IntechOpen

Tsunami

Edited by Mohammad Mokhtari

TSUNAMI

Edited by **Mohammad Mokhtari**

Tsunami
http://dx.doi.org/10.5772/61999
Edited by Mohammad Mokhtari

Contributors

Taro Kakinuma, Hiroshi Kanayama, Hiroshi Dan, Nils-Axel Morner, Daiki Ito, Kenji Tanaka, Belinda LIpa, Ghazala Naeem, Mohammad Mokhtari

Notice

First published in Croatia, 2016 by INTECH d.o.o.
eBook (PDF) Published by IN TECH d.o.o.
Place and year of publication of eBook (PDF): Rijeka, 2019.
IntechOpen is the global imprint of IN TECH d.o.o.
Printed in Croatia

Legal deposit, Croatia: National and University Library in Zagreb

Additional hard and PDF copies can be obtained from orders@intechopen.com

Tsunami
Edited by Mohammad Mokhtari
p. cm.
Print ISBN 978-953-51-2676-8
Online ISBN 978-953-51-2677-5
eBook (PDF) ISBN 978-953-51-5455-6

Meet the editor

Mohammad Mokhtari was born in Nosara, Neyshabur and has obtained his BSc from Azarabadegan University, MSc from the Southampton University and PhD from the Bergen University. He has worked as scientific assistant at the Utrecht University and principal geophysicist at Norsk Hydro (Norway) and NIOC. As the Director of Seismology Research Center at International Institute of Earthquake Engineering and Seismology (IIEES) and Member of Board of Directors, he has established the Iranian National Broadband Seismic Network. He has been the Cofounder and Director of National Center for Earthquake Prediction (NCEP) and founding member of the Risk Management Excellence Center, IIEES; coordinator of two International Conferences in Tehran; member of the Passive Seismic Equipment Expert Panel, CTBTO and visiting researcher at Geoscience of Australia, Indian Ocean Tsunami Hazard Assessment. He has been a member of ICG/IOTWMS Working Groups 1 and 3 and member of the Editorial Board of WDR 2009 report. He is now the Director of NCEP, ICG/IOTWMS, the Vice-Chairman of Working Group 2, and a member of advisory board at InTech publication. He supervised 28 MSc and 9 PhD students mainly in exploration seismology, seismology, and tsunami. His publications consisted of over 55 papers in international journals, over 100 conference presentations, and 5 books in different earth science subjects.

Contents

Preface

In the recent years, the world has experienced few mega-tsunamis which have caused extensive loss of life and property. The most destructive ones were in December 2004 in Sumatra, causing more than 290,000 deaths and in March 2011 in Japan, creating a nuclear accident. Because of these events, the recent advances in tsunami study have led the scientists to better understanding of the cause of tsunami, its propagation and most importantly, the system of warning ahead of tsunami arrival to the vulnerable coastal area. In continuation, the meteorological effects, meteo-tsunami and underwater volcanic eruption as other tsunamigenic sources are also being better documented and investigated. At last, let's also mention that onshore earthquake close to coast or located at the onshore part of the subduction zone has triggered the creation of mud-volcano island offshore and onshore, for example large earthquake of onshore Iran 2013 event. It is also important to mention as a pivotal point, the event of 2004 which has triggered many global initiatives such as a new tsunami detection system, more detailed coastal modeling, tsunami-compatible coastal developments and integrated approach for regional early warning system and public educations, awareness and preparedness. In these advances the environmental damage of urban communities (coastal) and ecosystems and consequently regional economic impact have been largely unattended to date, yet they may have very long-lasting effects both on environmental quality and on regional economy.

The book is divided into four sections. Section 1 covers the introduction to the topic. Section 2 which consists of two chapters provides information on tsunami propagation from the open sea to the coast and talks about coastal tsunami warning using deployed HF radar systems in many different parts of North America and Japan. The tsunami propagation, preliminary methods for evaluating the suitability of radar sites for tsunami detection using simulated tsunami velocities and factors affecting tsunami detectability are discussed and methods for reducing the false alarms are described.

Section 3 consists of two parts covering multi-scale meteorological systems resulted in meteo-tsunami (meteorological tsunami is a kind of ocean long wave with the tsunami frequency band from several minutes to 2 hours driven by atmospheric forcing at the sea interface). The second chapter of this section provides some details and scientific information, including some very important case studies on tsunami generation due to a landslide or a submarine volcanic eruption.

In Section 4, occurrence and characteristics of tsunami in Sweden, using paleo-tsunami events from different parts of Scandinavia are discussed in Chapter 6. Chapter 7 discusses challenges and opportunities for reducing losses to fast-arriving tsunamis in remote villages along the coast of Pakistan coast.

As a concluding remark, one important aspect concerning the local tsunamis is the role of the earthquake effect before tsunami waves are being generated and propagated toward the coast, and also an integrated worldwide tsunami early warning system needs to be fully accounted for in the future scientific discussion.

This book is based on expert writing with the objective of providing a collection of different aspects of tsunami events from generation by different sources including non-seismic, to propagation, detection, and warning dissemination. It is strongly believed that all the information provided here should play an important role in tsunami risk reduction and mitigation. The presented chapters have been peer reviewed and accepted for publication. We would like to express our gratitude to the contributing authors who have been the key factor in this achievement. Finally, we would like to specially thank the InTech publisher who initiated this book and guided and helped the Editor for its completion.

Prof. Mohammad Mokhtari
Director of Earthquake Prediction Center
International Institute of Earthquake Engineering and Seismology,
Iran

Introduction

Chapter 1

Introductory Chapter: A General Overview of Tsunami and Effectiveness of Early Warning System

Mohammad Mokhtari

Additional information is available at the end of the chapter

http://dx.doi.org/10.5772/65081

1. Introduction

Confirmed tsunami events from 1610 BC to AD 2014 are 1212 events from which 245 were deadly. The geographical distribution of these events is 76% in the Pacific Ocean, 9% in the Indian Ocean and Red Sea, 6% in the Atlantic Ocean and Caribbean Sea and 9% in the Mediterranean Sea. Concerning the sources for generation of the tsunamis, 87% are from earthquake, 8% from underwater volcanic eruptions, 4% from major ocean landslides and 1% from other sources [1].

In recent years, world has experienced few mega-tsunamis, which have caused extensive loss of life and properties. The most destructive ones were in December 2004 in Sumatra causing more than 290,000 death and March 2011 in Japan, creating a nuclear accident [2]. The event of 2004 has triggered many global initiatives, such as a new tsunami detection system, more detail coastal modeling, tsunami compatible coastal developments, integrated approach for regional early warning system (EWS) and public educations, awareness and preparedness.

Early warning system (EWS) can play an important role in risk reduction, using the effective development of national and local capabilities. However, it must be emphasized that national risk reduction strategies must not only be based on the EWS. If risk considerations are not adequately factored into national development strategies, disaster occurrence and loss will continue to increase, with or without the improved EWS capabilities. EWS should thus be seen as a last line of defense for dealing with unmanaged risks. EWS should be developed as vital element of much wider national risk management and reduction strategies. If the EWS is developed as stand-alone systems, it may contribute to generate a false sense of security leading to indifference and passivity in vulnerable groups and sectors as well as among national disaster management agencies and systems.

2. Tsunamis

2.1. Tsunami sources

The recent advances in tsunami study has lead the scientist for better understanding of the cause of tsunami, its propagation and most importantly the system of warning ahead of tsunami arrival to the vulnerable coastal area. In addition, now the secondary sources for strengthening the devastating effect of the tsunami, for example, the splay faulting, landslide caused by the parent earthquake sources, have been advancing [3].

The main source for tsunami generation, however, has been identified as being the earthquake. Due to this, we will discuss here two case studies, namely the Makran (Indian Ocean) and Great East Japan earthquake and tsunami Pacific Ocean.

The other sources are classified as meteorological effects, meteotsunami. This has been discussed fully within this book on Chapter 1, and the underwater volcanic eruption as other tsunamigenic sources also being better documented and investigated on Chapter 2 of this book.

Tsunamis can also be generated by a submarine landslide, which typically occurs as a result of an earthquake [4]. A submarine landslide, rock fall or ice fall can trigger a tsunami by displacing large amounts of water. As a result, the water level rises generating tsunami.

The Papua New Guinea tsunami of July 1998 is a good example of relatively small deepwater submarine landslide, which caused devastating local tsunamis. This was triggered by a magnitude 7.1 earthquake [5]. The multibeam bathymetric study is a very useful tool in identifying this type of potential submarine landslide offshore.

The other sources of major risk contributors are the onshore earthquake events rather close to sea. The thick sediments at Oman Sea provide conditions for submarine landslides and slumps that can generate small tsunamis in the region. Heidarzadeh and Satake [6] showed that the tsunami observed in the northwestern Indian Ocean following the 23 September 2013 Pakistan inland earthquakes was generated by a submarine landslide.

In addition, the splay faults mapped offshore Makran can also play an important role as tsunami strengthening factor after the major tsunamigenic event has occurred, but not as independent tsunami source [7–9].

It is very important to note that the coastal area can be affected by both local and remote-source tsunami. In the case of a local earthquake, the impact of the earthquake can be greater than the tsunami. The main tsunamigenic earthquake may cause damages to buildings and infrastructure before the arrival of the tsunami wave, with potential loss of life. Therefore, in the near coast (local) tsunami-prone area, both tsunami and earthquake effect must be considered.

http://dx.doi.org/10.5772/65081

2.2. Tsunami due to earthquake

2.2.1. Makran

From seismotectonic view point, the Makran subduction zone is characterized by the subduction of the oceanic part of the Arabian plate beneath the Eurasian plate [8] and extends along the Gulf of Oman from the Zendan-Minab fault system near the Strait of Hormuz in the west to the Baluchistan volcanic arc in the east. It has one of the largest accretionary prisms in the world with a thick (7 km) unconsolidated sediments [10, 11], lying above a shallow dipping decollement (**Figure 1**).

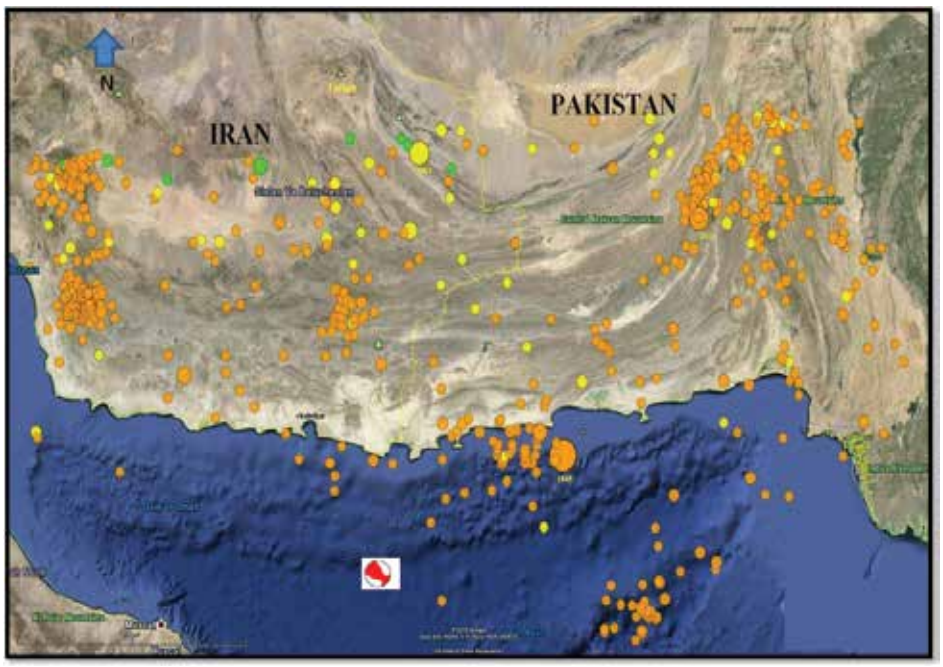

Figure 1. Makran seismicity 1940–2015, based on USGS catalog, the location and Focal Mechanism solution of 2015 earthquake also being indicated on the figure.

From seismicity point of view, compared with other similar zone in the world The Makran subduction area has been considered as having low seismicity. But based on data from 1945 tsunami, the affected area has been classified as a tsunami-prone region [11, 12].

2.2.2. Great East Japan earthquake and tsunami

The Pacific plate is subducting along the Japan Trench beneath Eastern Japan, whereas the Philippine Sea plate is subducting along the Nankai Trough beneath Western Japan [13]. The Philippine Sea plate is subducting along the Sagami Trough beneath the North American plate. The Pacific plate is converging with and subducting beneath the Okhotsk plate at about 40 mm

per year, resulting in frequent and large earthquakes [13]. The Japan Trough has a long history of large events, including the 869 Mw 8.3 Jogan, 1896 Ms 7.2 Meiji Sanriku and 1933 Mw 8.4 Showa Sanriku events, all of which produced large destructive tsunamis [13].

On 11 March 2011, an earthquake with magnitude of 9.0 off the northeastern coast of Japan triggered a tsunami [6]. The waves reached up to 40 m high and penetrated up to 5 km inland. It caused a great loss of life (~20,000), strong environmental damage and infrastructural destruction. The tsunami has also severely affected the Fukushima nuclear power plant, causing serious risks of contamination from radioactive releases.

2.2.3. Tsunami major disaster effects

One of the major disaster effects that require an especial attention is the environmental damage at the coastal area due to transportation of sediments and debris from ocean to coast and vice versa. For example, during 2004 Sumatra tsunami, the sediment transport and coastal subsidence associated with the tsunamis had a major impact on urban communities and also in ecosystems. Unfortunately, these types of impact have not been adequately studied because they may have long-term effects both on environment and on the regional economy.

2.2.4. Factors strengthening the tsunami disaster

Several case studies indicated that splay faults are associated with subduction zones in the world [3, 11]. They develop within the sedimentary sequences as sediments being added from the upper plate. The superimposed effect of splay faulting on tsunami wave heights in the near-field has been observed in many mega-tsunami events. In this respect, the 1946 Nankai, 1960 Chilean and 1964 Alaskan earthquakes and tsunamis [8, 14] and the most recent case of the 2004 Sumatra-Andaman could be mentioned.

Thus, splay faults can play an important role, in particular, as local hazard, and thus their identification is important.

At this stage, we do not believe that these faults individually are capable of producing tsunami, but as indicated above, they can play an important role in strengthening the tsunami hazard effect during megathrust ruptures. So, we strongly suggest that this factor should be accounted for a comprehensive tsunami hazard analysis. These factors in addition to the above-mentioned items, if are not implemented accurately, will make the design of an effective tsunami early warning system problematic [15].

2.2.5. Mud volcano (example from Makran)

Mud volcanoes are known from onshore, where erupted water often is methane saturated. These are the result of progressive compression and dewatering of the deep undercompacted, overpressured sequences (at decollement). The world's most notorious mud volcano, Indonesia's Lusi, destroyed a town in 2006.

Offshore Makran (Northwest Indian Ocean), numerous mud volcanoes have been mapped. There is a direct relationship between mud volcanoes and transform faults. Not all mud

http://dx.doi.org/10.5772/65081

intrusions reach the seabed (**Figure 2**). In places, there is clear evidence of mud intrusions in the shallow part of the sedimentary sequence. The mobilized overpressured sequences have clearly used the fault zones as conduits to reach low-pressure areas and the surface.

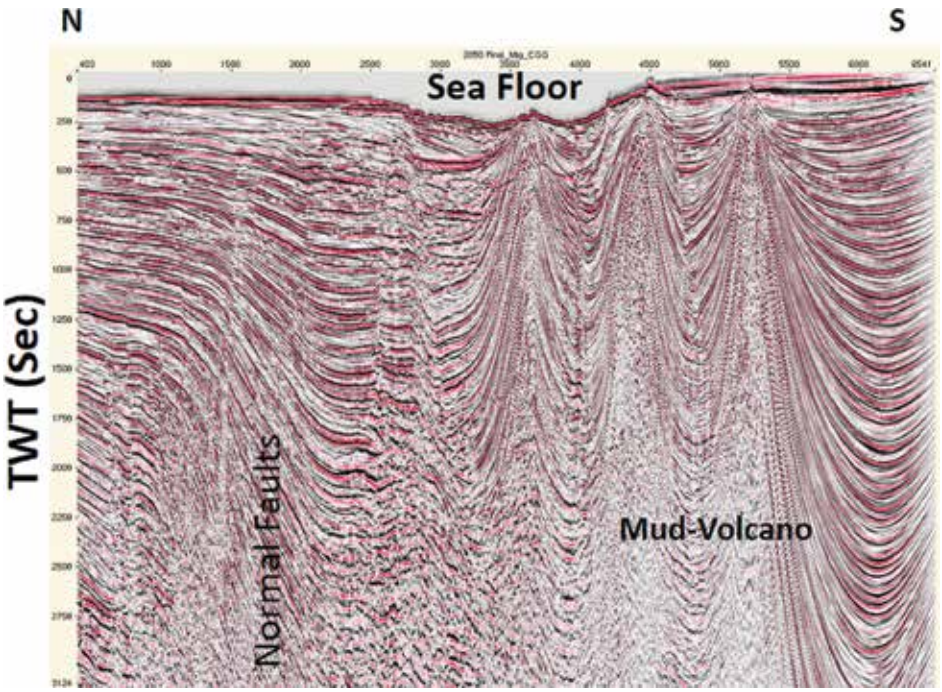

Figure 2. Seismic expression of mud volcanoes in the Makran subduction zone area, Oman Sea (belong to National Iranian Oil Company).

The offshore mud volcanoes, as the onshore once, have limited lifetime, and eroded tops have been observed.

On 24 September, a shallow 7.7 magnitude earthquake occurred in Pakistan. At least 300 people died and thousands of houses collapsed in Balochistan Province. The earthquake was felt as far as Oman and India. The earthquake appeared to be a strike slip event. An amazing effect of the earthquake—in roughly 40- km distance— is that a new island appeared few hundred meters off of Gwadar offshore. The island is about 18–21 meters high, up to 91 meters wide and up to 37 meters long [16].

3. Tsunami early warning system

The main elements that are required to be considered before any decision to set up an early warning system are frequency, severity, lead time, accuracy, response costs, loss reduction and

early warning system cost. A feasibility study needs to be conducted with great precision taking into account also the public education and their awareness to full response.

The current tsunami preparedness policy, which is oriented toward warning and evacuation, needs to be revised worldwide. Coastal cities, ports and marine constructions at tsunami risk are growing and becoming more and more vulnerable to a tsunami impact. Today, we cannot ignore an increasing risk of cessation of sea-port operation, oil platform destruction or coastal devastation. The safe and stable function of sea ports, coastal oil or gas tanks, cold storage, fisheries and other facilities becomes more significant for the economic development of coastal communities. Economic risk management is an important goal, which has to be solved for coastal urban and industrial areas at tsunami risk. Therefore, it is important to engage in day-to-day efforts to improve public awareness, preparedness and regional cooperation to deal with marine natural disasters.

4. Discussion and conclusions

In some areas, such as Japan's coast, the tsunami knowledge is high but other areas such as Indian Ocean region in particular Makran region is less advanced, and even some of the most important earthquake source parameters are less understood and require collection and analysis of more seismological and seismotectonic data. In this regard, it is important to note that in the recent years some progress is underway in the Makran region, for example, acquisition of some deep active seismic profiling using both explosion and air gun as seismic sources aimed at better understanding of the crustal structural elements and model to be used on tsunami hazard assessments.

In recent years, tsunami early warning systems are being established in the region. One of the essential parts of an effective warning system is the tsunami (earthquake) detection. It is important to consider how modern technology and lessons learned from past tsunamis worldwide can be combined to create safer coastal communities with tsunami aware populations.

For people living in coastal areas, protection awareness and education are other important elements in everyday lives, and through the professional responsibilities, understanding the disaster risk also increases the effectiveness of early warning system and policy implementation.

In this respect, the current tsunami preparedness policy, which is oriented toward warning and evacuation, needs to be revised worldwide. Coastal cities, ports and marine installations at tsunami risk are growing and becoming more and more vulnerable to a tsunami impact. Today, we cannot ignore an increasing risk of termination of sea-port operation, oil platform destruction or coastal devastation. The safe and stable function of sea ports, coastal oil or gas tanks, cold storage, fisheries and other facilities becomes more significant for the economic development of coastal communities. Economic risk management is an important goal, which has to be solved for coastal urban and industrial areas at tsunami risk. Therefore, it is important

to engage in day-to-day efforts to improve public awareness, preparedness and regional cooperation to deal with marine natural disasters.

Author details

Mohammad Mokhtari

Address all correspondence to: mokhtari@iiees.ac.ir

International Institute of Earthquake Engineering and Seismology, Tehran, Iran

References

[1] ITIC, (2014), Tsunami sources 1610 to A.D. 2014 from Earthquake, Volcanic Eruptions and other sources, tsunami sources August 2014; http://itic.ioc-unesco.org.

[2] Satake, K., 2014. Advances in earthquake and tsunami sciences and disaster risk reduction since the 2004 Indian Ocean tsunami. Geoscience Letters, 1(1), p. 1.

[3] Heidarzadeh, M., (2011). Major Tsunami Risks from Splay Faulting, The Tsunami Threat - Research and Technology, Nils-Axel Morner (Ed.), InTech, DOI: 10.5772/13375. Available from: http://www.intechopen.com/books/the-tsunami-threat-research-and-technology/major-tsunami-risks-from-splay-faulting.

[4] Heidarzadeh, M., Krastel et al, S., Yalciner, A.C., (2014) The state-of-the-art numerical tools for modeling landslide tsunamis: a short review. In book: Submarine Mass Movements and Their Consequences, Edition: 6, Chapter: 43, Publisher: Springer, Editors: Krastel et al, pp.483-495.

[5] Tappin, D. R., Watts, P., Grilli, S. T., 2008. The Papua New Guinea tsunami of 17 July 1998: anatomy of a catastrophic event, Natural Hazards and Earth System Sciences, 8, 243–266.

[6] Heidarzadeh, M. and Satake, K., 2014b. Excitation of basin-wide modes of the Pacific Ocean following the March 2011 Tohoku tsunami. Pure and Applied Geophysics, 171(12), pp.3405-3419.

[7] Heidarzadeh, M., Pirooz, M.D., Zaker, N.H., Yalciner, A.C., Mokhtari, M. and Esmaeily, A., 2008a. Historical tsunami in the Makran Subduction Zone off the southern coasts of Iran and Pakistan and results of numerical modeling. Ocean Engineering, 35(8), pp. 774–786.

[8] Mokhtari M., 2014. The role of splay faulting in increasing the devastation effect of tsunami hazard in Makran, Oman Sea, Arabian Journal of Geosciences 8(7) 161–174.

[9] Smith, G. L., McNeill, L.C., Wang, K., He, J., Henstock T.J., 2013. Thermal structure and megathrust seismogenic potential of the Makran subduction zone, Geophysical Research Letters, 40, 1–6.

[10] Byrne, D. E., Sykes, L. R., Davis, D. M., 1992. Great thrust earthquakes and aseismic slip along the plate boundary of the Makran subduction zone, Journal of Geophysical Research, 97(B1), 449–478.

[11] Mokhtari M, Abdollahie Far I, Hessami K., 2008. Structural elements of the Makran region, Oman Sea and their potential relevance to tsunamigenisis. Natural Hazards, 47, 185–199.

[12] Heidarzadeh, M., Pirooz, M.D., Zaker, N.H. and Synolakis, C.E., 2008b. Evaluating tsunami hazard in the northwestern Indian Ocean. Pure and Applied Geophysics, 165(11-12), 2045-2058.

[13] Scawthorn, C. and Porter, K. A. (2011) Reconnaissance Report Aspects of the 11 March 2011 Eastern Japan Earthquake and Tsunami, SPA Risk., http://www.sparisk.com/pubs/SPA-2011-Tohoku-Report.pdf

[14] Plafker, G. 1972. Alaskan earthquake of 1964 and Chilean earthquake of 1960: Implications for arc tectonics. Journal of Geophysical Research, 77(5), 901-925.

[15] Mokhtari M, 2011. Tsunami in Makran Region and its effect on the Persian Gulf, In edited by Mokhtari M, Tsunami - a growing disaster, InTech Publication, Open book publication. http://www.intechopen.com/books/show/title/tsunami-a-growing-disaster

[16] Heidarzadeh, M. and Satake, K., 2014a. Possible sources of the tsunami observed in the northwestern Indian Ocean following the 2013 September 24 Mw 7.7 Pakistan inland earthquake. Geophysical Journal International, 199(2), 752-766.

Section 2

Tsunami Generation

Chapter 2

Multiscale Meteorological Systems Resulted in Meteorological Tsunamis

Kenji Tanaka and Daiki Ito

Additional information is available at the end of the chapter

http://dx.doi.org/10.5772/63762

Abstract

Meteorological tsunami is a kind of the ocean long wave with the tsunami frequency band from several minutes to 2 h driven by atmospheric forcing at the sea interface. The multiplying of resonance and amplification effects enhanced the wave higher than 1 m with the destructive damage. The direct forcing of meteorological tsunami is the meso-β-scale disturbance, such as mesoscale convection system or internal gravity wave in the troposphere. The events on the destructive meteorological tsunamis were reported mainly on the mid-latitude regions such as Europe and US East Coast. Whatever the kind of the disturbance was, the intrusion of the dry air played important roles in unstable structure of the middle troposphere to travel the disturbance with a long disturbance. The backward trajectory of the air particle on the tsunami-enhancing region showed that the lifting of anomalous warm moist air mass from the lower latitude was significant to form the atmospheric structure over the targeted seas. Such characteristics in the large-scale atmosphere provide the possibility of the mid-term prediction on meteorological tsunamis, linking with the state-of-art observation technologies in satellite remote sensing, radar observation, in situ measurement network and so on.

Keywords: meteorological tsunami, inverse pressure effect, resonance, meso-β-scale disturbances, convective systems, atmospheric internal gravity wave, continental scale circulation

1. Introduction

Meteorological tsunami (or meteotsunami) is a kind of ocean long wave with the tsunami frequency bands from several minutes to 2 h driven by atmospheric forcing such as the disturbance of sea level pressure, wind, and others [1, 2]. The sea level rises (or depresses) inside

of the negative (positive) pressure anomalies. The sea level also rises accordingly with the horizontal convergence of the wind stress, for example, around the front or the coastal area. Such basic mechanism to set the wave up is similar as the storm surge. But the period of the storm surge is as long as tidal motion (approximately half or 1 day), while that of meteorological tsunami is generally much shorter than tidal motion. The intensity of the sea level deformation by severe storm is typically as large as several 10 cm or higher than 1 m including wind stress. But the intensity itself of the forcing to meteorological tsunami is much smaller than that related to storm surge: an order of several centimetres in typical cases. The multiple mechanism of the resonance at the sea interface enlarges the amplitude of the ocean long waves, and the wave will possibly become higher than 3 m with flooding and destruction of the dikes. The primitive mechanisms on meteorological tsunami are founded by geophysicists in the earlier and middle twentieth century [2–4]. In recent decades, however, the integration of the scientific findings throughout severe case studies and the advances in field observation, numerical modelling and data assimilation have revealed the significance of the multiscale mechanisms on atmospheric and oceanographic processes.

In the present chapter, we briefly introduce resonant mechanisms as propagating meteorological tsunamis. Next, we show the area where destructive meteorological tsunamis have been reported. After that, we present the various kinds of the weather conditions resulting in meteorological tsunamis. **Figure 1** indicates the typical scale of meteorological phenomena and oceanographic motion. The temporal scale of meteorological tsunami typically matches the meso-β-scale motion in the atmosphere such as squall line, internal gravity wave, gravitational flow and so on. However, the genesis of those motion is influenced by both smaller- and larger-scale motions. The organization of turbulent plume will generate the cumulus convection, and cluster of the convective cells will form the meso-β-scale system.

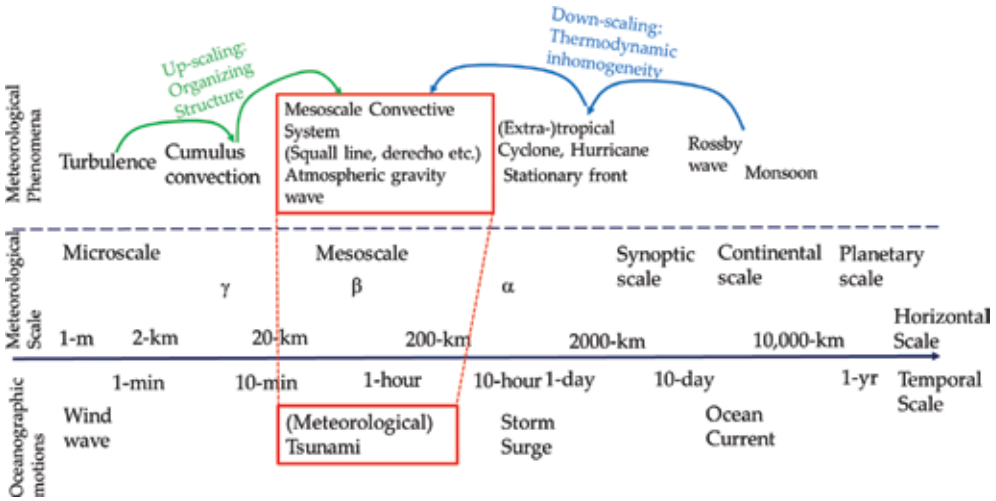

Figure 1. Scale of the various meteorological phenomena, and oceanographic motions.

http://dx.doi.org/10.5772/63762

The larger-scale motion provides the atmospheric instability structure by mixing dry air and moist air mass, that is, thermodynamic inhomogeneity. Hence, we first present the mesoscale phenomena resulting in meteorological tsunami, and then we discuss the meteorological phenomena including the large-scale motion (synoptic or continental scale). After that, we discuss and conclude the predictability of the meteorological tsunami with the current technologies on field observation, numerical modelling and data assimilation.

2. Resonant and amplifying mechanisms of the meteorological tsunami

2.1. Proudman resonance

One of the most important resonances was derived by Proudman (1929) [4], which is a coupling of the ocean long wave and the atmospheric disturbance. Let U the propagation speed of the pressure disturbance, and $c = (gH)^{1/2}$, the phase velocity of the ocean long wave dependent on the ocean depth H and the acceleration of the gravity, g. The Froude number Fr is defined as the ratio between the atmospheric motion and the ocean wave propagation, $\mathrm{Fr} = U/c$. Assuming that the friction, Coriolis, eddy viscosity and advection terms can be negligible (i.e. one-dimensional (1D) linear wave), the normalized sea level change becomes

$$\frac{\eta}{\eta_s} = \frac{1}{1 - Fr^2} \tag{1}$$

in equilibrium, where $\eta_s = -\Delta P/\rho g$ the sea level change under static balance with the intensity of the pressure anomaly ΔP and the density of water ρ. Equation (1) implies that sea surface can be deformed unlimitedly as the pressure disturbance moves the ocean with the same speed of the phase velocity of the long wave (i.e. holding Fr ~1).

When Fr ~1, the work due to the atmospheric pressure gradient force supplies wave energy at the same phase continuously, and the magnitude of the sea level deformation will be proportional to the travelling distance of the pressure disturbance on the sea interface. If $U > c$, that is, Fr > 1, that is, supercritical propagation over very shallow water, a wake forms similar to that passing the vessel with high speed. On the other hand, the subcritical propagation such that $U < c$, the ocean long wave will propagate ahead of the atmospheric disturbance, with the wave length becoming longer and longer instead of enlarging the amplitude.

The effect of the Proudman resonance typically ranged from two to five times of the stationary state. When the atmospheric disturbance travels longer than 1000 km keeping Fr =1 ± 0.10, the resonant effect can be higher than 10 times of the stationary state. Hibiya and Kajiura (1982) [5] derived the formula under the condition of Fr ~1 as,

$$\frac{\eta}{\eta_s} = \frac{1}{2}\frac{X_f}{W} \tag{2}$$

where X_f represents the fetch of the pressure disturbance, and W is the width of the pressure disturbance. For example, X_f = 500 km, W = 50 km yields the amplification ratio η/η_s = 5.0.

2.2. Shoaling and refraction

Similar to seismic tsunami, meteorological tsunami is also amplified by shoaling and refraction. Linear theory can be used as the first approximation to calculate the wave height as the wave moves across an ocean and undergoes wave shoaling and refraction. The formula can be written as (e.g. Synolakis, 1991 [6])

$$\frac{\eta_p}{\eta_o} = \left(\frac{D_o}{D_p}\right)^{\frac{1}{4}}\left(\frac{B_o}{B_p}\right)^{\frac{1}{2}} \tag{3}$$

where η_o = wave height (crest to trough) at the original point, η_p = wave height (crest to trough) at any point, D_o = water depth at source point, D_p = water depth at any shoreward point, B_o distance between wave orthogonals at a source point of water and B_P = distance between wave orthogonals at any shoreward point of water. The ratio between B_o and B_p indicates the refraction, and the ratio between water depth indicates the shoaling, a part of Green's law.

2.3. Resonance of the edge wave

The resonance due to continental shelf is also significant in amplifying the meteorological tsunamis. For example, Greenspan (1956) [7] derived the surface elevation across the continental shelf from the linearized shallow water equation. Let the beach slope α = tan β, and U = velocity of pressure disturbance along the edge, the frequency of n-th edge mode can be described as

$$\mathrm{k_n} = (2n+1)g\alpha / U^2 \tag{4}$$

Giving the pressure distribution as a Gaussian function moving along the shelf edge, the amplitude of the n-th edge wave depends (with the wave number of k_n) on the intensity of the pressure disturbance P_0, the moving speed of the system, horizontal scale of the disturbance a and the distance from the coast line y as

$$\mathrm{A_n}(k_n) = -\frac{2}{U}\left(-\frac{2\sqrt{\pi}UP_0a}{\rho}\right)k_n^2\exp\left(-\frac{a^2k_n^2}{4}\right)\int_0^\infty L_n(2k_ny)\exp\left\{-k_ny-\frac{(y-y_o)^2}{a^2}\right\}dy \tag{5}$$

http://dx.doi.org/10.5772/63762

where

$$L_n(s) = \exp(s)\left(\frac{d^n}{ds^n}\right)\left(s^n \exp(-s)\right) \tag{6}$$

For fundamental edge mode (n = 0), the maximum wave height becomes maximum with the half-pressure radius of 80–90 km. This implies that the meso-β- or γ-scale disturbance, the typical wavelength of the meteorological tsunami, is able to amplify the wave by edge mode rather than meso-α-scale disturbance such as hurricane.

2.4. Harbour resonance

The resonance in the harbour or the inlet is the conclusive effect of how much sea level oscillates inside them. Assuming that the bay shapes rectangular open channel with uniform sea depth (H), and the incident direction of the ocean wave is parallel to that of the axis of the bay. The period (T) for eigen oscillation of the bay is

$$T = \varepsilon \frac{4L}{n\sqrt{gH}} \tag{7}$$

with L = axis length of the bay. The coefficient ε represents the correction coefficient for the bay mouth effect due to the generation of scattering waves near the bay of the mouth [8] as

$$\varepsilon = \left[1 + \frac{2B}{\pi L}\left(0.923 + \ln\frac{4L}{\pi B}\right)\right]^{\frac{1}{2}} \tag{8}$$

where B = the width of the bay mouth. For more details, refer to Ravinobich (2009) [9] for the various shapes of the inlets.

3. Meteorological tsunami in the world ocean

The area where large meteorological tsunamis with the destructive damages were reported is marked in **Figure 2**. The colour palette in **Figure 2** indicates the phase speed of the ocean long wave $c = (gH)^{1/2}$, instead of the sea depth. Much of the events occurred in the mid-latitude, where the energy transport towards polar region is the most active throughout the meridional circulation. The wind speed of the mid-troposphere typically ranges 20–40 m/s along with the westerly jets, which is dominant to propagate the meso-β- or γ-scale atmospheric disturbance at sea level.

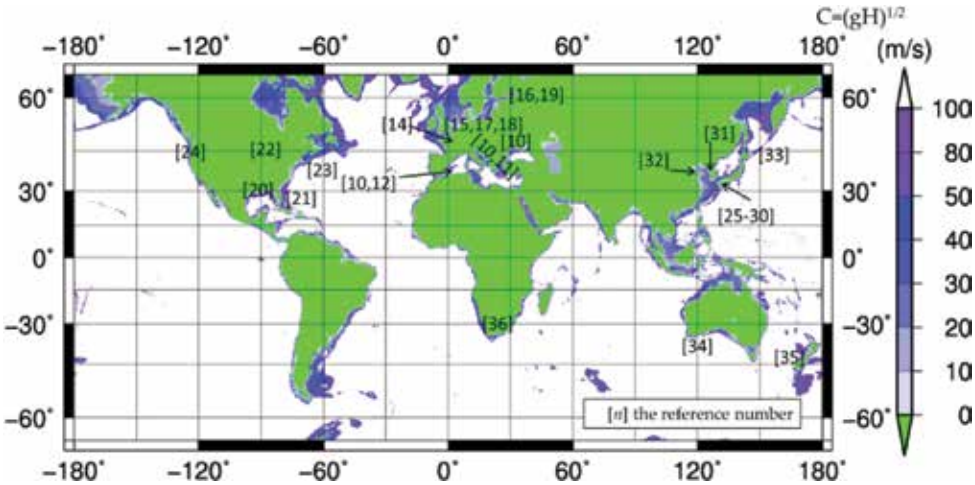

Figure 2. Map of the destructive meteorological tsunami events in the world. Colour shows the propagation speed of the ocean long wave $c = (gH)^{1/2}$ using the bathymetry of ETOPO5. Numbers indicate the location of event of the related references cited in this section.

Vera Luka, Croatia, June 1978
Vilibić et al. (2009)[11]

Ciutadella Harbour, Menorca Is.
Spain, June 2008 Vilibić et al. (2008)[12]

Figure 3. Example of scenes on destructive meteorological tsunami [11, 12].

The Mediterranean Sea including Adriatic Sea is one of the hotspots of the meteorological tsunamis. One of the recent major events occurred on 23–27 June 2014 due to the internal gravity wave (IGW) of the mid- and low troposphere [10]. In that event, the wave height became as high as 2–3 m in the wide area of the sea. The atmospheric IGW propagated not only over the Mediterranean Sea but extended to the Black Sea. The east coast of the Adriatic Sea, Croatia (*šćiga* in local name) has many small islands and complicated shoreline shape with small bays (smaller than 10 km in axis length) and has suffered from severe events. The most severe event in June 1978 brought the maximum wave height as high as 6 m [11]. At least five destructive events with the inundation damage occurred other than 2014 event: in June 1978 at Vera Luka

http://dx.doi.org/10.5772/63762

with 3-m wave height, in October 1984 at Ist Island with 4-m wave, in June 2003 over the middle Adriatic coast with approximately 3.5-m wave, in August 2007 at Ist Island with 4-m wave and in 2008 at Mali Lošinj [11]. The Balearic Island (*rissaga* or *resaca* in local name) is the area where large amplified waves hit as frequent as the Adriatic Sea. The large wave as high as 2 m hit that area once per 5–6 years. And 3–4-m waves hit once per 20–30 years. June 2006 event was the most severe one in recent decades: the wave as high as 4–5 m hit the the Ciudadella Harbour of the Menorca Island located in the east of the Balearic Islands [12]. An example of meteotsunami damages in those two areas is shown in **Figure 3**. Hundreds of fishing boats were destroyed by strong current, and hundreds of motorcars and number of residences were damaged by flood. Other coast at Sicily in Italy (*marrubio* in local name) and at Marta (*milghubo* in local name) also recorded wave height higher than 1 m in hitting the meteorological tsunamis [13].

Much of the large meteorological tsunami events had been reported over the coastal area of the northwest Europe, but not so frequent as compared to the Mediterranean Sea region. Since the shallow seafloor extended in the northwest Europe, it is easier for the wave to enhance by the Proudman resonance. Haslett et al. (2009) [14] summarized 9 events of the possible meteorological tsunamis over past 120 years in the United Kingdom. The recorded wave height ranged 4–9 m, caused mainly by squally thunderstorms. According to their paper, the sudden sea level rise within 5–10 min was reported. That time was too long to period of swell with the period around 10 s or little bit longer. The amplification effect in shoaling at the continental shelves of the Atlantic Ocean seemed to play an important role in the enhancement of the meteorological tsunamis. Much of the meteorological tsunami events were recorded in the South Wales and South England, where the channel opens to the west (Atlantic Ocean). The squall lines along with cold front in developed extratropical low sometimes bring the meteorological tsunamis in the southern North Sea [15] (*zeebeer* in Netherland, *seebär* in Germany) and Baltic Sea (*seebär* in Germany, or *sjösprång* in Swedish) [16]. The major recent event was brought by the cold front passed over the Netherland and Belgium on January 3, 2012. According to the weather information service webs in Netherland, sudden depression of the tide level was recorded by 1.66 m per 20 min at van Rijkswaterstaat [17], while the sudden rise of the tide level was recorded by 1.05 m per 20 min in Ijmuiden [18]. In the coastal area of the Finland, the latest major event brought the wave higher than 1.0 m (10–15 min in period) on July 29, 2010. The meteorological tsunami up to 1.5 m in wave height was also reported in May 15, 1924, caused by thunderstorm [19].

The developed squall line system or the atmospheric gravity waves brought the meteorological tsunamis in the wide area of East Coast of the United States including the Florida Peninsula and Gulf of Mexico [20, 21]. On March 1995, the giant meteorological tsunami with a 3.3-m wave height hit along the east coast of the Gulf of Mexico, Florida, due to the atmospheric gravity waves propagated from the Texas-Louisiana thunderstorm [20]. The derecho developed at the inland area of the North US brought the meteorological tsunamis not only in the Atlantic Ocean but also in the Great Lakes [22]. The meteorological tsunami on the Great Lakes as large as 3 m in wave height recorded on by squall line passage in June 1954 even the lateral extent was not so wide (~250 km) as compared to the continental shelves in Atlantic Ocean [23].

The west coast of United States has complicated shoreline shapes, similar to the Adriatic Coasts. However, the wave amplitude for each event was not so large [24].

East Asia region is one of the major spots of meteorological tsunami. There are several characteristics that can enhance meteotsunami much easier than other coastal regions. The unstable layer in the middle troposphere can easily form because a couple of jets in the upper air get closed in the leeward of the Tibetan Plateau. The lifting of the wet moist air from lower latitude and the descending of the upper dry air from continental region makes the so-called wave-ducting layer often. A wide coastal continental shelf is extended from China to the Islands of Japan. The equivalent speed of the ocean long wave ranged 20–40 m/s except the Okinawa trough near the Kyushu Island, Japan. What is more, there are many small inlets having eigen periods ranging between several minutes and several hours. In March 1979, a giant meteorological tsunami (*abiki* in local name) hit on the Nagasaki Bay in Kyushu, Japan, by passing abrupt pressure jump of 5.9 hPa per 30 min. The tide gauge observed the maximum wave height of 2.78 m [25]. A large meteorological tsunami also caused by train of pressure wave with the amplitude of 0.5–2.0 hPa, with the wave length of 20–100 km [26, 27]. In the west Kyushu, most of meteorological tsunami are likely observed in the season between February and early April [28, 29]; however, the severe squall system such as Baiu front sometimes generates the strong downdraft to meteorological tsunamis [30]. On the west of the Korean Peninsula, maximum amplitude of 1.4–1.6 m recorded in March 2007 and May 2008 with the pressure jump of 2–5 hPa travelled over the Yellow Sea [31]. In the Bohai Sea of China, sea level oscillations with the amplitude higher than 1.0 m are often observed; however, the oscillation period was much longer (56–160 min) than that reported in other coasts (nearly 5–20 min). Such large amplified oscillation remained unclear as to what kind of the atmospheric sources induces such a long period wave [32]. The meteorological tsunami hit on the Kuril Island and the Kamchatka when the developing low approached the area from Hokkaido, Japan. In recent years, the wave height recorded was higher than 1.2 m in February 2010 [33].

Some destructive events have been introduced in recent papers, which occurred on the southern hemisphere. The west coast of Australia caused the meteorological tsunami resulting from squall line or frontal passage in the low pressure system. The wave height of 1.0 m was recorded in the frontal passage on June 12, 2012 [34]. Similar magnitude of meteorological tsunami was measured on the coast of New Zealand in April 2002 (*rissaga* in local name) [35]. A large flooding damage by meteorological tsunami 2.9-m wave height occurred on the west coast of South Africa on August 7, 1969. In that event, the flooding damage of housings and parked automobiles was brought within the area of 2 km along the shoreline and 100–200 m across the shoreline due to run-up of the wave [36].

It is possible that other coastal areas hit the meteorological tsunami if the multiple resonant conditions were satisfied. However, the recorded wave height were smaller than 1-m in those coastal areas. For example, Pattriaratki and Wijeratne (2015) [14] introduced smaller meteotsunamis in the tropical region such as Sri Lanka and India.

http://dx.doi.org/10.5772/63762

4. Mesoscale convective systems

The mesoscale convective system (MCS) is one of the most important phenomena to generate pressure jumps at sea level. The horizontal scale of the individual convective cell is an order of ~10 km, with the lifetime of several tens of minutes. The vertical wind speed sometimes becomes as high as 20 m/s under the strong unstable atmosphere with the convective available potential energy (CAPE) higher than 1000 J/kg. A high pressure anomaly, of the order of 1–2 hPa, generates at the surface level inside the convective cell due to the downdraft. To travel a long distance satisfying the Proudman resonance, it is significant to form a series of the convective system including multiple cells such as squall line.

Derecho is one of the systems with a long lifetime, which can move fast and long enough to have Proudman resonance on the ocean surface. The lifetime of the derecho is longer than 6 h travelling hundreds to thousands of kilometres as seen in **Figure 4** [20]. Some of the severe systems bring very strong gusts higher than 40 m/s (~90 miles/h) with the destructive damage of housings in the land area. A schematic of the derecho structure and sea level pressure fluctuation is shown in **Figure 5** [37]. The organized convective systems move towards the warm sector parallel to low-level thickness lines with the mean tropospheric flow. The system moves as high as 15–25 m/s (50–90 km/h), when the velocity of the mean tropospheric flow is very fast against the horizontal wind velocity of the low-level moist air into the convective system.

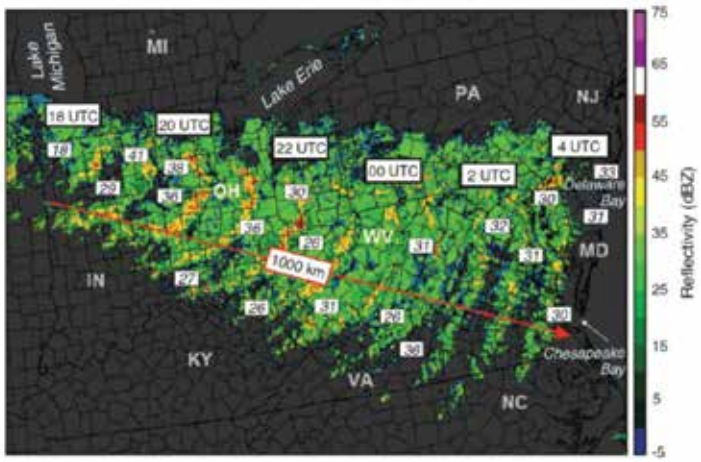

Figure 4. A mosaic composite of radar reflectivity (dBZ) image indicating the development and evolution of the derecho during June 29 and 30, 2012. Unitless numerical values indicate observed wind gusts (m/s). (Image by G. Carbin, NOAA/NWS Storm Prediction Center [22]).

In the US East Coast, the derecho had moved from land to ocean and the tsunami propagated towards offshore with Proudman resonance. **Figure 6** shows a sequence of the wave propagation simulated by the Pacific Tsunami Warning Centre, NOAA, as an example of June 13, 2013 [38]. The body wave, surrounded by a rectangle marked as 'a', generated along the coast

of Philadelphia (see the upper left panel in **Figure 6**) and moved eastward over the continental shelf. The wave was reflected along with the edge of the continental shelf and back to the coast. The body wave propagated across the edge after 17:00Z, crossing with the reflected wave. The body wave seemed to have disappeared at 20:00Z, which travelled longer than 300 km along the coastal shelf. The area of the maximum wave height higher than 10 cm corresponded with the area passing the body wave with resonance effect.

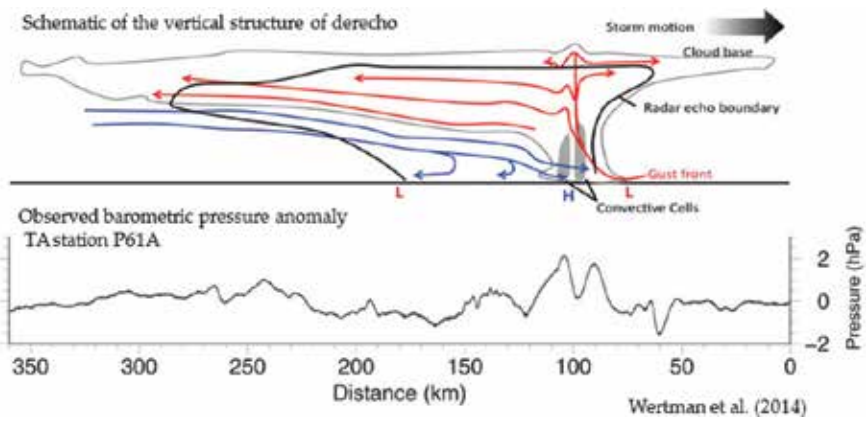

Figure 5. A schematic of the vertical structure of derecho (upper panel) and observed barometric pressure anomaly during the passage of derecho (lower panel) after case study on June 13, 2013 event, by Wertman et al. (2014) [37].

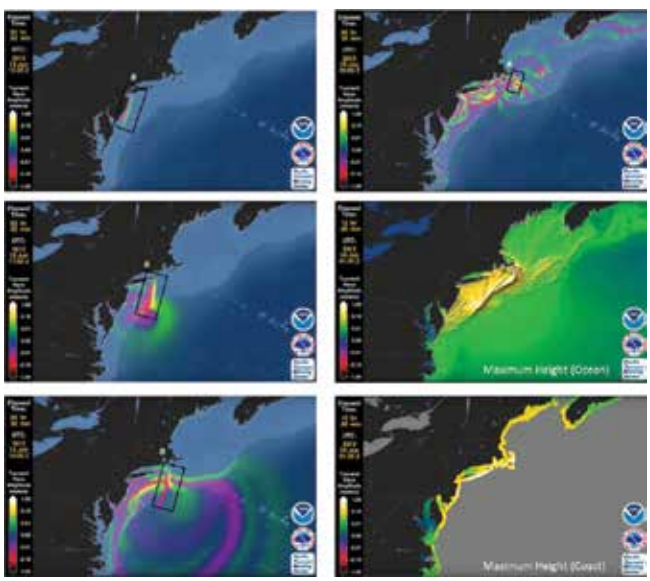

Figure 6. A sequence of the meteorological tsunami propagation computed by NOAA Pacific Tsunami Warning Centre. (Available from https://www.youtube.com/watch?v=ykABRe5Yt3c [38]).

http://dx.doi.org/10.5772/63762

5. Pressure jump of Nagasaki 1979 'Abiki' event

The system with the strong intrusion of the cold dry air can cause the abrupt pressure jumps with weak precipitation or without precipitation. **Figure 7** shows the satellite image and the observation records of meteorological tsunami by abrupt pressure jumps at Nagasaki Bay in west Kyushu, Japan [25]. The maximum wave height showed 278 cm at the third wave in tidal station of Nagasaki port. Some references cited the maximum wave of 4.8 m at this event [14], but that value was estimated value using Green's formula in Eq. (3). Abrupt pressure jump of 5.9 hPa per 30 min was recorded at Meshima about 140 km southwest from Nagasaki. The pressure jump decayed as the system moved to east and the intensity was 3.0 hPa per 20 min. Hibiya and Kajiura (1982) [5] proposed that the pressure jump was generated at the region near Shanghai, China, while Akamatsu (1982) [25] suggested that pressure jump was generated more towards the east side near Meshima. The satellite visible image showed that there was clear boundary between the stratiform cloud and the dry air in the middle of the East China Sea.

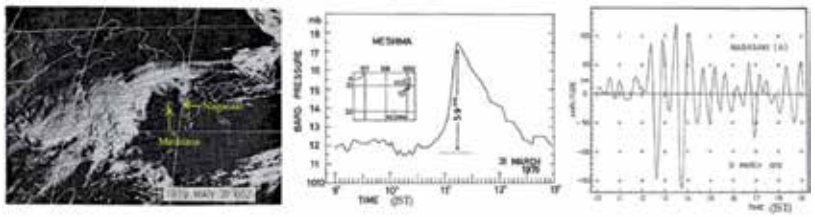

Figure 7. Meteorological tsunami of Nagasaki Bay caused by abrupt pressure jump on March 31, 1979. Satellite visible image by Geostationary Meteorological Satellite (left), barometric pressure recorded at Meshima (middle) and tidal amplitude observed at Nagasaki Bay (right) (Akamatsu 1982) [25].

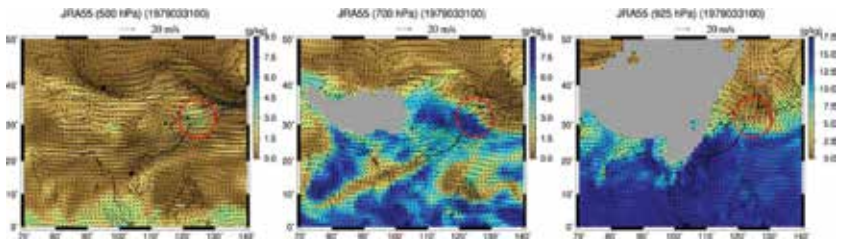

Figure 8. Distribution of the wet and dry air and horizontal wind in 500 hPa (left), 700 hPa (middle) and 925 hPa (right) isobar surface on 00Z, March 31, 1979. The reanalysis data of JRA-55 (Kobayashi et al. 2015) [39] was used.

The long-term reanalysis data from Japan Meteorological Agency (JRA-55) [39] in **Figure 8** indicated that the lower troposphere over the East China Sea was very dry (smaller than 3 g/kg in mixing ratio) and moist air came from south China region in 700 hPa isobar surfaces. The moist air lifted upward orographically in the mountain range of south China and vapour front formed in the mid-troposphere. Around the vapour front, the dry air cooled by re-

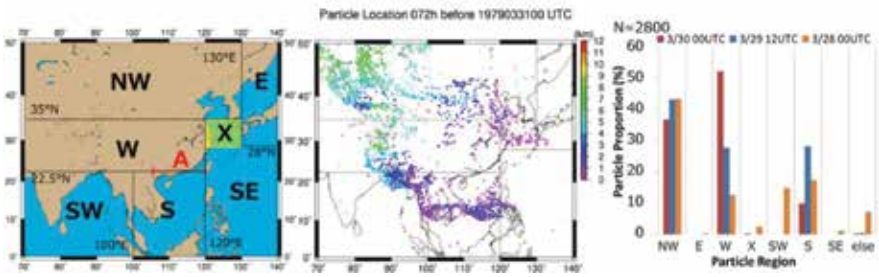

Figure 9. Air particle distribution into East China Sea. The left panel indicates the analysis area with initial particles located in region X. The middle panel shows the distribution of the individual particles 72 h before the meteorological tsunami over the East China Sea. The colour markers indicate the altitude of each air particles. The right panel indicates the particle proportion in each sector shown in the left panel [26].

evaporation of the cloud liquid water and settled down. The pressure jump was generated in the dry sector of the vapour front in the mid-troposphere. The back trajectory analysis of the air particle [39] depicted in **Figure 9** showed that the air particle in the East China Sea during the meteotsunami event came from mainly two or three regions. The warm moist air mainly came from South China Sea, Indochina Peninsula and Bengal Bay. Those air particles moved northeast along with the high-pressure system located in the Philippines, and lifted orographically over the inland area of the South China (region 'SW' and 'S'). Other particles came from upper dry air of northwest Eurasian continent or along with the subtropical jets via Tibetan Plateau (region 'NE' and 'E'). Further analysis in **Figure 10** showed that the anomalous mass of the moist air in the lower troposphere was transported from the tropical regions within 3 days before the meteotsunami event on March 31, 1979. The peak value of the moisture transport in the end of March (~200 kgm/s) was much greater than the peak value in the summer monsoon season (~150 kgm/s). The massive transport of the lower moist air into inland China can be seen especially in the late winter and early spring (February–April) for nearly every year. In the same period, the secondary oscillations larger than 1.0 m in amplitude were

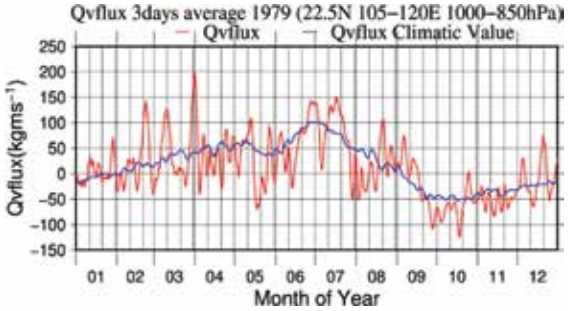

Figure 10. The northward component of water vapour flux across the line of South China coasts (22.5N, 105–120E) after the vertical integration between 850- and 1000-hPa isobar surface. Red line indicates the 3-day average from 6-h data in the year 1979. Blue line indicates the 10-day average of climatic value for 55 years (1958–2012) [26].

http://dx.doi.org/10.5772/63762

measured in the west Kyushu [27] nearly for every year. Hence, fluctuation of the vapour transport from tropical region to inland China can be key information to provide the first guess of the atmospheric disturbance causing meteorological tsunamis.

6. Atmospheric gravity waves in the troposphere

The atmospheric gravity waves are also one of the typical processes to generate pressure disturbance in the sea level, travelling with a long disturbances. There are two mechanisms supporting such characteristics of the atmospheric gravity wave: wave duct [40] and wave CISK [41]. The stable lower troposphere with an increasing wind in a vertical direction is overtopped with an unstable layer in the mid-troposphere as illustrated in **Figure 11** [10]. The Richardson number Ri

$$Ri = \frac{N^2}{\left(dU / dz\right)^2} \tag{9}$$

is generally used to see the atmospheric stability, where N = the Brunt-Väisälä frequency and U = horizontal velocity. Such vertical structure reflects the wave energy and traps the gravity waves towards the long distance [40, 42, 43]. The potential for downward or upward propagation of mid-tropospheric internal gravity waves may be assessed from the inequality of the linear gravity wave theory [43, 44].

$$N > \frac{2\pi U}{\lambda} \tag{10}$$

where λ = the horizontal wavelength of internal gravity wave. The depth of the wave duct D is described as

$$D = \lambda_z \left(\frac{1}{4} + \frac{1}{2}n\right) \qquad (n = 0,1,2,....), \tag{11}$$

where λ_z denotes the vertical wave length. Using the wind speed at critical level U_c, the λ_z can be approximated as

$$\lambda_z \approx 2\pi \frac{U_c - U}{N} \tag{12}$$

The wave CISK denotes the coupling between the gravity wave and convection. The convergences associated with the gravity wave force the moist convection while convection heating provides the energy for the wave [26, 41, 45].

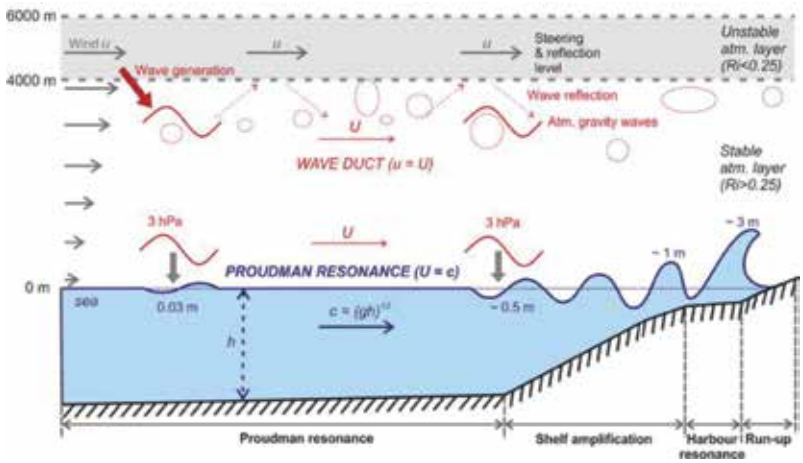

Figure 11. Schematic of the generation and the propagation of the atmospheric gravity wave in the presence of the wave-ducting layer, and the enhancement of the ocean long wave. A case study for widespread meteorological tsunami on Mediterranean and Black Sea, in June 2014 (Šepić et al., 2015) [10].

The large-scale motions with meso-α scale, synoptic scale or monsoon scale provide the structure of wave-ducting layer or wave CISK. In June 2014 event, the expansion of the wave-ducting layer generates and propagates the atmospheric gravity waves. The synoptic weather pattern and the sea level oscillation in that event are shown in **Figure 12** [10]. According to the Šepić et al. (2015) [10], the synoptic structure can be summarized as follows: first, inflows of warm and dry air from Africa in the low troposphere (~850 hPa); second, a strong south-west jet stream in the middle troposphere (~500 hPa) and the presence of the unstable layer between 600 and 400 hPa isobar [10]. The first pattern appeared at Menorca Island, Spain, in the west of the Mediterranean Sea, and the area of the wave propagation moved eastward [10]. The area of the high wind speed in the middle troposphere was located east of the trough.

The cold or dry sector of the cold or stationary front can satisfy the wave-CISK or wave-duct structure very well. In February 2009 event in the west Kyushu in **Figure 13**, Japan, a train of the pressure wave was generated in the north sector of the stationary front under both mechanisms of wave duct and wave CISK. The warm moist air lifted by the mountain effect in South China mixed with the dry air of the mid-troposphere from the south of the Himalaya mountain range. The mixed air generated the unstable layer in the mid-troposphere and covered above the East China Sea. The trough extended from the Siberia and the subtropical high-pressure system generated the latitudinal convergence over the area of the unstable mid-troposphere [26]. The wave length of the pressure waves ranged 30–100 km with the period of 20–60 min including the eigen oscillation mode in various bays in that area.

http://dx.doi.org/10.5772/63762

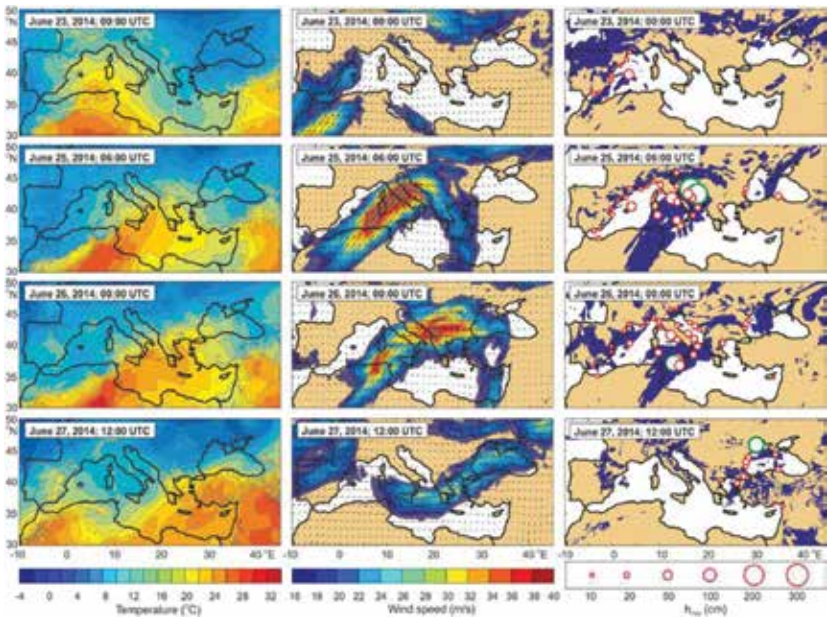

Figure 12. Propagation of the meteotsunamigenic synoptic pattern of 2014 together with the maximum heights of corresponding sea level oscillations at the times of the meteotsunami events. Left panels are 850 hPa air temperature, middle panels are 500 hPa wind and right panels are distribution of the unstable layer (Ri <0.25) in the mid-troposphere. (Šepić et al., 2015) [10].

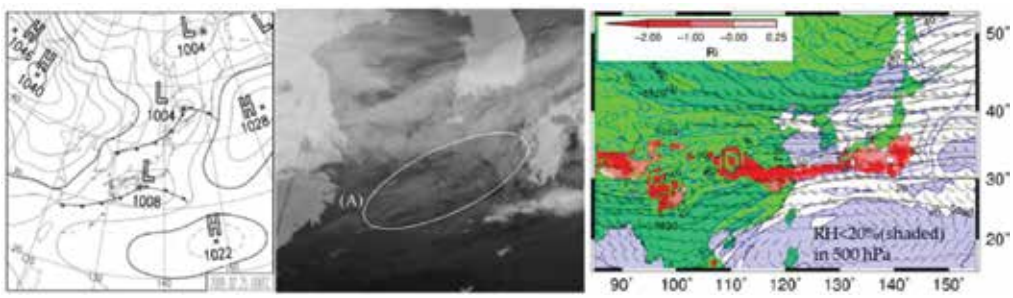

Figure 13. Weather condition of meteorological tsunami around the cold front on February 25, 2009. The surface weather chart (left), wavy clouds by satellite IR image (middle) and unstable layer covered with the East China Sea (right) [26].

7. Discussion and conclusion: the predictability of meteorological tsunami

The recent studies on meteorological tsunami presented that much more larger-scale motions played an important role in forming the atmospheric structures to generate meso-β or γ-scale

disturbances at sea level. Some latest papers pointed the importance of the (sub-) seasonal scale variation propagating from lower to mid-latitude.

Those findings in larger-scale motion will provide the capability for the prediction of the meteorological tsunamis from atmospheric and oceanographic aspects. It should be noticed that there have been much advances in technologies on observation, numerical modelling and others to make progresses scientifically in meteorological tsunamis. Especially, the high-performance computing technology brings us huge benefits to resolve the pressure disturbance in using numerical model such as the weather forecasting and research (WRF) model [46]. **Figure 14** illustrates a framework on the prediction of the meteorological tsunami. In obtaining a first guess, it is better to start the weather forecast in the synoptic scale with the duration of 2 or 3 days to make a first guess on the stability structure related to the wave duct or wave CISK. And then the downscaling run executes to resolve the atmospheric (mainly pressure) disturbance at sea level.

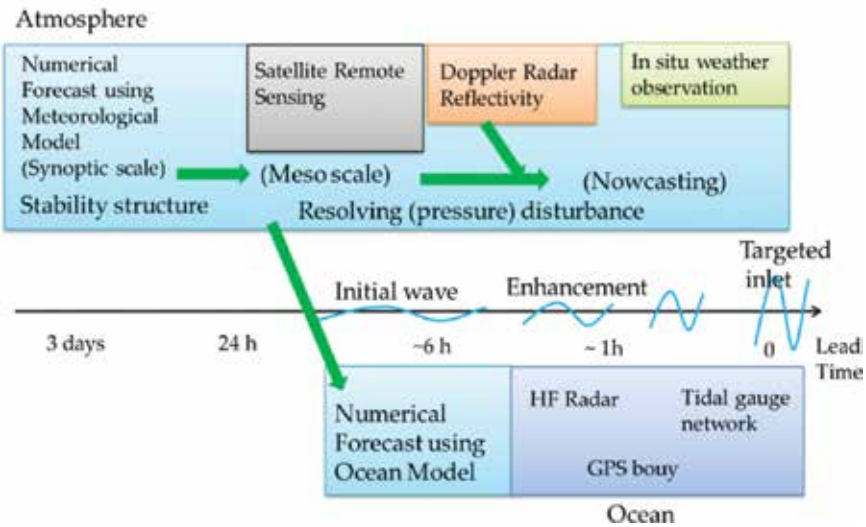

Figure 14. A framework on the prediction of the meteorological tsunami.

The infrared images of the satellite remote sensing have useful information if the sequence of the wavy clouds in the mid-troposphere moves fast over the ocean satisfying the Proudman resonance. A new geostationary meteorological satellite named Himawari-8 stated the operation in Asia-Australian region since July 2015. The Himawari-8 has 16-image channels of visible, near infrared, infrared bands, with the horizontal resolution of 0.5 (visible) to 2 km (infrared). The scan interval is every 10 min for global mode, and every 2.5 min for Japan area. The target such as typhoon or hurricane also scans for every 2.5 min for necessity. It will be much easier to see the propagation of the atmospheric wave using satellite data.

Although the mesoscale model can resolve the pressure disturbance to a considerable extent, it is not easy to apply directly into the ocean models as a surface boundary condition, because

of the difficulty in giving enough accuracy as compared to the in situ observation. Even small errors of the location, wave length, frequency, the propagation direction, etc. might affect the amplitude in the inlet. Indeed, Renault et al. (2011) [47] is the first to succeed the meteotsunami simulation by coupling of the WRF and ROMS (regional ocean modelling system) [48]. But the results of the pressure disturbance from the meteorological model should be treated very carefully. If the powerful computing resource is available, it is desirable to execute the ensemble run using various initial conditions, cloud physics parameter and boundary layer options for checking the uncertainty of the model behaviour.

The enhancement of the in situ observation network is one of the ways to provide a short-term prediction or real-time warning, in which the lead time is shorter than 1 h in many situations. It is convenient to install the automated station on isolated islands around the targeted area such as Adriatic Sea [49]. However, it seems not to be applicable such as US East Coast. The high-frequency (HF) radar extends the possibility for monitoring the meteorological tsunami propagation. Lipa et al. (2014) [50] detected the wave up to 23 km offshore, 47 min before reaching the shoreline by the analysis of HF radar signals on the June 2003 event on the US East Coast.

Indeed, further developments are required to get more accurate outputs for linking each processes, but we can believe that the day will come to predict the meteorological tsunami in a practical manner.

Author details

Kenji Tanaka* and Daiki Ito

*Address all correspondence to: k.tanaka.pb@cc.it-hiroshima.ac.jp

Department of Global Environment Studies, Faculty of Environmental Studies, Hiroshima Institute of Technology, Hiroshima, Japan

References

[1] Monserrat S., I. Vilibić, A.B. Rabinovich. Meteotsunamis: atmospherically induced destructive ocean waved in the tsunami frequency band. Nat. Hazards Earth Syst. Sci. 2006;6:1035–1051.

[2] Defant A. Physical Oceanography. New York, Oxford, London and Paris: Pergamon Press; 1962. pp. 234–235.

[3] Nomitsu T. A theory of tsunamis and seiches produced by wind and barometric gradient. Mem. Coll. Sci. Imp. Univ. Kyoto A. 1935;18:201–214.

[4] Proudman J. The effects on the sea of changes in atmospheric pressure. Geophys. J. Intl. 1929;2:197–209.

[5] Hibiya T., K. Kajiura. Origin of 'Abiki' phenomenon (kind of seiches) in Nagasaki Bay. J. Oceanogr. Soc. Jpn. 1982;38:172–182.

[6] Synolakis C.E. Green's law and the evolution of solitary waves. Phys. Fluids A. 1991;3(3):490–491.

[7] Greenspan H.P. The generation of edge waves by moving pressure distributions. J. Fluid Mech. 1956;1;574–592.

[8] Honda K., T. Terada, Y. Yoshida, D. Ishitomi. An investigation on the secondary undulation of oceanic tides. J. College Sci. Univ. Tokyo. 1908;24:113p.

[9] Rabinovich A.B. Seiches and harbor oscillations. In: Kim, Y.C., editors. Handbook of Coastal and Ocean Engineering. Singapore: World Scientific Publ.; 2009. pp. 193–236.

[10] Šepic J., I. Vilibić, A.B. Rabinovich, S. Monserrat. Widespread tsunami-like waves of 23–27 June in the Mideierranean and Black Sea generated by high-altitude atmospheric forcing. Sci. Rep. 2015;5:11682(8p.). DOI:10.1038/srep11682

[11] Vilibić I., J. Šepić. Desctructive meteotsunamis along the eastern Adriatic coast: overview. Phys. Chem. Earth. 2009;34:904–917.

[12] Vilibić I., S. Monseratt, A.B. Rabinovich, H. Mihanović. Numerical Modelling of the destructive meteotsunami of 15 June 2006 on the coast of the Baleatic Islands. Pure Appl. Geophys. 2008;165:2169–2195.

[13] Pattiaratchi I., C.B., E.M.S. Wijeratne. Are meteotsunamis an underrated hazard? Phil. Trans. R. Soc. A. 2015;373:20140377 (23p.). DOI: 10.1098/rsta.2014.0377

[14] Haslett S.R., H.E. Mellor, E.A. Bryant. Meteo-tsunami hazard associated with summer thunderstorms in the United Kingdom. Phys. Chem. Earth. 2009;34:1016–1022.

[15] de Jong M.P.C., L.H. Holtsuijsen, J.A. Battjes. Generation of seiches by cold fronts over the southern North Sea. J. Geophys. Res. 2003;104(C4):3117(10p.). DOI: 10.1029/2002JC001422

[16] Renqvist H. Ein Seebär in Finnland, Zur Frage Nach der Entstehung der Seebären. Geogr. Ann. 1926;8;230–236.

[17] Meteogroup in Netherlands. 'Meteotsunami' aan Nederlandse kust http://www.weer.nl/nieuws/detail/2012-01-04-meteotsunami-aan-nederlandse-kust/ (last view on Mar. 26, 2016).

[18] Wadgidsen web: Meteo-tsunami aan Nederlandse Kust 3 Januari 2012. http://wadgidsenweb.nl/nieuwsarchief/waddenzee2007-2012/536-meteo-tsunami.html, Updated on Feb. 5, 2012 (last view on Mar. 26, 2016).

http://dx.doi.org/10.5772/63762

[19] Ewing M., P. Rauhala, K.K. Kahma, T. Stipa, H. Boman, A. Kangas. Recent observations on the Finnish Coast. Nat. Hazards. 2014;74:197–215.

[20] Paxton C.H., D.A. Sobien. Resonant interaction between an atmospheric gravity wave and shallow water wave along Florida's West Coast. Bull. Amer. Meteor. Soc. 1998:79(12):2727–2732.

[21] Churcill D.D., S.H. Houston, N.A. Bond. The Daytona beach wave of 3–4 July 1992: a shallow-water gravity wave forced by a propagating squall line, Bull. Am. Meteor. Soc. 1995;76(1):21–32.

[22] Šepić J., A.B. Rabinovich. Meteotsunami in the great lakes and on the Atlantic coast of the United States generated by the 'derecho' of June 29–30, 2012. Nat. Hazards. 2014;74:75–107.

[23] Ewing M., F. Press, W.L. Donn. An exaplanation of the lake Michigan wave of 26 June 1954. Science. 1954;120:684–686.

[24] Thomson R.E., A.B. Rabinovich, I.V.Fine, D.C. Sinott, A. McCarthy, N.A.S. Sutherland, L.K. Neil. Meteorological tsunamis on the coasts of British Columbia and Washington. Phys. Chem. Earth. 2009;34:971–988.

[25] Akamatsu H. On seiches in Nagasaki Bay. Pap. Meteor. Geophys. (Meteorological Research Institute, Japan Meteorological Agency). 1982;33(2):95–115.

[26] Tanaka K. Atmospheric pressure-wave bands resulted in meteotsunami over the East China Sea on February 2009. Nat. Hazards Earth Syst. Sci. 2010;10(12):2599–2610.

[27] Ito D. On meteorological systems related to meteorological tsunamis over the East China Sea. Master Thesis, Hiroshima Institute of Technology. Hiroshima, Japan, 2016:138.

[28] Asano T., T. Yamashiro, N. Nishimura. Field observations of meteotsunami locally called 'abiki' in Urauchi Bay, Kami-Koshiki Island, Japan. Nat. Hazards. 2012;64:1685–1706.

[29] Tanaka K., S. Gohara, T. Koga, R. Yamaguchi, F. Yamada. Abiki oscillations in Sakitsu Bay, west Kyushu, Japan. Nat. Hazards. 2014;74:233–250.

[30] Tanaka K. On meteotsunamis around Tsushima Straits generated by the Baiu front. Nat. Hazards. 2012;63:805–822.

[31] Cho K-H., J-Y. Choi, K-S. Park, S-K. Hyun, Y. Oh, J-Y. Park. A synoptic study on tsunami-like sea level oscillations along the west coast of Korea using an unstructured-grid ocean model. J. Coastal Res. 2013;65:678–683.

[32] Wang X., K. Li, Z. Yu, J. Wu, Statistical characteristics of seiches of Longkou harbour. J. Phys. Oceanogr. 1987;17:1963–1966.

[33] Makarenko E., T. Ivelskaya. Meteotsunmai in the ports of Sakhalin region from the observational telemetry network of TWS. Navigation and Marine Researches, selected

reports of the 3rd Sakhalin regional marine scientific conf. Feb. 15–16, 2011: 205–210. ISSN 2227-4375.

[34] Pattriaratchi C., E.M.S. Wijeratne. Observations of meteorological tsunamis along the south-west Australian coast. Nat. Hazards. 2014;74:280–302.

[35] Goring D.G. Extracting long waves from tide-gauge records. J. Waterway Port Coast Ocean Eng. ASCE. 2008;134:306–312.

[36] Okal E.A., Y.NJ. Visser, C.H. de Beer. The Dwaskersbos, South Africa local tsunami of August 1969: field survey and simulation as a meteorological event. Nat. Hazards. 2014;74:251–268.

[37] Wertman C.A., R.A. Yabnosky, S. Yang, J. Merril, C.R. Kincaid, R.A. PackalMesoscale convective system surface pressure anomalies responsible for meteotsunamis along U.S. East Coast on June 13th, 2014. Sci. Rep.;9:7143(9p.). DOI: 10.1038/srep071

[38] NOAA Pacific Tsunami Warning Centre. Meteotsunami Animation: U.S. East Coast June 2013. https://www.youtube.com/watch?v=ykABRe5Yt3c.Uploaded on Dec. 8, 2013 (last view on Mar. 28, 2016).

[39] Kobayashi S., Y. Ota, Y. Harada, A. Ebita, M. Moriya, H. Onoda, K. Onogi, H. Kamahori, C. Kobayashi, H. Endo, K. Miyaoka, K. Takahashi. The JRA-55 reanalysis: general specifications and basic characteristics. J. Meteor. Soc. Jpn. 2015;93:5–48.

[40] Lindzen R.S., K.K. Tung. Banded convective activity and ducted gravity waves. Mon. Weather Rev. 1976;104:1602–1617.

[41] Lindzen R.S. Wave-CISK in the tropics. J. Atmos. Sci. 1974;31:156–179.

[42] Monserrat S., A.J. Thorpe. Using a ducting theory in an observed case of gravity waves. J. Atmos. Sci. 1996;53:1724–1736.

[43] Vilibić I., K. Horvath, N.S. Mahović, S. Monserrat, M. Maros, A. Amores, I. Fine. Atmospheric process responsible for generation of the 2008 Boothbay meteotsunami. Nat. Hazards. 2014;74:29–52.

[44] Lin Y.-L. Mesoscale dynamics. Cambridge: Cambridge University Press; 2007. p. 630.

[45] Belušić D., B. Grisono, Z.B. Kraić. Atmospheric origin of devastating coupled air-sea event in the east Adriatic. J. Geophys. Res. 2007;112:D17111. DOI:10.1029/2006JD008204

[46] Skmarock W.C., J.B. Klemp, A time-split nonhydrostatic atmospheric model for weather research and forecasting applications. J. Comput. Phys. 2008;227:3465–3485.

[47] Renault L., G. Vizono, A. Jansa, W.J. Tintore, Toward the predictability of meteotsunamis in the Balearic Sea using regional nested atmosphere and ocean models. Geophys. Res. Lett. 2011;38:L10461. DOI:10.1029/2011GL047361

[48] Shcheptickin A.F., J.C. McWilliams. The regional oceanic modelling system (ROMS): a split-explicit, free-surface, topography-following-coordinate ocean model. Ocean Modell. 2005;9:347–404.

[49] Šepić J., I. Vilibić. The development and implementation of a real-time meteotsunami warning network for the Adriatic Sea. Nat. Hazard Earth Syst. Sci. 2011;11:83–91.

[50] Lipa B., H. Parikh, D. Barrick, H. Roarty, S. Glenn. High frequency radar observation of the June 2013 US East Coast meteotsunami. Nat. Hazards. 2014;74:109–122. DOI: 10.1007/s11069-013-0992-4

Chapter 3

Tsunami Generation Due to a Landslide or a Submarine Eruption

Taro Kakinuma

Additional information is available at the end of the chapter

http://dx.doi.org/10.5772/64530

Abstract

Tsunamis can be triggered by not only submarine earthquakes, but also by landslides, and submarine volcanic eruptions. First, several characteristics of tsunami generation due to a landslide, or a sector collapse, are studied, with the tsunamis simulated numerically, to represent their generation through an interaction between falling bodies, and seawater, in two vertical dimensions. The falling body is assumed to be a fluid, or a rigid body, which moves down a slope with a constant gradient. Second, the mechanism of tsunami generation caused by a submarine volcanic eruption, is discussed, focusing on a phreatomagmatic explosion, where after exposure to high temperature magma, seawater evaporates instantly, with an explosive increase in its volume. An index for submarine volcanic explosive force, concerning tsunami generation, has been developed, by assuming the relationship between a phreatomagmatic explosion, and the resultant initial tsunami waveform. A numerical simulation was also generated, with a specific value for this index, for the propagation of tsunamis due to a submarine volcanic eruption in Kagoshima Bay, where a submarine explosion, leading to tsunami generation, has been observed.

Keywords: tsunami, landslide, sector collapse, submarine volcanic eruption, phreatomagmatic explosion

1. Introduction

A mega earthquake off the Pacific coasts of the Tohoku region, Japan, caused tsunamis, with an inundation height over 20 m, in 2011 (e.g., [1]). These tsunamis were generated by a rise, or a subsidence, in the seabed. For example, if a part of the seabed rises, owing to an underground fault movement, then the seawater over the deformation lifts, resulting in an increase in the

seawater's potential energy, then, in order to resolve this energy imbalance, waves, i.e., tsunamis are generated and travel in all available directions.

Tsunamis are, however, triggered not only by such a submarine earthquake, but also other phenomena as illustrated in **Figure 1**: landslide (e.g. [2]), sector collapse, glacier fall, submarine eruption, meteorite impact, and others. In the latter cases, where a tsunami source is not directly connected to an earthquake, the wave height of generated tsunamis could be underestimated or be beyond estimation, by the general prediction for tsunamis based on only seismic data, as in cases with a tsunamigenic earthquake [3]. In this chapter, we concentrate our discussion on tsunami generation caused by landslide, or submarine eruption.

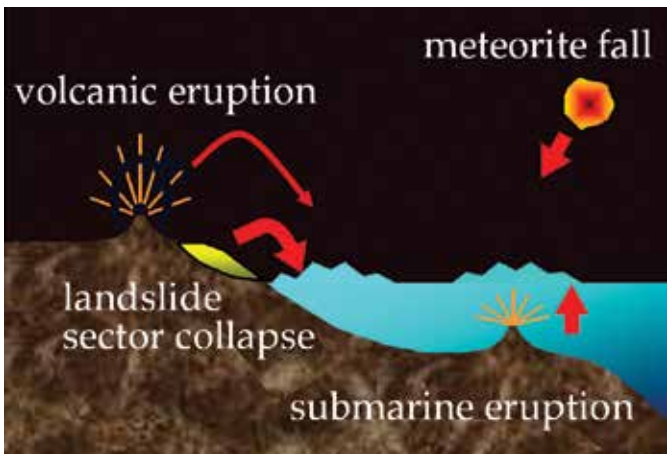

Figure 1. An illustration for examples of tsunami sources.

Figure 2. A huge boulder, which was proposed to have been carried by tsunamis, on Ishigaki Island, Japan. This photo was taken in 2013, and provided by Dr. T. Iribe. He is the person in this photo and is 1.71 m tall.

http://dx.doi.org/10.5772/64530

First, we will study several characteristics of tsunamis induced by landslides, or sector collapses. It is proposed that the 1771 Meiwa Earthquake Tsunami occurred owing to a submarine landslide, for although the earthquake was not strong according to the Japanese archive, huge boulders on Ishigaki Island, Japan, were determined to have been carried by the tsunamis [4]. Shown in **Figure 2** is a boulder supposed to have been carried by an older tsunami, which hit the same island. In 1792, the tsunamis due to a landslide, or a sector collapse, at Mt. Mayu, Japan, traveled over the Ariake Sea, resulting in a runup on the opposite shore, which killed more than 15,000 people [5]. **Figure 3(a)**, and **3(b)**, show the eroded slope of Mt. Mayu, and the view of its opposite side, respectively; the distance between them is about 20 km. Such tsunamis are not necessarily generated only by sands or rocks: an excursion ship could be hit by tsunamis, due to a partial collapse of glacier near a coast on Svalbard Islands, Norway [6].

Figure 3. The eroded slope of Mt. Mayu in Nagasaki Prefecture (a), and the view of its opposite side in Kumamoto Prefecture (b). The distance between them is about 20 km. The author took these photos in 2012.

These tsunamis are generated through an interaction between water motion, and falling bodies, such that the tsunami generation process is rather complicated. An experimental study on tsunami generation due to a rigid object sliding down a slope, was reported by e.g. Wiegel [7], while tsunami generation due to particles moving down a slope, was studied by e.g. Walder et al. [8], and Shigihara et al. [9], using sands for falling bodies, Shigematsu and Kohno [10] glass beads, and Mohammed and Fritz [11] naturally rounded river gravel. In the laboratory experiments by Riu et al. [12], the falling bodies were glass balls with different diameters, glass beads, natural stones, acrylic rock-shape blocks, ice balls, etc.

Tsunami generation due to a landslide, has been also investigated numerically, using various methods (e.g., [13–21]). Wu and Liu [22] had simulated tsunami generation from a rigid wedge sliding down a slope, using a modified volume of fluid (VOF) method, as well as a moving boundary algorithm, and compared their three-dimensional numerical results, with the corresponding experimental data obtained by Raichlen and Synolakis [23]. In this chapter, we

will study several fundamental characteristics of tsunami generation caused by a landslide, or a sector collapse, on the basis of two-dimensional vertical results, obtained through a numerical simulation using a moving particle semi-implicit (MPS) model [24], where the falling body is assumed to be a fluid, or a rigid body, which moves down a slope with a constant gradient.

Second, we examine tsunamis caused by a submarine eruption. When a submarine explosive eruption occurs, volcanic products are blown out, as in case for an explosion from a subastral active volcano. Conversely, if some volume of magma is released out of a chamber, owing to a submarine volcanic eruption, ground subsidence occurs, leading to a creation of a caldera. Although both volcanic products, and a caldera, should cause tsunamis as mentioned by Egorov [25], and Maeno et al. [26], respectively, we take up a different tsunami source, peculiar to a submarine eruption, for discussion in this chapter, i.e., a phreatomagmatic explosion [27]. In the process with a submarine phreatomagmatic explosion, seawater contacts high temperature magma in the seabed neighborhood, after which the seawater evaporates with an explosive increase in its volume, resulting in a water surface displacement that generates tsunamis. A new index for submarine volcanic explosion, concerning tsunami generation, is developed by assuming the relationship between a phreatomagmatic explosion, and the resultant initial tsunami waveform. We specifically assume the value of this index, to generate a numerical simulation for tsunamis caused by a submarine volcanic eruption in Kagoshima Bay, Japan, where a submarine explosion with tsunami generation has been observed [28].

2. Tsunamis due to a landslide or a sector collapse

2.1. Numerical model

Numerical computations have been performed that represent tsunami generation due to a body, which moves down a slope. In the present calculation, the numerical model, developed by Iribe and Nakaza [24], based on the MPS method designed by Koshizuka and Oka [29], is applied to consider the furious water motion. The water surface level is determined using the spatial gradient of particle-number density, to inhibit pressure disturbance at the water surface. No turbulence model is utilized for fluid motion, and both the elasticity, and the plasticity, of the falling bodies are neglected for simplicity.

2.2. Model validation for tsunami generation due to a falling fluid

2.2.1. Experimental setup

In order to validate the applicability of the numerical model, several numerical results for water surface displacements, are compared with the corresponding experimental data. **Figure 4** depicts a setup for laboratory experiments, with an acrylic basin, where h_{off} denotes the still water depth off of the slope, i.e., the offshore still water depth, and the water density is 1000 kg/m^3. The vertical steel gate, installed on a slope with a constant gradient of β, can be pulled up quickly, and smoothly, by operating two levers as shown in **Figure 5**, resulting in the

http://dx.doi.org/10.5772/64530

release of objects, stacked on the onshore side of the gate. When the gate is closed, its bottom edge touches the shoreline in the still water condition. The height of the falling-body front face along the vertical gate, is denoted by h_s. In the experiments for model validation, the falling body is water, with the same density as that of the offshore water, i.e., 1000 kg/m^3.

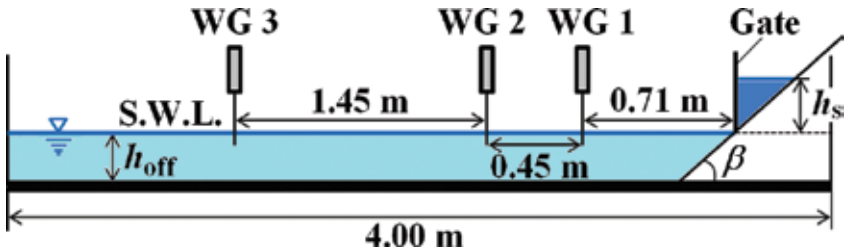

Figure 4. The hydraulic basin with a slope on which a gate is installed. The basin width is 2.0 m.

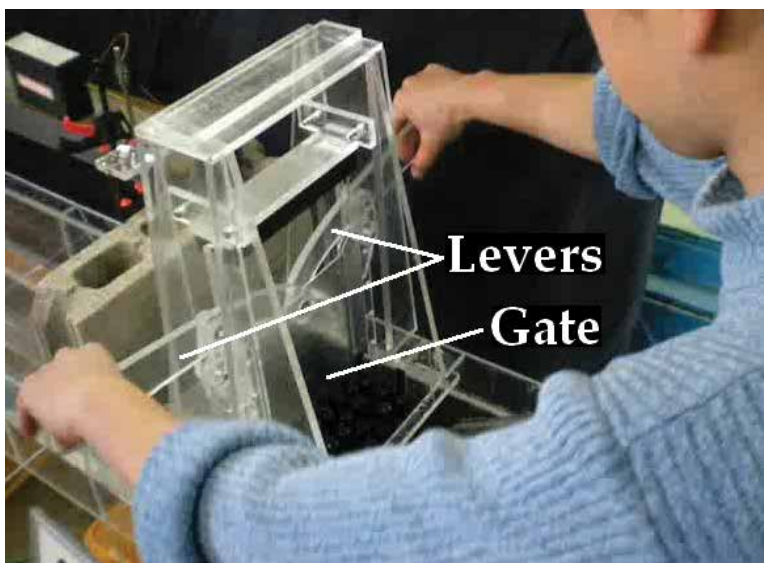

Figure 5. The gate, with two levers, set on the slope in the hydraulic basin as shown in **Figure 4**.

2.2.2. Calculation conditions

In the model computation, 17,000 particles are used to represent the above-described initial condition, where the particle grid is 0.005 m for the MPS model. In the present calculation, the numerical results for water surface displacements in the case where the particle grid is 0.005 m, are in good agreement with the case where the particle grid is 0.01 m. The water density on both the offshore side, and the onshore side, of the gate is 1000 kg/m^3. The water on the onshore side of the gate, starts at the initial falling time, i.e., t = 0.0 s.

2.2.3. Comparison between the numerical results and the corresponding experimental data for water surface displacements

Shown in **Figure 6** are the numerical results for the water surface displacements, at the location for wave gauge (WG) 2 shown in **Figure 4**, in comparison with the corresponding experimental data. The slope gradient β is 30°, and 45°, in the cases shown in **Figure 6(a)**, and **6(b)**, respectively. The offshore still water depth h_{off}, and the initial falling-body height h_s, are 0.1 m, and 0.15 m, in both the cases. The distance between the location for WG 2, and that for the gate, is 1.16 m. The experimental value for each case, is a mean value among values obtained through five runs of the experiment, with the same initial conditions. **Figure 6** indicates that, both the wave height, and the wave phase, of the first wave obtained using the MPS model, are in harmony with the experimental results.

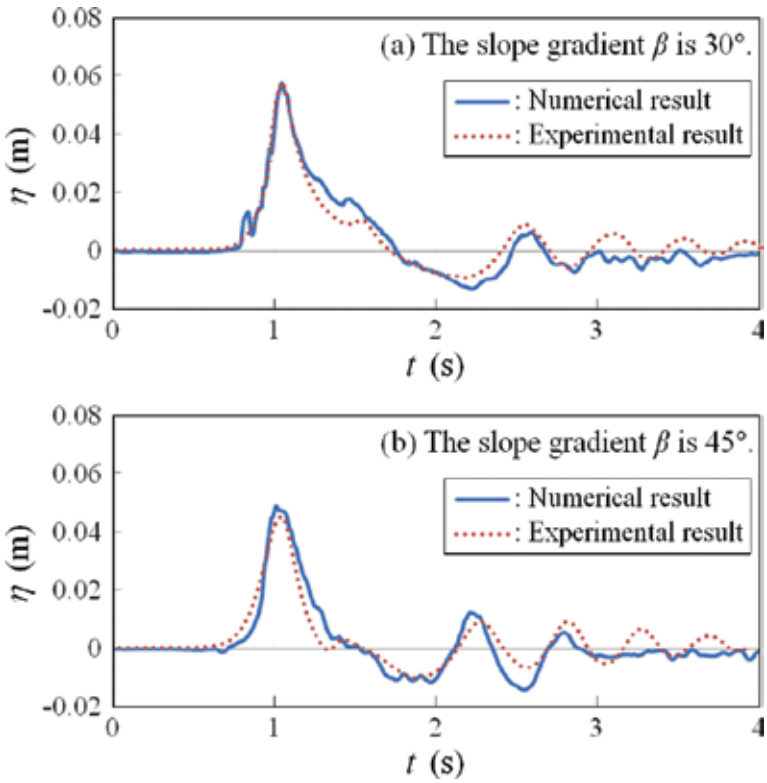

Figure 6. The water surface displacement at the location for WG 2 shown in **Figure 4**. The falling body is water, with the same density as that for the offshore water, i.e., 1000 kg/m^3. The offshore still water depth h_{off} is 0.1 m and the initial falling-body height h_s is 0.15 m.

2.3. Tsunami generation due to a falling fluid

Two-dimensional vertical motion in a water basin shown in **Figure 7**, is simulated numerically, where the slope gradient β is 30°, and the distance between the slope foot, and the offshore

http://dx.doi.org/10.5772/64530

vertical wall, is 3.5 m. The offshore still water depth h_{off} is 0.1 m, or 0.2 m. Also in the following computation, the offshore water density is 1000 kg/m^3, and the particle grid is 0.005 m.

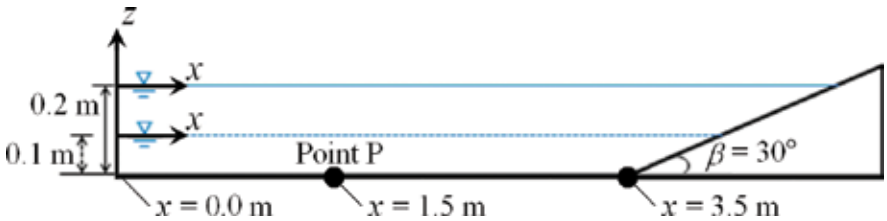

Figure 7. The target domain for computation, where the offshore still water depth h_{off} is 0.1 m, or 0.2 m; the slope gradient β is 30°.

Sketched in **Figure 8** are the initial positions of a falling body in Cases 1–4, where the initial level of the falling-body bottom from the seabed, is 0.1, 0.2, 0.3, and 0.4 m, respectively, whether the offshore still water depth h_{off} is 0.1 or 0.2 m. The initial shape of the falling body is a right triangle, where the height of its vertical front face is 0.1 m. The body on the slope starts at the initial falling time, i.e., t = 0.0 s. The falling body is assumed to be a fluid, or a rigid body. The fluid, and the rigid body, with the same density as that of the offshore water, i.e., 1000 kg/m^3, we call, a "light fluid" and a "light rigid body", respectively, while the fluid and the rigid body, with a density of 2600 kg/m^3, we call, a "heavy fluid" and a "heavy rigid body", respectively.

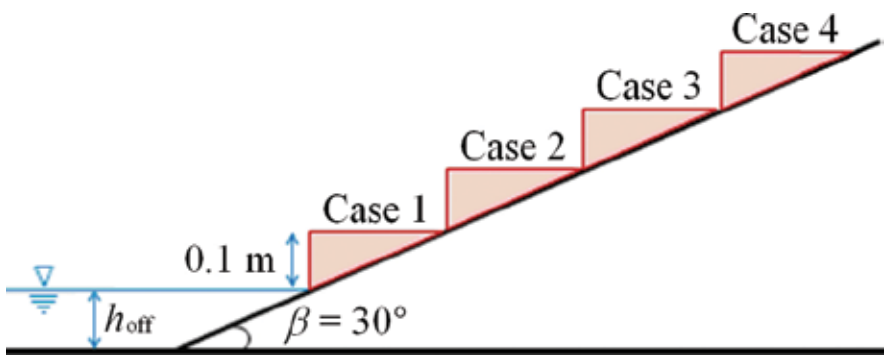

Figure 8. A sketch of the initial positions of a falling body in Cases 1–4.

Figure 9 shows the numerical results for the water surface displacements at Point P, in Cases 1–4, when the falling body is a light fluid, and the offshore still water depth h_{off} is 0.1 m. The distance between the location for Point P, and that for the offshore vertical wall, is 1.5 m, as shown in **Figure 7**. If the vertical distance between a particle, and its nearest particle below it, is larger than the particle grid, i.e., 0.005 m, then the upper particle is defined as a droplet, which is located over a particle at the water surface, around the horizontal location for the upper particle.

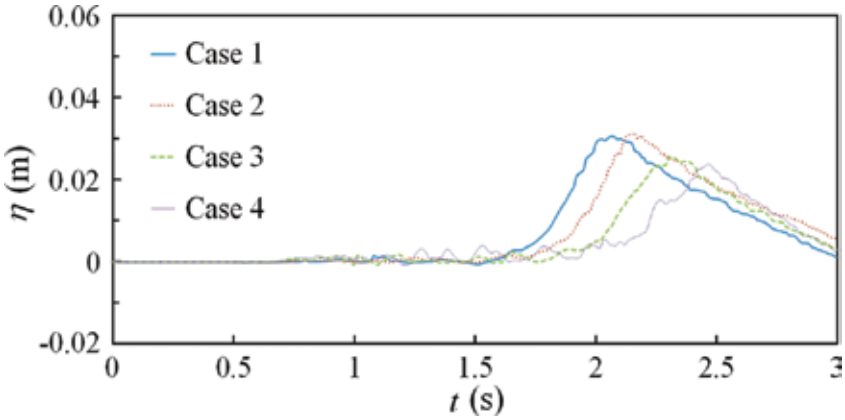

Figure 9. The water surface displacements at Point P (x = 1.5 m) for the different initial positions of a falling light fluid, with a specific gravity of 1.0. The offshore still water depth is 0.1 m.

Conversely, in **Figure 10** are the numerical results for the water surface displacements at Point P, in Cases 1–4, where the falling body is a heavy fluid, and the offshore still water depth h_{off} is 0.1 m. The tsunami height is defined as the maximum value in water surface displacement at each location. In each of our cases, the tsunami height from the heavy fluid is twice as large as that from the light fluid. Thus, if both the initial position, and the volume, of a falling body are the same, the tsunami height increases as the density, i.e., the initial potential energy, of the falling body is increased.

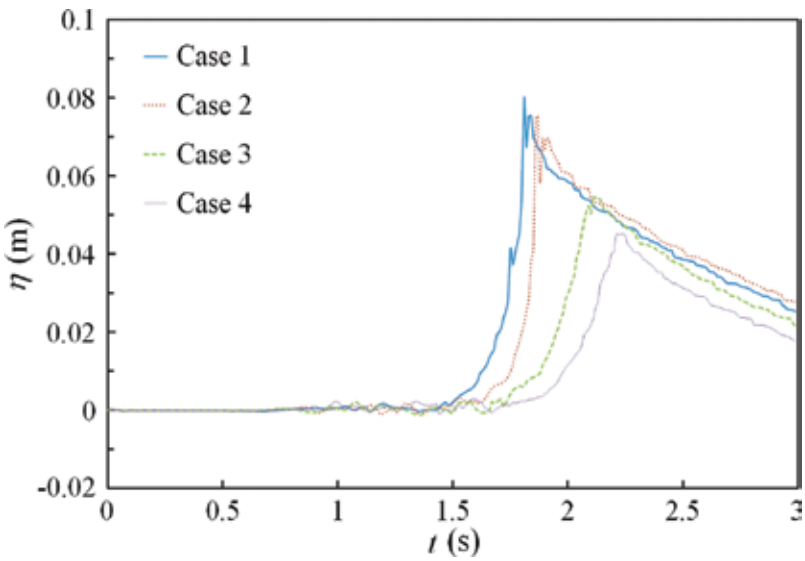

Figure 10. The water surface displacements at Point P (x = 1.5 m) for the different initial positions of a falling heavy fluid with a specific gravity of 2.6. The offshore still water depth is 0.1 m.

http://dx.doi.org/10.5772/64530

However, it is in Case 4, where the falling-body initial potential energy is largest, that the tsunami height at Point P, is the minimum value, whether the falling body is a light fluid, or a heavy fluid, as shown in **Figure 9**, or **10**, respectively. Conversely, the tsunami height at Point P, is the maximum value in Case 2, when the falling body is a light fluid, as shown in **Figure 9**, while in Case 1, when the falling body is a heavy fluid, as shown in **Figure 10**. How is this possible?

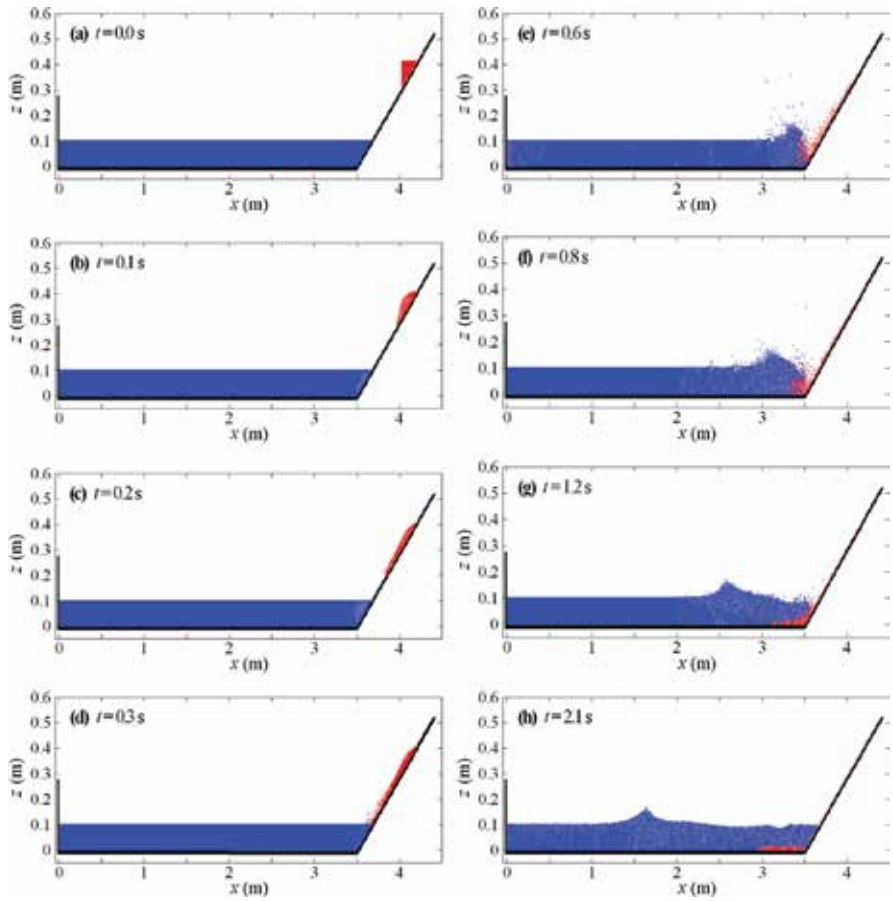

Figure 11. The simulation result for the particle motion in Case 3, where the falling body is a heavy fluid with a specific gravity of 2.6; the offshore still water depth is 0.1 m. The red points denote the falling-fluid particles, while the blue ones the offshore-water particles.

The particle motion numerical result for Case 3, is shown in **Figure 11**, where the falling body is the heavy fluid, and the offshore still water depth h_{off} is 0.1 m. The red points denote the heavy-fluid particles, while the blue ones the offshore-water particles. **Figure 11** indicates that when the initial position of a falling body is high, the falling-body group while moving down a slope, transforms and flattens, resulting in a flattened body rushing into the water, such that

the volumetric flow rate of the falling body decreases, and pushes the water weakly. This is the reason why the tsunami height at Point P, is lower in Case 4, where the falling-body initial potential energy is large, when the falling body is the heavy fluid, and also for the light fluid.

2.4. Tsunami generation due to a falling rigid body

Shown in **Figure 12** are the numerical results for the water surface displacements at Point P, in Cases 1–4, when the falling body is a light rigid body, and the offshore still water depth h_{off} is 0.1 m. The tsunami height at Point P, shows its maximum value in Case 4, where the falling-body initial potential energy is largest. This is not true when the falling body is a light fluid, or a heavy fluid, as described above.

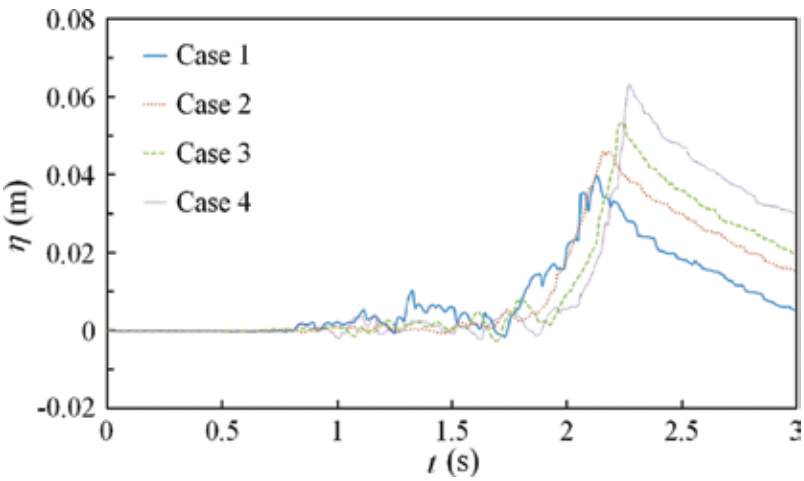

Figure 12. The water surface displacements at Point P (x = 1.5 m) for the different initial positions of a falling light rigid body with a specific gravity of 1.0. The offshore still water depth is 0.1 m.

On the other hand, shown in **Figure 13** are the numerical results for the water surface displacements at Point P, in Cases 1–4, when the falling body is a heavy rigid body, and the offshore still water depth h_{off} is 0.1 m. The tsunami height at Point P, is lowest in Case 4, where the falling-body initial potential energy is largest. This is another challenge!

The particle motion numerical result for the Case 3, is shown in **Figure 14**, where the falling body is the heavy rigid body, and the offshore still water depth h_{off} is 0.1 m. The red points denote the rigid-body particles, while the blue ones the offshore-water particles. The front face of the falling rigid body pushes the water, generating a large wave height plunging-type wave, after which a turbulent tsunami propagates, with a bore, generated at its front face. Thus in both the generation, and the propagation, of this tsunami, the energy loss is larger, owing to the generation of splashes, the turbulence, and the bore. This is the reason why the tsunami height at Point P, is lower in Case 4, in which the falling-body initial potential energy is large, when the falling body is a heavy rigid body. It should also be noted that the water surface profile for this tsunami, is forwardly inclined, such that the peak in the water surface

http://dx.doi.org/10.5772/64530

displacement at Point P, appears earlier in **Figure 13**, in the case of the falling heavy rigid body, than in **Figure 12**, concerning the falling light rigid body.

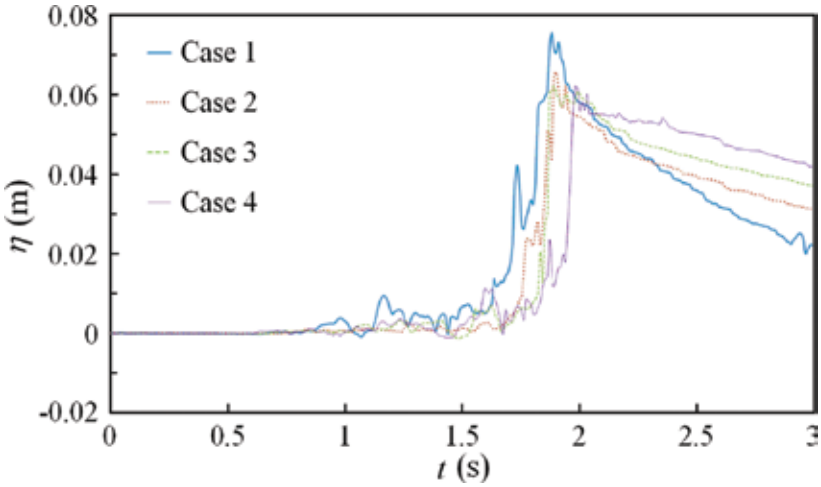

Figure 13. The water surface displacements at Point P (x = 1.5 m) for the different initial positions of a falling heavy rigid body with a specific gravity of 2.6. The offshore still water depth is 0.1 m.

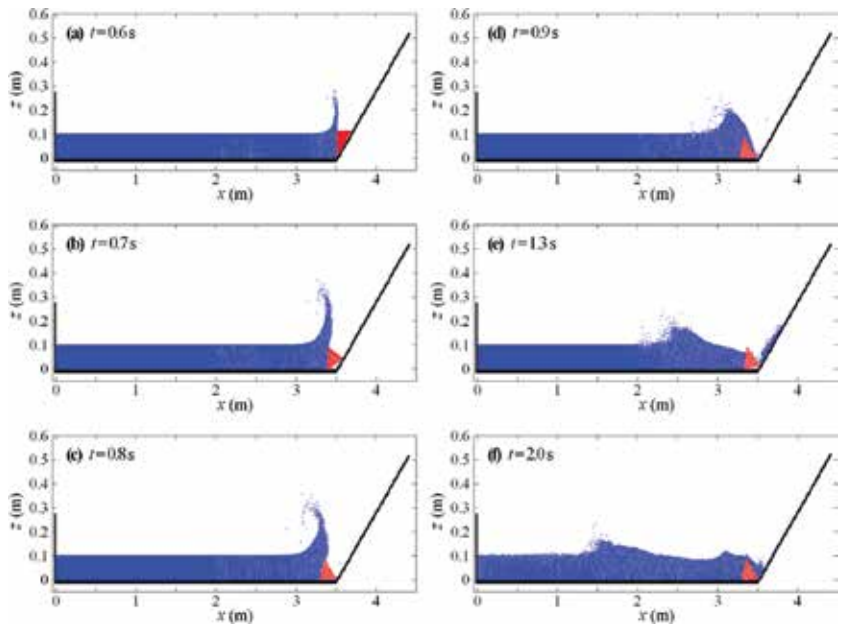

Figure 14. The simulation result for the particle motion in Case 3, where the falling body is a heavy rigid body with a specific gravity of 2.6; the offshore still water depth is 0.1 m. The red points denote the rigid-body particles, while the blue ones the offshore-water particles.

2.5. Effect of the offshore still water depth on tsunami generation due to a falling body

The numerical results for the tsunami-height distribution are shown in **Figure 15(a)**, and **15(b)**, where the offshore still water depth h_{off} is 0.1 m, and 0.2 m, respectively, when the falling body is a light fluid. As the offshore still water depth decreases, the tsunami height near the gate, i.e., the shoreline increases, as shown in **Figure 15(a)**, for the falling body does not move seabed seawater. With less volumetric flow rate wasted, the falling body contributes to tsunami-height growth, while it progresses near the seabed. Note, however, that as the offshore still water depth decreases, there is decreased rate in the tsunami height in tsunami propagation, which increases especially for 2.0 m ≤ x ≤ 2.5 m, as shown in **Figure 15(a)**.

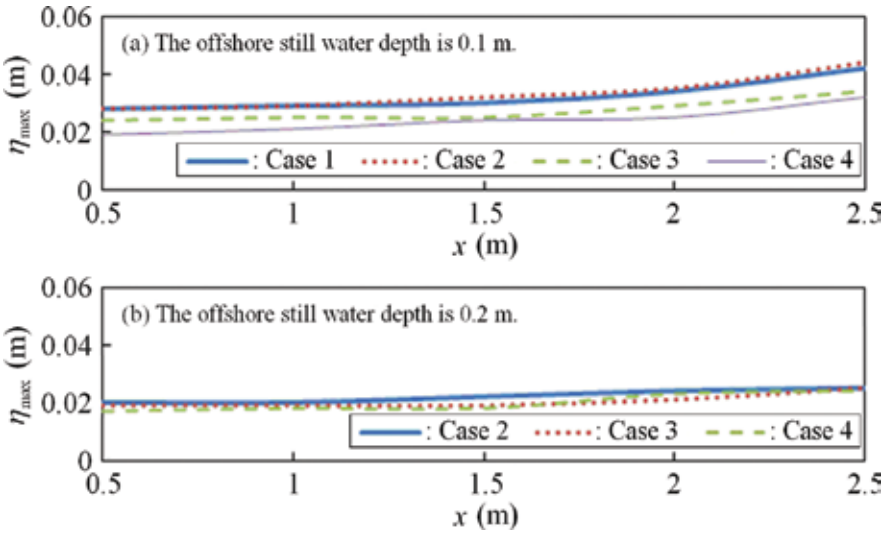

Figure 15. The distributions of the tsunami height η_{max} for the different initial positions of a falling light fluid with a specific gravity of 1.0.

2.6. Tsunami generation due to a submarine landslide

Two-dimensional vertical motion in a water basin, as illustrated in **Figure 16**, is numerically simulated to examine tsunami generation due to a submarine landslide. The slope gradient β is 45°, the offshore still water depth h_{off} is 0.305 m, and the offshore water density is 1000 kg/m^3. The particle grid is 0.005 m, the same as in the present computation. The initial level of a falling-body bottom from the offshore still water level, is −0.205, −0.105, 0.0, 0.1, and 0.2 m in Cases U1, U2, O1, O2, and O3, respectively, such that the falling body is under sea level even at the initial falling time in both Case U1, and Case U2, creating a submarine landslide, whereas the falling body is above sea level at the initial falling time in Cases O1, O2, and O3, with a subaerial landslide. The falling body is a heavy fluid, with a density of 2600 kg/m^3, and the initial shape of the falling body is an isosceles right triangle, where the initial height of its vertical front face is 0.105 m, in all cases.

http://dx.doi.org/10.5772/64530

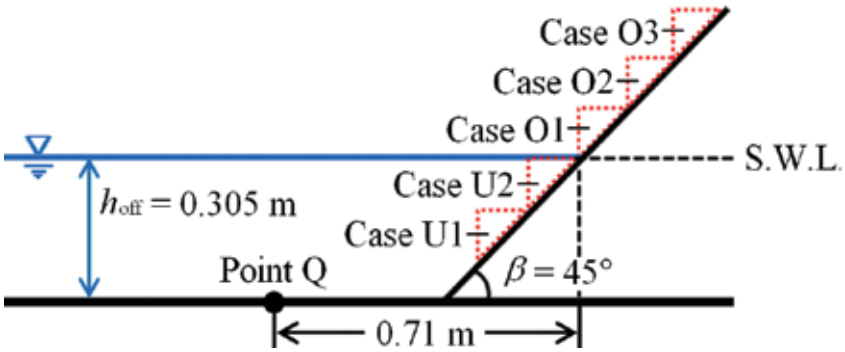

Figure 16. A sketch of the initial positions of a falling body, in Cases U1, and U2, with a submarine landslide, and Cases O1, O2, and O3, with a subaerial landslide. The offshore still water depth h_{off} is 0.305 m, and the slope gradient β is 45°.

Shown in **Figure 17** are the numerical results for the water surface displacements at Point Q, where the distance between the location for Point Q, and that for the shoreline in still water, is 0.71 m, as shown in **Figure 16**. **Figure 17** indicates that the tsunami height is lower when a falling body is initially submerged, as in both Case U1, and Case U2, the reason for which is the third question.

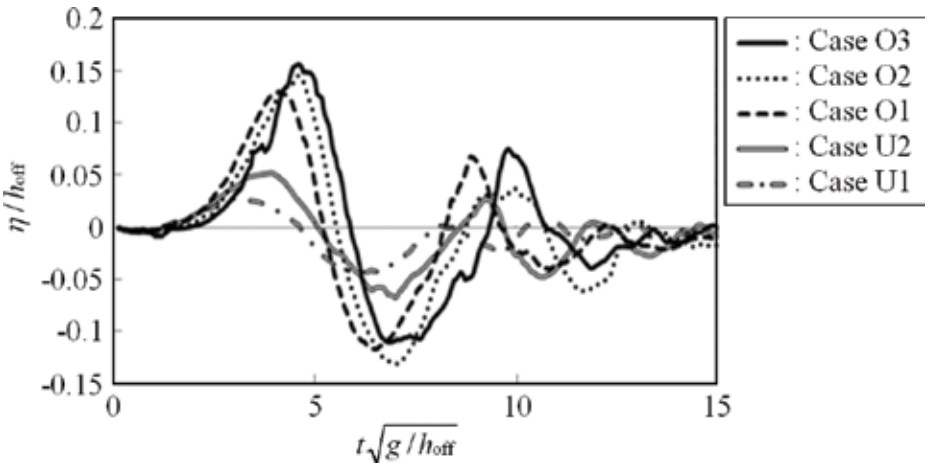

Figure 17. A relative value for the water surface displacement η at Point Q, indicated in **Figure 16**, where the falling body is a heavy fluid, with a specific gravity of 2.6. The offshore still water depth is 0.305 m, and g denotes gravitational acceleration, i.e., 9.8 m/s^2.

In the cases with a submarine landslide, a falling body is surrounded by seawater, from the time falling starts. In both Case U1, and Case U2, the density ratio between the falling heavy fluid, and the offshore water, is 2600 kg/m^3/1000 kg/m^3 = 2.6, which is much smaller than the density ratio between the falling heavy fluid, and the air, i.e., about 2600 kg/m^3/1.0 kg/m^3 = 2600. Thus the initial relative potential energy of a submerged falling body is lower, resulting

in a slower motion, with a smaller volumetric flow rate, in the falling body. This is the reason why the tsunami height is lower in the cases where the submarine landslide occurs than in the cases where the landslide occurs above the offshore water level.

3. Tsunamis due to a submarine eruption with a phreatomagmatic explosion

3.1. Submarine explosive index concerning tsunami generation

3.1.1. Cubic expansion of water through heat-induced evaporation

In this section, the process of tsunami generation due to a submarine volcanic eruption, is discussed considering a phreatomagmatic explosion, where the seawater touches high temperature magma in the seabed neighborhood, after which the water evaporates instantaneously with explosive increase in its volume, lifting the water over the water vapor bubble. We will develop a model for tsunami generation due to a submarine eruption with phreatomagmatic explosion, and introduce a submarine explosive index concerning the relationship between the submarine phreatomagmatic explosion, and the resultant initial tsunami height.

Remember the following characteristics of water: the mass, and the density, of 1.0 mol of liquid water, are around 18.0 g, and 1.0 g/cm^3, respectively, such that 1.0 mol of liquid water, occupies a volume of 18.0 ml. Conversely, 1.0 mol of vapor, assumed to be an ideal gas, occupies a volume of 22,700 ml at the standard temperature and pressure (STP), where the temperature, and the pressure, are 0.0°C, and 1.0 bar, i.e., 1.0×10^5 Pa, respectively. Thus, when liquid water transforms to vapor at STP, the volume of the vapor becomes $22{,}700/18.0 \approx 1.261 \times 10^3$ times as much as that of the liquid water.

If the pressure is p (Pa), then the volume of a gas at temperature τ (°C), V, is evaluated by $V = V_0\,(10^5/p)\,(1 + \tau/273)$ according to Boyle-Charles' law, where V_0 denotes the volume of the gas at 0.0°C.

Consequently, when liquid water with a volume of V_w at STP, transforms to vapor with a volume of V at τ(°C), and p (Pa), the volume expansion ratio between liquid water, and vapor, is

$$\alpha = V / V_w = 1.261 \times 10^8 \left(1 + \tau / 273\right) / p. \tag{1}$$

3.1.2. Volume expansion ratio of water through a phreatomagmatic explosion

Immediately after magma touches water, the following equation explains their interface [30]:

$$(\tau_m - \tau_i) / (\tau_i - \tau_w) = (\rho_w c_{pw} k_w / \rho_m c_{pm} k_m)^{1/2}, \tag{2}$$

http://dx.doi.org/10.5772/64530

where τ_i is the temperature at the interface between magma and water; ρ, c_p, and k are density, isopiestic specific heat, and heat transfer coefficient, respectively; the subscripts m, and w, denote the variables of magma, and water, respectively. The general values of these parameters are as follows [26]:

[The general values of the parameters for magma]

Density $\rho_m = 2400$ kg/m^3

Temperature $\tau_m = 973$ K

Isopiestic specific heat $c_{pm} = 1.2 \times 10^3$ J/kgK

Heat transfer coefficient $k_m = 1.2$ W/mK

[The general values of the parameters for water]

Density $\rho_w = 1000$ kg/m^3

Temperature $\tau_w = 273$ K

Isopiestic specific heat $c_{pw} = 4.2 \times 10^3$ J/kgK

Heat transfer coefficient $k_w = 0.61$ W/mK

We substitute these general values into Eq. (2), and obtain the temperature at the interface, τ_i, as

$$\tau_i = 649.0 \text{ K} = 376.0°\text{C}. \tag{3}$$

This value is larger than the spontaneous nuclear generation temperature of water, which is approximately 583 K at 1.0 atm. Note that the temperature increases by around 10.0 K as the pressure is increased by 2.0 MPa [26].

3.1.3. Relationship between the still water depth and the volume expansion ratio for seawater near the seabed

The water pressure at a submarine crater in still water, p, is defined as

$$p = \rho_w g h = 9800\, h(\text{Pa}) \ (\text{unit length in meter}), \tag{4}$$

where h denotes the still water depth at the crater location, and the gravitational acceleration g equals 9.8 m/s^2. Substituting the value of τ_i shown in Eq. (3), and the value of p given by Eq. (4), into τ, and p, in Eq. (1), respectively, leads to

$$\alpha = V / V_w = 30{,}600 / h(\text{unit length in meter}), \tag{5}$$

where the water surface displacement is assumed to be much smaller than the still water depth. Eq. (5) determines the relationship between the volume expansion ratio of water over the crater, and the still water depth at the crater location; for instance, $\alpha \approx 10.2$ when h is 3000 m, while $\alpha \approx 6.1 \times 10^2$ when h is 50 m.

3.1.4. Relationship between the submarine volcanic explosion and the initial tsunami profile

Assume that a circular crater (indicated with "A" in **Figure 18**) with a radius of r, appears at the horizontal seabed, with the seawater (B) over the crater then being vaporized to expand vertically in an instant (C), such that the initial tsunami profile becomes a cylinder (D) with a height of η_0. E in **Figure 18** indicates the still water surface, where the still water depth is h. Although in case with a seabed rise, the initial tsunami height decreases, as the seabed-rise speed decreases, and also as the still water depth increases, as described by Kakinuma and Akiyama [31], these effects on tsunami generation are neglected for simplicity. Thus both the shape, and the size, of the cylinder D, are the same as that of the cylinder C, such that the volume of these cylinders, V, equals $\pi r^2 \eta_0$, where η_0 is the initial tsunami height.

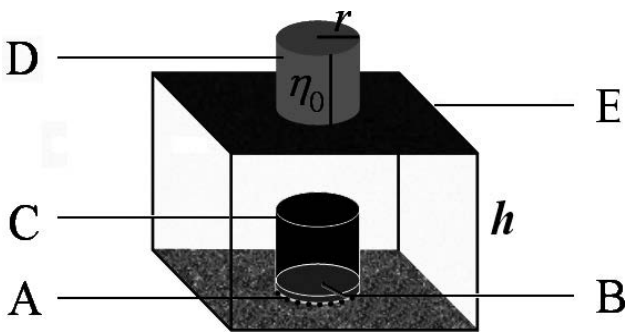

Figure 18. A schematic for tsunami generation due to a submarine phreatomagmatic explosion. "A" denotes a crater with a radius of r, at the seabed; "B" the original water with a volume of V_w, before vapor transformation; "C" the generated vapor with a volume of V; "D" the initial tsunami profile with a radius of r, and a height of η_0; "E" the still water surface, where the still water depth is h.

By substituting $V = \pi r^2 \eta_0$ into Eq. (5), we obtain:

$$V_w = \pi r^2 \eta_0 h / 30,600 \approx 1.0 \times 10^{-4} r^2 \eta_0 h \left(\text{unit length in meter}\right), \tag{6}$$

where V_w is the original volume of the seawater (B), before vapor transformation. Eq. (6) indicates that the cylindrical initial tsunami profile with a radius of r, and a height of η_0, is generated when a submarine eruption, transforms water with a volume of V_w at the seabed neighborhood, to vapor, where the still water depth is h. If we know all the values of V_w, r, and h, then we can evaluate the value of the initial tsunami height η_0. Therefore, the original volume of seawater, which transforms to vapor through a phreatomagmatic explosion caused by it

http://dx.doi.org/10.5772/64530

touching high temperature magma, i.e., V_w, is a submarine explosive index concerning tsunami generation.

On the other hand, if we assume that the seawater over a crater is vaporized, becoming a half sphere with a radius of R, where the sphere center coincides with the crater center at the seabed, then the sphere volume V is $2\pi R^3/3$. If we assume also that the initial tsunami profile is a half sphere, with a radius of R, then we obtain

$$V_w \approx 6.8 \times 10^{-5} R^3 h \left(\text{unit length in meter}\right), \tag{7}$$

where V_w is the original volume of the seawater, before vapor transformation. Eq. (7) can be rewritten to

$$R \approx 24 \left(V_w / h\right)^{1/3} \left(\text{unit length in meter}\right). \tag{8}$$

According to an old document, the initial tsunami height η_0 was around 9 m, owing to a submarine volcanic eruption in Kagoshima Bay, Japan, on September 9, 1780 [27], where the still water depth at the eruption location is about 200 m. In this case, we substitute both R = 9 m, and h = 200 m, into Eq. (7), resulting in V_w = 9.9 m^3. It should be noted, however, that future work is required to know accurately both the profile, and the size, of the initial tsunami, for instance, by performing laboratory experiments using both high temperature material, and water.

3.2. Numerical simulation for propagation of tsunamis due to a submarine phreatomagmatic explosion in a bay

3.2.1. Examples of values of the submarine explosive index concerning tsunami generation

The relationship between the crater radius r, and the eruption amount V_e, is expressed by Sato and Taniguchi [32] as

$$r = 0.97 V_e^{0.36} \left(\text{unit length in meter}\right). \tag{9}$$

For example, the volcanic explosive index (VEI) introduced by Newhall and Self [33], is assumed to equal three, larger than two for a standard explosion, then the eruption amount V_e is between 1.0×10^7 m^3 and 1.0×10^8 m^3; hence the crater radius r becomes approximately between 321 m and 736 m, based on Eq. (9). Thus we assume that the crater radius r is 700 m, in the present computation. Conversely, owing to the submarine explosion in Kagoshima Bay on September 9, 1780, the sea level rose by around 9 m over the explosion, as described above, such that we assume that the initial tsunami height η_0 is 9.0 m. If the initial tsunami profile becomes a cylinder, as shown in **Figure 18**, then the value of submarine explosive index

concerning tsunami generation, V_w, is evaluated by Eq. (6) as 2.3×10^4 (unit length in meter) when the still water depth at the eruption location, h, is 50 m, while 4.5×10^4 (unit length in meter) when h is 100 m.

3.2.2. Numerical model and calculation conditions

Numerical simulation for tsunamis due to a submarine volcanic eruption in Kagoshima Bay, is generated using the shallow water version of the nonlinear wave model [34], where the computational program developed by Nakayama and Kakinuma [35] to simulate internal wave propagation, is partially rewritten to solve the set of finite difference equations for nonlinear surface waves. **Figure 19** shows the seabed level in the northern bay, where the still water level is described by $z = 0.0$ m. The shorelines are assumed to be vertical walls with perfect wave reflection, while the Sommerfeld radiation condition is applied at the open boundaries inside the sea area. The initial tsunami height η_0 is assumed to be 9.0 m, as described above.

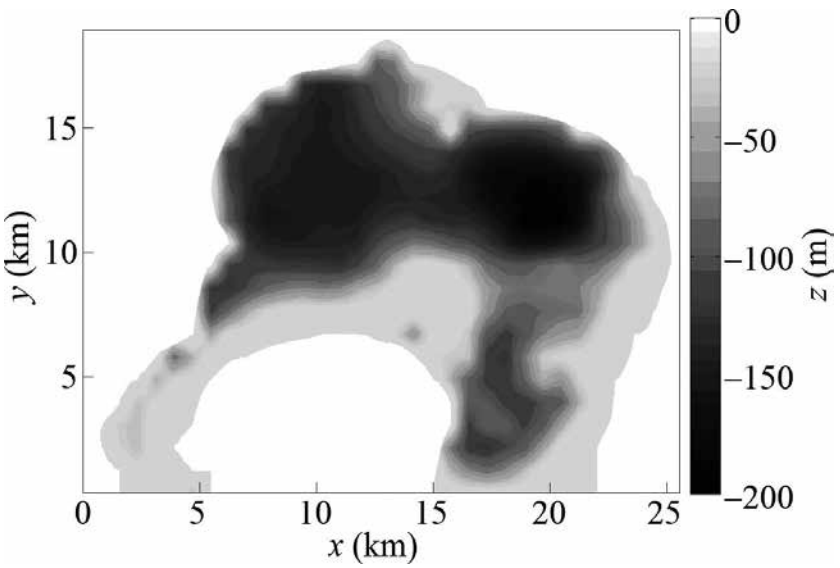

Figure 19. The seabed level in the northern area of Kagoshima Bay, Japan.

3.2.3. Water surface displacements

Water surface displacements are obtained through numerical calculation for the trial cases where the craters are located at Point ① and Point ③, the locations of which are shown in **Figure 20**, as well as for the above-described actual case on September 9, 1780, where the crater is located at Point ②.

There are many submarine fumaroles in Kagoshima Bay, and an active volcano exists in Sakurajima, as shown in **Figure 21**. Sakurajima, where "sakura" means cherry, while "jima", or "shima", means island, in Japanese, was an isolated island prior to its violent eruption in

http://dx.doi.org/10.5772/64530

1914, when Sakurajima was connected to the Ohsumi Peninsula by the eruption with a large amount of ejecta. As shown in **Figure 20**, Point B is located in the West Sakurajima Channel, on the western side of which lies the most urban area in the prefecture, Kagoshima City.

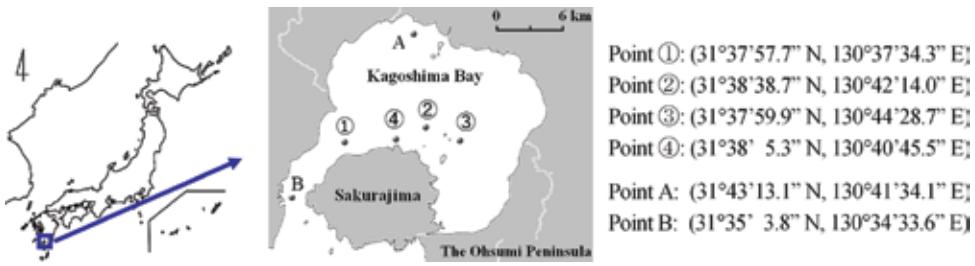

Figure 20. The point locations in Kagoshima Bay, Japan. Sakurajima, which was an isolated island, has an active volcano. Point B is located in the West Sakurajima Channel.

Figure 21. The active volcano with an eruption on Sakurajima, Japan. The author took this photo in 2015.

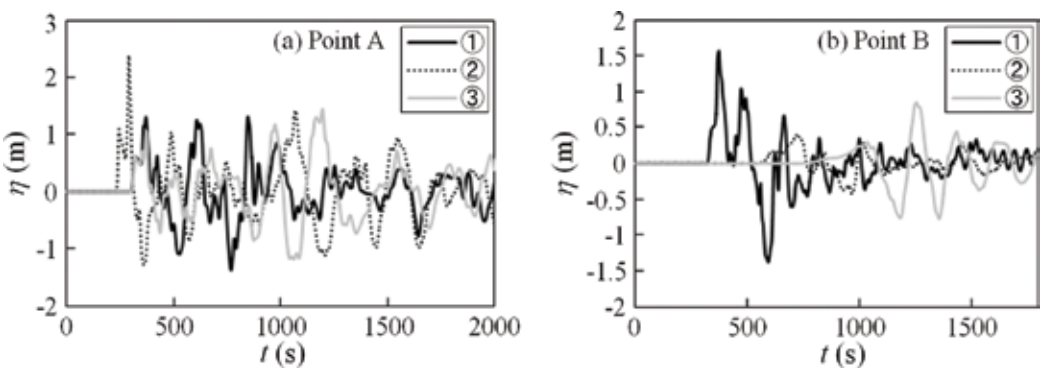

Figure 22. The water surface displacements at Points A and B for different crater locations, i.e., Points ①, ②, and ③. The point locations are indicated in **Figure 20**.

Shown in **Figure 22(a)**, and **22(b)**, are the numerical results for the water surface displacements at Point A, and Point B, indicated in **Figure 20**, respectively. The tsunami height for not only the first wave, but also the several following waves, is larger than 1.0 m at Point A, where it takes a longer time for the oscillation to attenuate because of multiple reflections of tsunamis at the bay head.

Although Point ③ is more distant from Point B than Point ②, the maximum tsunami height at Point B, near the highest population area, is larger in the case where the crater is located at Point ③ than that in the case where the crater appears at Point ②; for in the former case, the wave energy is large for the wave component approaching Sakurajima in a direction oblique, or parallel, to the seashore of Sakurajima, resulting in a tsunami traveling along the shoreline of Sakurajima toward the west.

3.2.4. Distribution of the maximum water level

The numerical results for the distributions of the maximum water level η_{max} for 0.0 s ≤ t ≤ 2.0 × 10^3 s, are shown in **Figure 23(a)–23(d)**, where the crater locations are depicted with white circles off the north of Sakurajima, off Hayato, off Ryugamizu, and off Kurokami-cho, respectively. The still water depth at the crater, h, is assumed to be 1.0 × 10^2 m in all the cases, such that the value of the submarine explosive index concerning tsunami generation, V_w, is about 4.5 × 10^4

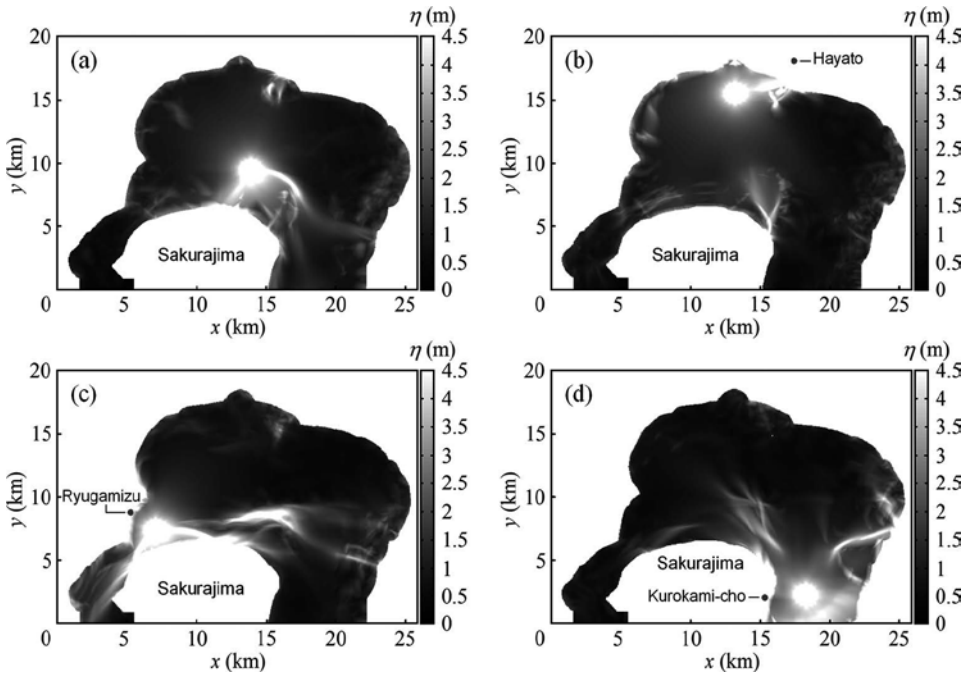

Figure 23. The distributions of the maximum water level for 0.0 s ≤ t ≤ 2.0×10^3 s, for different crater locations. The crater locations depicted with white circles, are as follows: (a) off the north of Sakurajima, (b) off Hayato, (c) off Ryugamizu, and (d) off Kurokami-cho.

(unit length in meter). The tsunamis propagation starts at $t = 0.0$ s. In every case, the maximum water level η_{max} decreases at $(x, y) \approx (20.0 \text{ km}, 14.0 \text{ km})$, for the still water depth is deeper, i.e., about 200 m at the location.

Figure 23 indicates that there are three areas where η_{max} increases, irrespective of the crater location, i.e., near the northern shore of Sakurajima, the bay head off Hayato, and near the western shore of the Ohsumi Peninsula, for the still water depth suddenly decreases toward the land near these three areas.

As shown in **Figure 23(a)**, the tsunamis generated off the north of Sakurajima, travel toward the north, after reflecting at the northern shore of Sakurajima; while as shown in **Figure 23(b)**, the tsunamis generated off Hayato, propagate toward the south, after the reflection at the bay-head shore. In the cases shown in **Figure 23(c)**, and **23(d)**, however, the tsunamis generated off Ryugamizu, and Kurokami-cho, propagate toward the east, and west, respectively, where the maximum wave height of these components is larger.

4. Conclusions

First, several characteristics of tsunami generation due to a landslide, or a sector collapse, were studied, with the tsunamis simulated using the MPS model, that represents their generation through an interaction between the falling bodies, and the seawater, in two vertical dimensions. The falling body was assumed to be a fluid, or a rigid body, which moved down a slope with a constant gradient.

Second, the mechanism of tsunami generation due to a submarine volcanic eruption, was discussed, focusing on a phreatomagmatic explosion. A submarine explosive index concerning tsunami generation, was developed, by assuming the relationship between a phreatomagmatic explosion, and the resultant initial tsunami waveform. A numerical simulation was also generated, for the propagation of tsunamis due to a submarine volcanic eruption, with the specific value for this index, agreeing with the observed data from the submarine explosion leading to a tsunami generated in Kagoshima Bay.

Acknowledgements

Sincere gratitude is extended to Dr. Tsunakiyo Iribe, Ryukyu University, who allowed me to apply his computational program, based on the MPS method, to the numerical calculation for tsunami generation due to a landslide.

I also express my gratitude to Ms. Manami Higashi, Mr. Yusuke Irifune, Mr. Hiroshi Matsumoto, Ms. Aya Oyama, Mr. Roan Riu, Mr. Ryo Sawada, and Dr. Kei Yamashita, who contributed to the numerical simulation, as well as the hydraulic experiments, when they were student members of our laboratory.

Author details

Taro Kakinuma

Address all correspondence to: taro@oce.kagoshima-u.ac.jp

Kagoshima University, Kagoshima, Japan

References

[1] Kakinuma T, Tsujimoto G, Yasuda T, Tamada T: Trace survey of the 2011 Tohoku Tsunami in the north of Miyagi Prefecture and numerical simulation of bidirectional tsunamis in Utatsusaki Peninsula. Coastal Eng. J. 2012; 54: 1250007. 28 p.

[2] Cox D C, Morgan J: Local tsunamis and possible local tsunamis in Hawaii. Hawaii Inst. Geophys. Rep. 1977; HIG-77-14. 118 p.

[3] Kanamori H, Kikuchi M: The 1992 Nicaragua earthquake: a slow tsunami earthquake associated with subducted sediments. Nature. 1993; 361: 714–716.

[4] Goto K, Miyagi K, Kawamata H, Imamura F: Discrimination of boulders deposited by tsunamis and storm waves at Ishigaki Island, Japan. Marine Geol. 2010; 269: 34–45.

[5] Togashi H, Hirayama Y. Hydraulic experiment on reappearance of the Ariake-kai tsunami in 1792. In: Proc. IUGG/IOC Int. Tsunami Symp. (Tsunami '93); 23–27 August 1993; Wakayama. Pp. 741–754.

[6] Marchenko A V, Morozov E G, Muzylev S V: A tsunami wave recorded near a glacier front. Nat. Hazards Earth Syst. Sci. 2012; 12: 415–419.

[7] Wiegel R L: Laboratory studies of gravity waves generated by the movement of a submerged body. Trans. AGU. 1955; 36: 759–774.

[8] Walder J S, Watts P, Sorensen O E, Janssen K: Tsunamis generated by subaerial mass flows. J. Geophys. Res. 2003; 108(B5): 2236. 19 p.

[9] Shigihara Y, Goto D, Imamura F, Kitamura Y, Matsubara T, Takaoka K, Ban K: Hydraulic and numerical study on the generation of a subaqueous landslide-induced tsunami along the coast. Nat. Hazards. 2006; 39: 159–177.

[10] Shigematsu T, Kohno T. An experimental study on fluid motion induced by particles moving on a slope. Annual J. Coastal Eng. JSCE. 2006; 53: 136–140 (in Japanese).

[11] Mohammed F, Fritz H M: Physical modeling of tsunamis generated by three-dimensional deformable granular landslides. J. Geophys. Res. 2012; 117: C11015. 20 p.

[12] Riu R, Kakinuma T, Irifune Y, Nakamura K: An experimental study on tsunami generation due to landslides or glacier collapses. Annual J. Civil Eng. Ocean JSCE. 2010; 26: 207–212 (in Japanese with an English abstract).

[13] Harbitz C B: Model simulations of tsunamis generated by the Storegga Slides. Marine Geol. 1992; 105: 1–21.

[14] Jiang L, Leblond P H: Three-dimensional modeling of tsunami generation due to a submarine mudslide. J. Phys. Oceanogr. 1994; 24: 559–572.

[15] Imamura F, Gica E C: Numerical model for tsunami generation due to subaqueous landslide along a coast: a case of the 1992 Flores tsunami, Indonesia. Sci. Tsunami Hazards. 1996; 14: 13–28.

[16] Rzadkiewicz S A, Mariotti C, Heinrich P: Numerical simulation of submarine landslides and their hydraulic effects. J. Waterway Port Coastal Ocean Eng. 1997; 123: 149–157.

[17] Tinti S, Bortolucci E, Romagnoli C: Modeling a possible holocenic landslide-induced tsunami at Stromboli Volcano, Italy. Phys. Chem. Earth (B). 1999; 24: 423–429.

[18] Grilli S T, Vogelmann S, Watts P: Development of a 3D numerical wave tank for modeling tsunami generation by underwater landslides. Eng. Anal. Bound. Elem. 2002; 26: 301–313.

[19] Panizzo A, Cuomo G, Dalrymple R A. 3D-SPH simulation of landslide generated waves. In: Smith J M, editor. Coastal Eng. 2006. Singapore: World Scientific; 2007. Pp. 1503–1515.

[20] Ataie-Ashtiani B, Shobeyri G: Numerical simulation of landslide impulsive waves by incompressible smoothed particle hydrodynamics. Int. J. Numer. Meth. Fluids. 2008; 56: 209–232.

[21] Gotoh H, Ikari H, Matsubara T, Ito T: Numerical simulation on tsunami due to sector collapse by solid-liquid two-phase flow model based on accurate particle method. J. JSCE, B2 (Coastal Eng.). 2011; 67(2): I_196-I_200 (in Japanese with an English abstract).

[22] Wu T-R, Liu P L-F. A large eddy simulation model for tsunami and runup generated by landslides. In: Liu P L-F, Yeh H, Synolakis C, editors. Advanced Numerical Models for Simulating Tsunami Waves and Runup. Singapore: World Scientific; 2008. Pp. 101–162.

[23] Raichlen F, Synolakis C E. Run-up from three dimensional sliding mass. In: Proc. Long Waves Symp. 2003, XXXth IAHR Congress; 24–29 August 2003; Thessaloniki. Pp. 247–256.

[24] Iribe T, Nakaza E: An improvement of accuracy of the MPS method with a new gradient calculation model. J. JSCE, B2 (Coastal Eng.). 2011; 67(1): 36–48 (in Japanese with an English abstract).

[25] Egorov Y: Tsunami wave generation by the eruption of underwater volcano. Nat. Hazards Earth Syst. Sci. 2007; 7: 65–69.

[26] Maeno F, Imamura F, Taniguchi H: Numerical simulation of tsunamis generated by caldera collapse during the 7.3 ka Kikai eruption, Kyushu, Japan. Earth Planets Space. 2006; 58: 1013–1024.

[27] Taniguchi H: Mechanism of a phreatomagmatic explosion due to the interaction between hot rhyolitic lava flow and external water. Mem. Geol. Soc. Japan. 1996; 46: 149–162 (in Japanese with an English abstract).

[28] Tsuji Y. Volcanic activity and tsunami generation. In: Kaneoka I, Ida Y, editors. Volcanoes and Magma. Tokyo: Univ. of Tokyo Press; 1997. Pp. 197–202 (in Japanese).

[29] Koshizuka S, Oka Y: Moving-particle semi-implicit method for fragmentation of incompressible fluid. Nucl. Sci. Eng. 1996; 123: 421–434.

[30] Fauske H K: On the mechanism of uranium dioxide-sodium explosive interactions. Nucl. Sci. Eng. 1973; 51: 95–101.

[31] Kakinuma T, Akiyama M. Numerical analysis of tsunami generation due to seabed deformation. In: Smith J M, editor. Coastal Eng. 2006. Singapore: World Scientific; 2007. Pp. 1490–1502.

[32] Sato H, Taniguchi H: Relationship between crater size and ejecta volume of recent magmatic and phreato-magmatic eruptions: Implications for energy partitioning. Geophys. Res. Lett. 1997; 24: 205–208.

[33] Newhall C G, Self S: The volcanic explosivity index (VEI): an estimate of explosive magnitude for historical volcanism. J. Geophys. Res. 1982; 87(C2): 1231–1238.

[34] Kakinuma T, Yamashita K, Nakayama K: Surface and internal waves due to a moving load on a very large floating structure. J. Applied Math. 2012; 2012: 830530. 14 p.

[35] Nakayama K, Kakinuma T: Internal waves in a two-layer system using fully nonlinear internal-wave equations. Int. J. Numer. Meth. Fluids. 2010; 62: 574–590.

Section 3

Tsunami Propagation and Early Warning System

Chapter 4

Tsunami Propagation from the Open Sea to the Coast

Hiroshi Kanayama and Hiroshi Dan

Additional information is available at the end of the chapter

http://dx.doi.org/10.5772/63814

Abstract

The tsunami generated by the Great East Japan Earthquake (GEJE) caused serious damage to the coastal areas of the Tohoku district. Numerical simulations are used to predict damage caused by tsunamis. Shallow-water equations are generally used in numerical simulations of tsunami propagation from the open sea to the coast. This research focuses on viscous shallow-water equations and attempts to generate a computational method using finite-element techniques based on the previous investigations of Kanayama and Ohtsuka (1978). First, the viscous shallow-water equation system is derived from the Navier-Stokes equations, based on the assumption of hydrostatic pressure in the direction of gravity. The derived equations have the horizontal viscosity term hereditary from the original Navier-Stokes equations. Next, a numerical finite element scheme is shown. Finally, tsunami simulations of Tohoku-Oki are shown using the above-mentioned approach. Our main concern in this chapter is how to set the boundary condition on the open boundary.

Keywords: Tsunami, the Great East Japan Earthquake (GEJE), Viscous shallow-water equations, Navier-Stokes equations, Finite-element method

1. Introduction

The coastal areas of Tohoku district suffered serious damage from the tsunami caused by the 2011 off the Pacific Coast of Tohoku Earthquake that occurred on March 11, 2011 [1, 2]. Numerical simulations are used to develop disaster-prevention measures to deal with such tsunami disasters. They are also used to predict potential future tsunami disasters, to design disaster-prevention facilities such as coastal breakwaters and levees and to predict tsunami attacks immediately after an earthquake occurs [3, 4]. The Central Disaster Prevention Council [5] prepares a basic disaster prevention plan and participates in the determination of important

disaster-prevention matters. If the Tonankai-Nankai earthquake occurs, it may cause considerable damage. Consequently, the council has been performing numerical calculations to predict wave height and arrival time when tsunami reaches the coast.

In this chapter, to let it be self-contained, the viscous shallow-water equations are again derived from the Navier-Stokes equations in which the hydrostatic pressure in the direction of gravity is assumed. In the numerical analysis of tsunamis, the viscosity term is often omitted or simply added [6, 7]. In this study, however, a computational method that does not omit the viscosity term is adopted, that is, because it enables more rigorous analysis to be performed and we intend to include the viscosity term in future stress analysis of tsunamis. The approximation scheme [8] is given below and simulation results [9] for a Tohoku-Oki model are again presented for self-containing. Our main concern in this chapter is how to set the boundary condition on the open boundary, which is completely changed to a new one.

2. Viscous shallow-water equations

The tsunami generated by the GEJE caused serious damage to the coastal areas of the Tohoku district. Numerical simulations are used to predict damage caused by tsunamis. Shallow-water equations are generally used in numerical simulations of tsunami propagation from the open sea to the coast. This subsection focuses on viscous shallow-water equations and attempts to generate a computational method using finite-element techniques based on the previous investigations of Kanayama and Ohtsuka [8].

In the numerical analysis of tsunami, a viscosity term is often omitted or simply added [6, 7]. In this subsection, however, a computational method that does not omit the viscosity term is adopted, that is, because it enables more rigorous analysis to be performed, and the authors intend to include the viscosity term in future stress analysis of tsunami. Recently, the authors have found an interesting book [10] that deals with sound mathematical topics related to the viscous shallow-water equations.

2.1. Derivation of the viscous shallow-water equations

As shown in **Figure 1**, Kanayama and Dan [9] considered the shallow-water long-wave flow in which the wavelength is sufficiently long relative to the water depth [11]. First, the viscous shallow-water equations are again derived to let this chapter be self-contained. Detailed derivation comes from the study of Kanayama and Ushijima [11]. Orthogonal coordinates [m] are used, where x_1 and x_2 represent directions in the horizontal plane and x_3 represents the vertical direction, and the time [s] is represented by t. Assuming the hydrostatic pressure in the x_3 direction, the following Navier-Stokes equations are used with the external forces, namely the Coriolis forces and the gravity are assumed to act in the x_1 and x_2 directions and the x_3 direction, respectively.

http://dx.doi.org/10.5772/63814

$$\sum_{j=1}^{3} \frac{\partial u_j}{\partial x_j} = 0, \tag{1}$$

$$\frac{\partial u_1}{\partial t} + \sum_{j=1}^{3} u_j \frac{\partial u_1}{\partial x_j} = -\frac{1}{\rho}\frac{\partial p}{\partial x_1} + \frac{1}{\rho}\sum_{j=1}^{3} \frac{\partial \tau_{1j}}{\partial x_j} + f u_2, \tag{2}$$

$$\frac{\partial u_2}{\partial t} + \sum_{j=1}^{3} u_j \frac{\partial u_2}{\partial x_j} = -\frac{1}{\rho}\frac{\partial p}{\partial x_2} + \frac{1}{\rho}\sum_{j=1}^{3} \frac{\partial \tau_{2j}}{\partial x_j} - f u_1, \tag{3}$$

$$0 = -\frac{1}{\rho}\frac{\partial p}{\partial x_3} - g. \tag{4}$$

$u(x_1, x_2, x_3, t)$ represents the fluid velocity component [m/s] in the x_i (i=1–3) direction, $p(x_1, x_2, x_3, t)$ denotes the pressure [N/m^2], ρ is the density [kg/m^3], τ_{ij} is the stress component [N/m^2] in the x_i direction acting on the x_j plane, f is the Coriolis coefficient [1/s], and g is the acceleration [m/s^2] due to the gravity. In addition, the ordinate [m] of the water surface (water level) is represented by ζ and the ordinate [m] of the bottom surface is represented by h. Note that h usually has negative input values depending on x_i (i = 1–2).

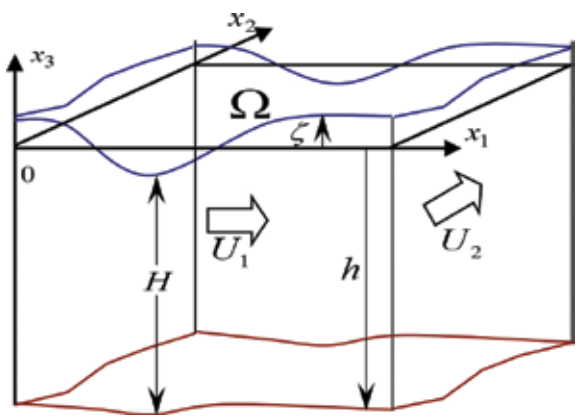

Figure 1. Variables of the computational model [9].

Eqs. (1)–(3) [9] are integrated with respect to x_3 from the bottom h to the water surface ζ. The velocity component in the normal direction is assumed to be zero at the water and bottom surfaces. By doing this, the viscous shallow-water equations expressed by the water level and the averaged velocity can be derived. If the layer thickness is $H(x_1, x_2, t)$ and the average velocity in the x_i (i = 1, 2) direction is U_i (x_1, x_2, t), then H and U_i are given by the following equations:

$$H = \zeta - h,\ U_i = \frac{1}{H}\int_h^\zeta u_i\, dx_3. \tag{5}$$

Note that H is assumed to be positive in this chapter, whose guarantee is a difficult mathematical problem [9].

The fixed density of the layer is represented by ρ and the stress component in the x_i direction acting on the x_j plane is represented by $\tilde{\tau}_{ij}$. The horizontal viscosity constant [Ns/m^2] is represented by μ_H, the wind effect coefficient is represented by θ, the air density is represented by ρ_a, the wind velocity component speed in the x_i direction is represented by W_i, and the Chezy coefficient [m$^{1/2}$/s] is represented by C. Then, the following viscous shallow-water equations are derived [9]:

$$\frac{\partial \zeta}{\partial t} + \sum_{j=1}^{2} \frac{\partial}{\partial x_j}\left(HU_j\right) = 0, \tag{6}$$

$$\begin{aligned} &H\left(\frac{\partial U_i}{\partial t} + \sum_{j=1}^{2} U_j \frac{\partial U_i}{\partial x_j}\right) = -gH\frac{\partial \zeta}{\partial x_i} + \frac{1}{\rho}\sum_{j=1}^{2}\frac{\partial}{\partial x_j}\left(H\tilde{\tau}_{ij}\right) \\ &+\frac{1}{\rho}\theta\rho_a W_i\left(\left(W_1\right)^2 + \left(W_2\right)^2\right)^{\frac{1}{2}} - \frac{g}{C^2}U_i\left(\left(U_1\right)^2 + \left(U_2\right)^2\right)^{\frac{1}{2}} + \left(-1\right)^{i+1} fHU_{i+1}, \end{aligned} \tag{7}$$

where

$$\tilde{\tau}_{ij} = \mu_H\left(\frac{\partial U_i}{\partial x_j} + \frac{\partial U_j}{\partial x_i}\right),\ U_3 = U_1. \tag{8}$$

Note that $\tilde{\tau}_{ij}/2$ is often used for the definition of $\tilde{\tau}_{ij}$. Here, however, we follow the definition in [11] for convenience.

Finite-element approximation is performed for the viscous shallow-water Eqs. (6) and (7) with given initial conditions and boundary conditions.

The computational domain is the two-dimensional (2D) polygonal region Ω surrounded by the boundaries Γ_c and Γ_o. In this region, the orthogonal coordinates $x = (x_1, x_2)$ are used. The boundary conditions on Γ_c and Γ_o and the initial conditions at $t = 0$ are as follows [9]:

Boundary conditions, Eqs. (9) and (10):

$$U_i(x,t) = 0 \text{ on } \Gamma_c \tag{9}$$

http://dx.doi.org/10.5772/63814

$$\left.\begin{array}{l}\zeta(x,t)=\zeta_{\Gamma_o}(x,t)\\ \sum_{j=1}^{2}\tilde{\tau}_{ij}n_j=0\end{array}\right\}\ \text{on } \Gamma_o. \tag{10}$$

Here, n_i is the component in the x_i direction of the unit outward normal vector on the boundary. On Γ_o, $\zeta_{\Gamma_o}(x,t)$ is specified. Later, we improve Eq. (10).

Initial conditions:

$$U_i(x,0)=U_{i0}(x),\ \zeta(x,0)=\zeta_0(x). \tag{11}$$

Here, $U_{i0}(x)$ and $\zeta_0(x)$ are the initial values of U_i and ζ, respectively.

2.2. Finite-element approximations for the viscous shallow-water equations

The finite-element approximation [8] is as follows. First, Eqs. (6) and (7) are multiplied by test functions and then integrated over the computational domain Ω. Subsequently, the approximation is carried out for terms containing a derivative with respect to time by using an explicit method. For terms containing spatial derivatives, the finite-element approximation is carried out by using the piecewise linear basis function $\hat{\phi}_k$. For terms without spatial derivatives, the approximation is carried out by using the corresponding step function $\bar{\phi}_k$. The step function $\bar{\phi}_k$ is 1 in the barycentric region around the node k and is 0 at other places.

$$\left(\frac{\bar{\zeta}^{n+1}-\bar{\zeta}^{n}}{\Delta t},\bar{\phi}_k\right)+\left(\sum_{j=1}^{2}\frac{\partial\left(\hat{H}^n\hat{U}_j^n\right)}{\partial x_j},\hat{\phi}_k\right)=0. \tag{12}$$

$$\begin{aligned}&\left(\bar{H}^{n+1}\left(\frac{\bar{U}_i^{n+1}-\bar{U}_i^{n}}{\Delta t}\right),\bar{\phi}_k\right)+\left(\hat{H}^{n+1}\sum_{j=1}^{2}\hat{U}_j^n\frac{\partial\hat{U}_i^n}{\partial x_j},\hat{\phi}_k\right)\\&=-\left(g\hat{H}^{n+1}\frac{\partial\hat{\zeta}^{n+1}}{\partial x_i},\hat{\phi}_k\right)-\sum_{j=1}^{2}\left(\frac{1}{\rho}\hat{H}^{n+1}\mu_H\left(\frac{\partial\hat{U}_i^n}{\partial x_j}+\frac{\partial\hat{U}_j^n}{\partial x_i}\right),\frac{\partial\hat{\phi}_k}{\partial x_j}\right)\\&+\left(\frac{1}{\rho}\theta\rho_a W_i\left(\left(W_1\right)^2+\left(W_2\right)^2\right)^{\frac{1}{2}},\bar{\phi}_k\right)-\left(\frac{g}{C^2}\bar{U}_i^n\left(\left(\bar{U}_1^n\right)^2+\left(\bar{U}_2^n\right)^2\right)^{\frac{1}{2}},\bar{\phi}_k\right)\\&+\left(\left(-1\right)^{i+1}f\bar{H}^{n+1}\bar{U}_{i+1}^n,\bar{\phi}_k\right).\end{aligned} \tag{13}$$

In the above, ζ_k^{n+1} is determined from Eq. (12). From the obtained value and $U_{i,k}^n$, the value $U_{i,k}^{n+1}$ is determined by Eq. (13). Here, ζ_k^n and $U_{i,k}^n$ are approximate values of $\zeta(x,t)$ and $U(x,t)$ respectively, at the node k after n time steps, and Δt represents the size of time steps. In addition, the following symbols are also used:

$$\left(\frac{\partial U_i}{\partial x_j}, v\right) = \int_\Omega \frac{\partial U_i}{\partial x_j} v\, dx, \tag{14}$$

$$\hat{U}_i^n = \sum_k U_{i,k}^n \hat{\phi}_k, \overline{U}_i^n = \sum_k U_{i,k}^n \overline{\phi}_k. \tag{15}$$

It is well known that integration by parts is used for the viscosity term in (13).

Because of the presence of the basic boundary conditions, Eq. (12) holds for all nodes except for the nodes on Γ_o and Eq. (13) holds for all the nodes except for the nodes on Γ_c. However, on the boundary Γ_o, an approximation method is adopted in which the advective term of Eq. (13) uses Tabata's upwind approximation [9, 12]. A mathematical justification for the approximation scheme for linearized equations related to the above scheme was given by Kanayama and Ushijima [13, 14].

In general, tsunami is excited in the following two ways. The first one is to consider the tsunami excitation as the initial condition of the water surface, for which we do not have sufficient input information in such an artificial tsunami of Hakata Bay [9]. The second one is to consider it as the boundary condition of the water surface as in the next subsection. In the setting of Hakata Bay, a computational domain is not so wide that the above approach may be the only way. It is also noted that 50 [m] at the open boundary for the later Tohoku-Oki case may be too high. In the computation, the tsunami arrived at Oshika Peninsula after 20 min, and the highest wave height reached 15 [m]. These numerical results should be checked more carefully with data on the open boundary.

3. Computational examples

3.1. Tohoku-Oki models

Now, numerical results [9] for a Tohoku-Oki model are again shown for self-containing. When not specifically defined, the same physical values as for Hakata Bay were used. Regarding the mesh data, the total number of nodes is 56,562, the total number of elements is 113,013, and the ocean floor ordinate is set to become deep gradually from $h = -10$ to $h = -1{,}000$ [m]. We set the initial conditions at $\zeta_0(x) = 0$ and $U_{i0}(x) = 0$, and the boundary conditions $\zeta_{\Gamma_o}(x,t) = 50$ [m] ($0 < t < 60$ [s]) at the tsunami-generating area and $\zeta_{\Gamma_o}(x,t) = 0$ [m] at other

http://dx.doi.org/10.5772/63814

areas (see **Figure 2**). It is noted that 50 [m] at Γ_o may be too high. In our computation, the tsunami arrived at Oshika Peninsula in **Figure 2** after 20 min and the highest wave height reached 15 [m]. These numerical results should more carefully be checked with boundary data on Γ_o.

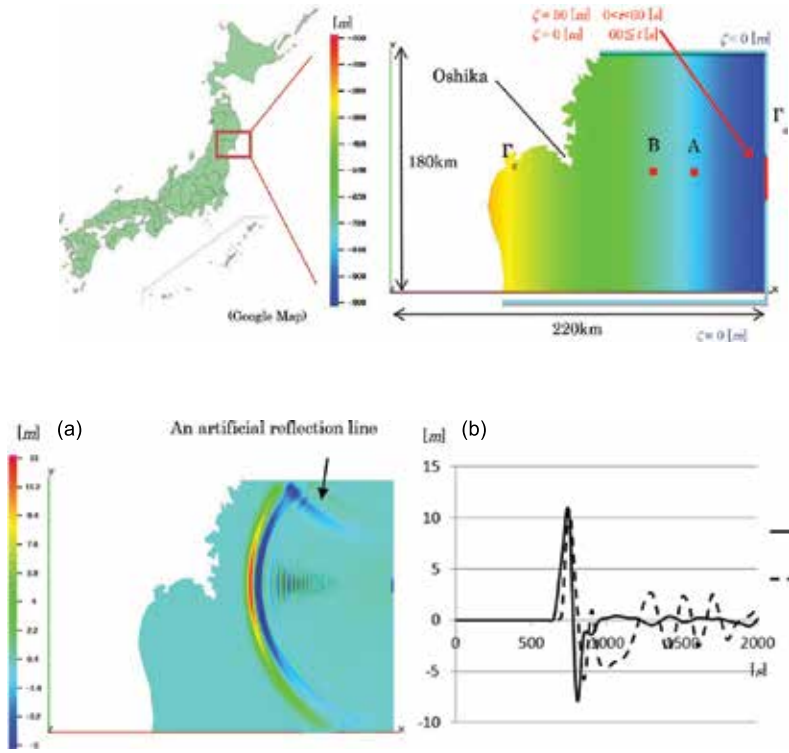

Figure 2. A computational model of Tohoku-Oki [9]. (a) Contour map of ζ [9]. (b) Time histories of ζ [9].

Figure 2a shows the ordinates of the water surface (water level) after 18 [min]. Since the computational domain is not wide, it looks that there is a reflection from the northern boundary in **Figure 2a**. This artificial reflection can be removed by suitable boundary conditions on Γ_o. Details are later mentioned. **Figure 2b** shows the water level change at the two points A and B in **Figure 2**. The wave height at the point B is higher than the point A after about 1500 [s]. When the tsunami reaches coastal areas, the water depth becomes shallow and the wave height becomes high.

Next, new numerical results for the second Tohoku-Oki model are shown. When not specifically defined, the same physical values as for Hakata Bay were used. Regarding the mesh data, the total number of nodes is 563,100, the total number of elements is 1,123,178, and **Figure 3** shows the ocean floor ordinate, which is constructed from 30-arc sec interval grid of JTOPO30, provided by the Marine Information Research Center. We set the initial conditions at $\zeta_0(x)$ like **Figure 4** based on the data of Fujii et al. [15] as a source of tsunami. **Figure 5a–f** shows the

ordinates of the water surface (water level) every 8 [min] from after 8 [min] to after 48 [min]. In our previous paper [9], since the computational domain is not wide, it looks that there is a reflection from the boundary Γ_o (see **Figure 2a**). This artificial reflection can be removed by changing boundary conditions from (10) to (16) as follows:

$$\left.\begin{array}{c} U_n(x,t) = c\dfrac{\sqrt{g|h|}}{H}\zeta(x,t) \\ U_t(x,t) = 0 \end{array}\right\} \ on\ \Gamma_o, \tag{16}$$

where U_n and U_t denote the normal component of velocity and the tangential component of velocity, respectively, and c is a constant. We used (c = 0.9) in this chapter.

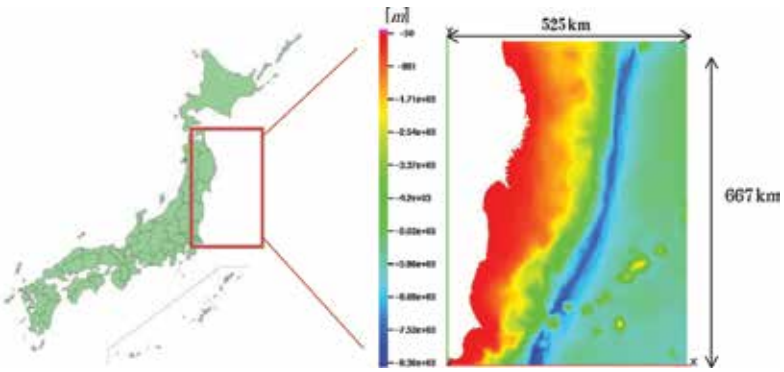

Figure 3. The second computational model of Tohoku-Oki.

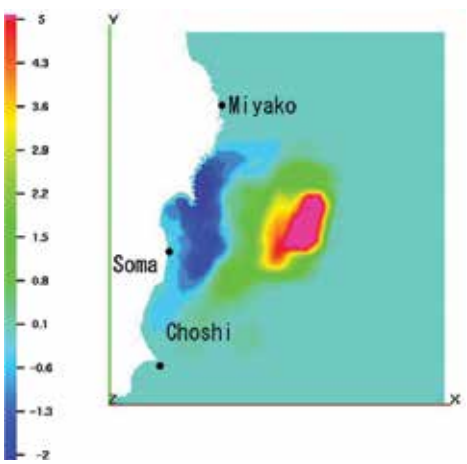

Figure 4. Contour map of initial water level.

http://dx.doi.org/10.5772/63814

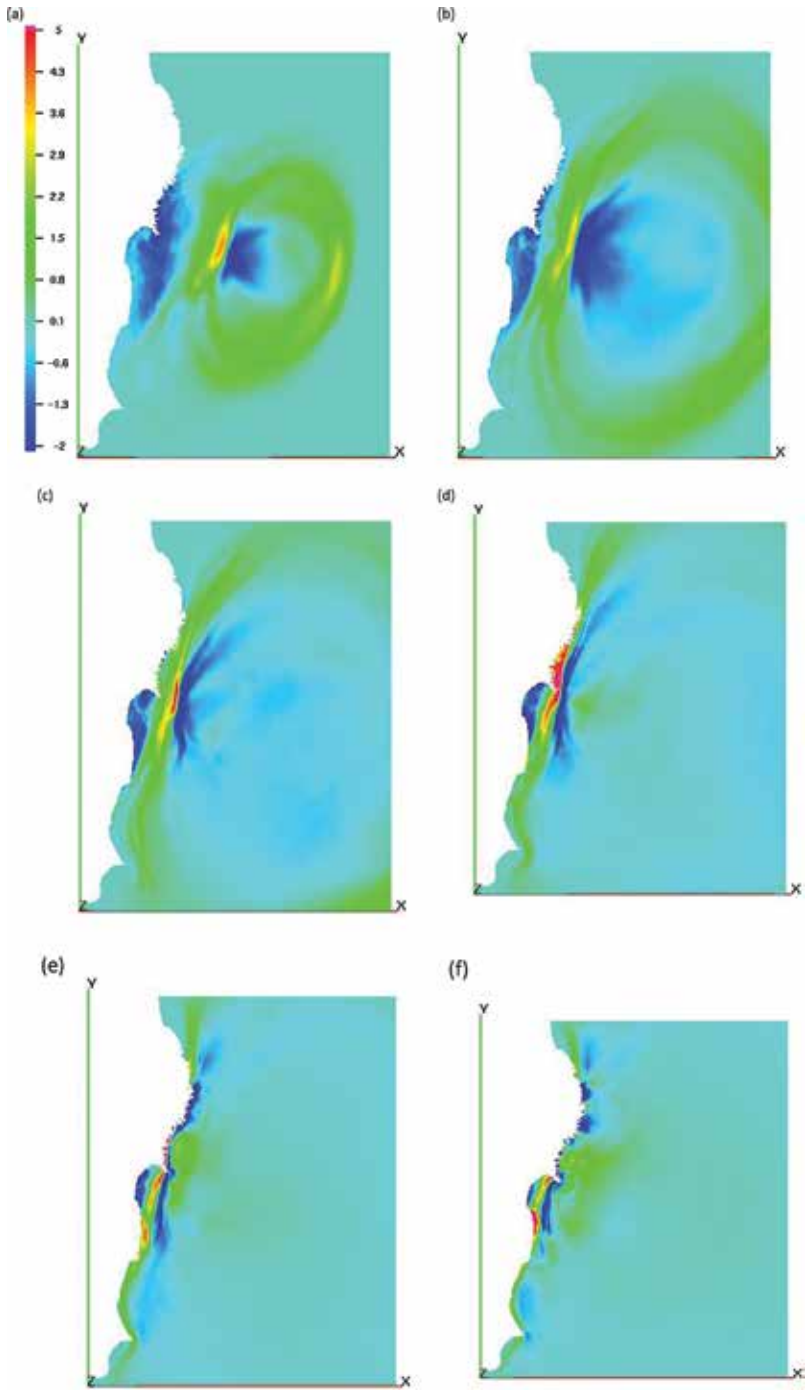

Figure 5. (a) Contour map of after 8 min, (b) contour map of after 16 min, (c) contour map of after 24 min, (d) contour map of after 32 min, (e) contour map of after 40 min, and (f) contour map of after 48 min.

Figure 6 shows the water level change at the three points Miyako, Soma and Choshi in **Figure 4**. Solid curves show observed data [15] and dashed curves show numerical results. Though the arrival time of the first wave is almost same, the wave height is small compared with observed data at the points of Miyako and Soma. Results may be improved by changing initial and boundary conditions.

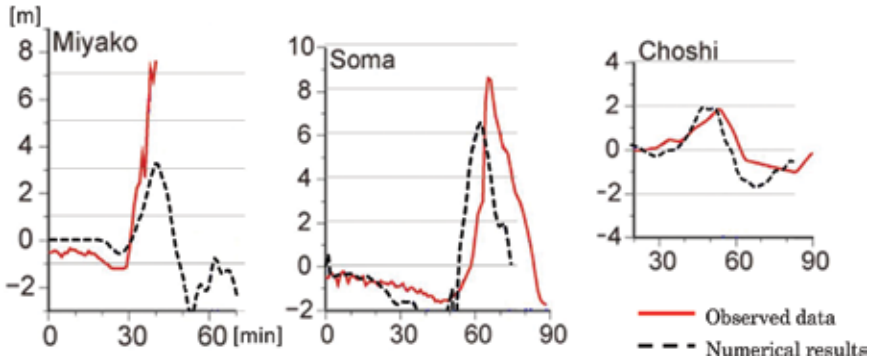

Figure 6. Time histories of ζ.

4. Concluding remarks

In this study, the viscous shallow-water equations have again been derived from the Navier-Stokes equations in which the hydrostatic pressure in the direction of gravity is assumed. Tsunami propagation is then simulated by a finite-element computation. In the study of

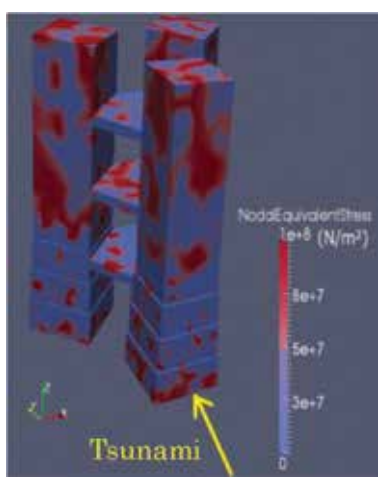

Figure 7. Structural analysis in the case of tsunami attack [9].

Kanayama and Dan [9] using the Hakata Bay model, in which the tsunami-generating area was taken to be the epicenter of the West off Fukuoka Prefecture Earthquake (2005), tsunami propagation from the open sea to the coastal area might be produced. This is an example in which the conventional open boundary condition Eq. (10) is still valid. In this chapter, however, in the second Tohoku-Oki model, the open boundary condition is changed from Eq. (10) to Eq. (16) to overcome artificial reflection. In addition, we have reconstructed a system in which the tsunami arrival time and the wave height at the time of tsunami attack can be obtained from numerical results. Since our analysis takes the viscosity term into account, this study can also be considered to be a preliminary study for future planned stress analyses of tsunamis (see **Figure 7**). We still want to check whether the hydrostatic pressure is always the dominant force in the case of tsunami attack compared with other forces including the viscous force.

Acknowledgements

The first author thanks the JKA RING!RING! Project for the financial support during 2015FY.

Author details

Hiroshi Kanayama[1*] and Hiroshi Dan[2]

*Address all correspondence to: kanayamah@fc.jwu.ac.jp

1 Japan Women's University, Tokyo, Japan

2 Kyushu University, Fukuoka, Japan

References

[1] National Institute for Land and Infrastructure Management, Ministry of Land, Infrastructure, Transport and Tourism, Japan and Building Research Institute, Incorporated Administrative Agency, Japan: Quick report of the field survey and research on the 2011 off the Pacific Coast of Tohoku Earthquake. 2011; Technical Note 636: Building Research Data 132 (in Japanese)

[2] Yoshimura S et al.: Understanding tsunami-causing damage mechanism of machines and structures based on a discipline of mechanics. In: Report of JSME Research Committee on the Great East Japan Earthquake Disaster. 2014. Chapter 4.

[3] Goto C, Sato K: Development of tsunami numerical simulation system for Sanriku coast in Japan. Report of the Port and Harbour Research Institute. 1993;32(2):3–44 (in Japanese)

[4] Takahashi T: Application of numerical simulation to tsunami disaster prevention. Journal of Japan Society of Computational Fluid Dynamics. 2004;12(2):23–32 (in Japanese)

[5] The Central Disaster Prevention Council. Special Investigation Council concerning Tounankai and Nankai Earthquakes (in Japanese) http://www.bousai.go.jp/kaigirep/chuobou/senmon/tounankai_nankaijishin/index_nankai.html [Accessed:03-06-2016]

[6] Ulutas E: The 2011 off the Pacific Coast of Tohoku-Oki Earthquake and tsunami: influence of the source characteristics on the maximum tsunami heights. In: Proceedings of the International Symposium on Engineering Lessons Learned from the 2011 Great East Japan Earthquake. 2012. pp. 602–611.

[7] Imamura F, Yalciner AC, Ozyurt G. Tsunami modelling manual. 2006. http://www.tsunami.civil.tohoku.ac.jp/hokusai3/J/projects/manual-ver-3.1.pdf [Accessed: 27-03-2012]

[8] Kanayama H, Ohtsuka K: Finite element analysis on the tidal current and COD distribution in Mikawa Bay. Coastal Engineering in Japan. 1978;21:157–171.

[9] Kanayama H, Dan H: A tsunami simulation of Hakata Bay using the viscous shallow-water equations. Japan Journal of Industrial and Applied Mathematics. 2013;30(3):605–624.

[10] Bresch D. Shallow-water equations and related topics. In: Dafermos C, Pokorny M, editors. Handbook of Differential Equations: Evolutionary Equations. 5: 2009. pp. 1–104. Elsevier doi:10.1016/S1874-5717(08)00208-9

[11] Kanayama H, Ushijima T: On the viscous shallow-water equations I – derivation and conservation laws. Memoirs of Numerical Mathematics. 1981/1982;8/9:39–64.

[12] Tabata T: A finite element approximation corresponding to the upwind finite differencing. Memoirs of Numerical Mathematics. 1977;4:47–63.

[13] Kanayama H, Ushijima T: On the viscous shallow-water equations II – a linearized system. Bulletin of University of Electro-Communications. 1988;1(2):347–355.

[14] Kanayama H, Ushijima T: On the viscous shallow-water equations III – a finite element scheme. Bulletin of University of Electro-Communications. 1989;2(1):47–62.

[15] Fujii Y, Satake K, Sakai S, Shinohara M, Kanazawa T: Tsunami source of the 2011 off the pacific coast of Tohoku earthquake. Earth Planets Space. 2011;63:815–820.

Chapter 5

Coastal Tsunami Warning with Deployed HF Radar Systems

Belinda Lipa, Donald Barrick and James Isaacson

Additional information is available at the end of the chapter

http://dx.doi.org/10.5772/63960

Abstract

We describe the evolution of coastal HF radar observations of tsunamis, first proposed in 1979 and developed after the 2004 Indonesia and 2011 Japan tsunamis to allow routine monitoring to detect an approaching tsunami. Oceanographic tsunami theory is summarized, both for the fundamental equations of motion and in the ray optics and Green's Law approximations; the latter can be applied when water depths are slowly varying. Observations of the current velocities caused by the 2011 Japan tsunami off the Japanese, the US West, and Chilean coasts are described and examples are shown. These observations led to the development of an empirical tsunami detection method, which is outlined. Examples of offline tsunami detections are given and detection times are compared with arrival times at neighboring tide gauges. We describe the observation and offline detection of the June 2013 meteotsunami off the New Jersey coast using coastal radar systems and tide gauges. Methods to model and simulate tsunami velocities are described and videos of the resulting velocity/height maps are given. We describe preliminary methods for evaluating the suitability of radar sites for tsunami detection using simulated tsunami velocities. Factors affecting tsunami detectability are discussed and methods are described for the alleviation of false alarms.

Keywords: tsunami detection, tsunami velocity/height simulation, remote sensing, radar oceanography

1. Introduction

High-frequency (HF) radars were first used for ocean observations in the 1960s. Located on the coast and transmitting vertically polarized radiations, they exploit the high conductivity of sea

water to propagate their signals well beyond the visible or microwave-radar horizon. They have found widespread use for mapping surface currents and monitoring sea state.

Barrick [1] suggested in 1979 that these radars could detect tsunamis by means of their orbital wave velocity as they approach the coast. Because the distribution of radars around the world was sparse until the 1990s, this concept was not pursued until the tsunami caused by the catastrophic 2004 Banda Aceh earthquake in Indonesia claimed a quarter of a million lives. Although there were no radars in place to observe that event, work began to quantify the radar tsunami response. It was not until the 2011 Tohoku (Japan) tsunami that sufficient radars were in place to capture real tsunami data, which led to development of algorithms to provide robust detection and warning. The Japan tsunami signal was observed by many HF radars around the Pacific Rim with clear results from sites in Japan, USA, and Chile [2–4]. Additional weak tsunamis have also been observed: the 2012 Indonesia tsunami [5] and the 2013 US East Coast meteotsunami [6]. A database of actual HF radar tsunami observations from both strong and weak tsunamis has been accumulated, which has been used to identify the tsunami current velocity signature in the background ocean current velocity field. An empirical method for the automatic detection of a tsunami has been developed, based on pattern recognition in the velocity time series. Over 350 HF radar stations operate from many coastal locations, see, for example, http://www.codar.com/seasonde_world_locations.shtml, providing continuous measurement of surface current velocities and waves. Tsunami detection software can run in a background mode, issuing a warning before the tsunami strikes the coast.

The first possible indication of a tsunami might be the seismic detection of an earthquake. However, not all subsea earthquakes produce tsunamis, and hence the magnitude of an earthquake cannot be used to forecast the detailed generation or intensity of a resulting tsunami. At present, the only operational sensor that detects a tsunami and measures its intensity is a bottom pressure sensor connected to a buoy overhead. Developed by the National Oceanic and Atmospheric Administration (NOAA), networks of these sensors called DART™ (Deep-ocean Assessment and Reporting of Tsunami) were deployed after the 2004 event. They observe the height of the tsunami wave as it passes above them. The tsunami height measured by these buoys is then entered into numerical tsunami models [7–8] to give rough forecasts of the tsunami arrival time and intensity at coastal points around the world. As this network is located in the deep ocean, not all tsunamis are observable by DART and then are not entered into the model before coastal impact. Furthermore, the model's forecast of intensity at the coast is often coarse, so that more accurate estimates of intensity at specific locations are needed; such local variations not captured by the models are referred to as “near field.” HF radars make their areal observations over this local near field and so provide an ideal solution to this need. We describe an empirical tsunami detection algorithm that can run in the background on these radars. This can detect and warn of an approaching tsunami in the near-shore region over which these radars observe the sea surface. A total of 21 offline radar detections of tsunamis have been made to date. Many are described here and others are reported in the literature [2, 3, 5].

A tsunami's orbital velocity appears as part of the surface current as the wave approaches the coast. Tsunami periods lie typically between 20 and 50 min. A tsunami originates when there

http://dx.doi.org/10.5772/63960

is a massive displacement of water: The spatial scales of water displacement are the spatial scales of water displacement are usually of great horizontal but small vertical dimensions These include subsea earthquakes where plates force each other upward/downward, respectively; subsea landslides along steep submerged mountainous slopes; or fast-moving atmospheric anomalies (e.g. low-pressure centers) that create "meteotsunamis." The sources can be thousands of kilometers from an impacted coastal area (where an HF radar might be located), or very close. As the displaced water mass leaves its source region under the influence of gravity, it becomes a freely propagating shallow-water wave. Although the origins of meteotsunamis vis-à-vis seismically generated tsunamis differ, the propagation and evolution of these shallow-water waves are the same, as are the applicable detection and warning methods. Tsunami warning times are mainly dependent on the width of the adjacent continental shelf, ranging from minutes for a narrow shelf (e.g. California) to hours when the shelf is broad (e.g. New Jersey).

Some sites may be less suitable for tsunami monitoring by radar, as the tsunami signature can be masked by large, variable background currents. Tsunami detection is favored by shallow water extending far offshore and by slowly varying background current fields. We describe a method for the evaluation of a coastal site for tsunami warning based on simulated tsunami velocities superimposed on the site's measured velocities. Factors affecting radar detection of tsunamis are discussed. Difficulties that can occur in tsunami detection and methods for alleviation are described. At present, work on the evaluation of coastal sites for tsunami warning using HF radars is being performed in a partnership between Codar Ocean Sensors and NOAA.

It is often convenient to identify Codar SeaSonde® radars by their abbreviated site names used in the field. Those referred to in this article are listed here in alphabetical order, along with their geographical locations:

A087: Usujiri, Hokkaido, Japan

A088: Kinaoshi, Hokkaido, Japan

BELM: Belmar, New Jersey, USA

BML1: Bodega Marine Lab., California, USA

BRMR: Brigantine, New Jersey, USA

BRNT: Brant Beach, New Jersey, USA

COMM: Commonweal, California, USA

ESTR: Point Estero, California, USA

GCVE: Granite Cove, California, USA

LUIS: Point San Luis, California, USA

PREY: Point Reyes, California, USA

SEA1: Seaside, Oregon, USA

STV2: Fort Stevens, Oregon, USA

TRIN: Trinidad, California, USA

YHS2: Yaquina Head South, Oregon, USA

2. Tsunami theory and modeling applicable to HF radar observations

In this section, we provide a brief synopsis of tsunami theory and numerical modeling, as required to explain and develop the HF radar coastal observation/warning capability. We refer to a region of interest near the coast, or within the coverage area of a coastal HF radar, as the "near field," typically of ranges up to 50 km.

2.1. Fundamental equations describing a tsunami in the near-field region

Two equations form the basis of tsunami wave theory and propagation modeling. They are the essence of NOAA's Method of Splitting Tsunami (MOST) over near-field distances but away from the coastal run-up zone where flooding is experienced [7–8]. The first is essentially Newton's second law, that is, force = mass times acceleration, which for fluids gives the Navier-Stokes vector equation to the lowest order. For horizontal coordinates x and y and time t, this is given by:

$$\nabla \eta(x,y,t) = -\frac{1}{g}\frac{\partial \tilde{v}(x,y,t)}{\partial t} \tag{1}$$

where $\eta(x, y, t)$ is the tsunami wave height, g is the acceleration due to gravity, and $\tilde{v}(x,y,t)$ is the orbital velocity of the wave. We assume, as in [7–8], that the orbital velocity at a particular location is independent of depth. The second equation is the continuity equation that expresses the incompressibility of water:

$$\nabla \cdot [(d(x,y) + \eta(x,y,t)\tilde{v}(x,y,t))] = -\frac{\partial \eta(x,y,t)}{\partial t} \tag{2}$$

where $d(x,y)$ is the depth below a mean datum reference, from which the tsunami wave height is measured. The left side of this equation is the net horizontal water volume transport per unit time into a vertical column. Eq. (2) simply expresses the fact that the net flow per unit time into the column of incompressible water must be matched by the rate of rise in the water elevation.

As it stands, Eq. (2) is nonlinear because the two dependent variables, height and velocity, on the left side are multiplied together. Because the tsunami elevation is small compared with the water depth (typically less than 0.5 m in deep water), the height in the left-hand side of the equation can usually be neglected, upon which the equation becomes linear.

http://dx.doi.org/10.5772/63960

2.2. Reduction to partial differential equations (PDEs)

Eqs (1) and (2) represent coupled equations in the unknown tsunami wave height and orbital velocity. By differentiating with respect to time and/or space, as relevant, we eliminate one variable, arriving at the following two hyperbolic PDEs for tsunami height and velocity:

$$\nabla \cdot (d\nabla \eta) - \frac{1}{g}\frac{\partial^2 \eta}{\partial t} \tag{3}$$

$$\nabla\nabla \cdot (d\tilde{v}) - \frac{1}{g}\frac{\partial^2 \tilde{v}}{\partial t^2} = 0 \tag{4}$$

We first solve the scalar Eq. (3) for height. Then orbital velocity is obtained by integrating the left side of the linearized Eq. (2) as a function of time. Radars measure orbital velocity, rather than the tsunami height measured by other tsunami sensors.

These are well-known equations for waves in shallow water. They are justified when water depth is much less than the horizontal scale of the water wave, for example, its wavelength. Horizontal scales of a tsunami wave exceed tens of kilometers, so that even in water several thousand meters deep *the tsunami is always a shallow-water wave everywhere on the planet*. The time scales (periods) for tsunami waves that represent hazards are large, varying from 20 to 50 min.

Another useful quantity applied to shallow-water waves is their phase velocity v_{ph} that is given in terms of the water depth by:

$$v_{ph}(d) = \sqrt{gd} \tag{5}$$

The phase velocity for a tsunami wave train traveling across the ocean with depths from 100 to 1000 m typically exceeds 100 km/h, while the orbital velocities encountered are tens of centimeter/s or less. The water particles themselves move at the orbital velocity, while the surface velocity that the eye would follow as the wave rushes across the ocean is the phase velocity.

We define the "near field" over which the linear model applies as ranging from about 2 km from shore (beyond first radar range cell) out to as far as the radar can see, ~50 km from the coast. The PDEs (3) and (4) are exact under the accepted linearity assumptions and can handle sharp bottom depth changes and reflections or partial absorptions at coastlines. Typically, they are solved with standard finite-element methods [9]. Over near-field distances, they can be solved on personal computers.

2.3. Ray optics and Green's Law approximations for tsunami waves

Traveling waves, such as tsunami or electromagnetic waves, sometimes follow simple ray optics approximations where they can refract, changing their direction continuously with the refractive index. The refractive index for waves of any nature propagating through media with different or changing properties is defined as the ratio of the reference phase velocity to the phase velocity at the specific point in the medium. For light or electromagnetic waves, the reference velocity is taken as the speed of light in vacuum. For acoustic waves or water waves in the shallow-depth limit, one normally selects a convenient reference velocity [10]. So, for example, if one selected the 4000-m depth which is typical of a deep ocean basin, the refractive index becomes $\sqrt{4000/d}$, which is sometimes referred to as the HF asymptotic limit. This approximation applies only when refractive index varies slowly and smoothly with distance. This means that the refractive index cannot have a discontinuous jump, for example, if the bottom had a significant change in depth over scales shorter than a wavelength, say 10 km. Bottom depth fluctuations over smaller scales are not important to tsunami propagation. The tsunami wave, with its massive inertia, is like a low-pass spatial filter that effectively averages across these fine-scale features. A wave typically does not respond appreciably to perturbations with a scale much smaller than its wavelength; this is sometimes known as the Rayleigh criterion. As tsunami wavelengths exceed tens of kilometers, this implies that perturbations with smaller spatial scales (e.g.10 km) are unimportant. There is an often-asked question: "Do I need to use a bathymetry database for tsunami near-field modeling with 1–2 km resolution?" The answer is "No: 10 km resolution is always adequate."

We now examine simplifications possible when depth varies slowly, and discuss exact alternatives that will work when depth varies abruptly.

2.3.1. Ray optics approximation

When depth and refractive index vary slowly, ray tracing allows a version of Fresnel's law such that the advancing wave continuously refracts, so that its direction of propagation follows the gradient of refractive index perpendicular to the isobath depth contours. This approximation has the consequence that there is always only one set of ray paths, which end up perpendicular to the coastline. The coastline boundary will reflect; outgoing rays also cross the contours perpendicularly.

When depth and refractive index vary abruptly, it is valid to use Eqs (1–4) as an alternative. Models based on these equations, for example as described in [7–8], will predict the direction correctly and will generate components parallel to the contours and coastline, as has been observed by radars [2, 5]. Incorrect use of ray tracing for these situations will show evolution with some error of the forward ray toward the region of shallower water near the coast, but can never predict a parallel component.

2.3.2. Green's Law approximation

When refractive index (depth) varies slowly, Green's Law [11, 12] applies. In this limit, tsunami height and orbital velocity follow simple relationships in terms of depth, as described in

http://dx.doi.org/10.5772/63960

reference [1]. It is convenient to normalize the height to a value of the tsunami height in deeper water; we take this depth to be 4000 m, typical for an ocean basin; other depths can be used. The approximate tsunami wave height and scalar tsunami orbital speed in water of depth d are then given by:

$$\eta_{approx} = \eta_{4000}(4000/d)^{1/4} \tag{6}$$

$$v_{approx} = \eta_{4000}\sqrt{g/d}\,(4000/d)^{3/4} \tag{7}$$

where η_{4000} is the tsunami height in water of depth 4000 m.

2.4. Comparison of Green's Law amplitudes with exact calculations

How accurate are the approximations in Eqs (6) and (7) for tsunami height and velocity? To get an idea of this, we compare the height approximation with solutions of the exact Eqs (1–4) for specific cases.

Case 1: A typical continental shelf with a steeply sloping edge that goes from an outer depth of1000 m to an inner depth of 50 m over a horizontal distance of 20 km. Defining the transmission coefficient as the ratio R_T of the tsunami height after passing over this shelf to that before striking the shelf's lower edge, Green's Law Eq. (6) gives $R_T = 2.11$. The solution of the PDEs (2) and (3), discussed further in Section 5, gives $R_T = 1.68$. These values for R_T agree to within about 25%.

Case 2: A vertical shelf edge parallel to the coast falling perpendicularly from depth 50 to 1000 m. Clearly, this fails the "slow depth change vs. tsunami wavelength" criterion required for both ray optics and Green's Law and thus is beyond the scope of these approximate models. For normal incidence to a vertical escarpment, NOAA modelers [8] express Eqs (1–4) as a boundary-value problem requiring continuity of height and transport across the escarpment and obtain the following exact expression for the transmission coefficient of the tsunami wave height:

$$R_T = 2/(1+\sqrt{D_2/D_1}) \tag{8}$$

where D_1 and D_2 are the depths on the shelf's outer and inner edges, respectively. This is considered an exact solution for this defined geometry. Substituting $D_1 = 1000$ m and $D_2 = 50$ m yields a value for R_T equal to 1.63, which is close to the prior estimate from the PDE calculation.

To conclude, the exact solutions for transmission coefficient R_T for a depth change from 1000 to 50 m are (a) 1.68 over a steep slope and (b) 1.63 over a vertical step. These values differ by only about 3%, indicating that shelf slope does not have a significant effect on the transmission coefficient. Comparing these values with the Green's Law approximation of 2.11 suggests an

error estimate of about 25% when using Green's Law for estimating tsunami height change due to sharp depth changes.

2.5. Tsunami arrival time

Solving Eqs (2–3) provides both the tsunami height and orbital velocity profiles as the wave approaches the coast, as impacted by the decreasing depth on the journey toward shore. This yields the most accurate estimate for the arrival time from any offshore point along its path and is useful in near field of the coastal radar because the computational effort is manageable.

However, for an approach from much farther out, or in order to get a quick, rough estimate of the tsunami arrival time, the phase velocity $v_{ph}(d)$ at depth d, time t, and distance s along a tsunami great-circle ray path can be expressed as follows:

$$v_{ph}(d) = \frac{\partial s}{\partial t} \tag{9}$$

Eqs (5) and (9) lead to the following approximate solution for the elapsed time ΔT for the tsunami arrival at distance S from the start:

$$\Delta T = \int_s^0 \frac{\partial s}{\sqrt{g d(s)}} \tag{10}$$

Because of inherent smoothing of the integration process, the depth profile need not be defined to great resolution, allowing quick use of Eq. (10) over large ocean distances to give rough estimates of the tsunami arrival time.

3. HF radar observations of the 2011 Japan tsunami leading to an empirical detection algorithm

Radar echoes are produced by reflection of the radar wave from ocean waves with wavelengths half that of the radar; such waves have periods between 1.5 and 4.5 s. In contrast, the tsunami wave period lies between 20 and 50 min, corresponding to wavelengths between 400 and 800 km in the open ocean. Tsunami orbital velocities add to the shortwave radial velocities producing the radar echo; in deep water, tsunami velocities are too small to be seen by the radar, but they increase as the tsunami moves onto the continental shelf and the water depth decreases below 200 m and can then be observed by radars located on the coast.

Radial current velocities are obtained from the first-order radar echo spectra measured at individual radar sites [13, 14]. In usual practice, several radar echo spectra are averaged over time before analysis. As time resolution is critical for local tsunami detection, unaveraged spectra are analyzed. The Doppler shift from the ideal Bragg frequency defines the radial

http://dx.doi.org/10.5772/63960

current speed; spectral values at that frequency are interpreted to give the azimuth angles at which this speed occurs. Together with range defined by the time delay, estimates follow for the radial current velocity at locations spaced 1° apart around a circular range cell centered on the radar site.

Total current velocities are obtained by combining radial velocities from the radar sites [13]. A grid is formed over the radar coverage area and averaging circles form surrounding each grid point. Total velocity vector components are calculated by fitting to radial velocities from the different radar sites that fall within the averaging circle.

On March 11, 14:46 2011 Japan Standard Time (JST), a magnitude-9 earthquake off Sendai, Japan, unleashed a large tsunami that was observed by HF radars around the Pacific Rim, see **Figure 1**. The earthquake and resulting tsunami are known as the Tohoku event. As our first example, we show current velocities measured by two SeaSonde radars located near Usujiri and Kinaoshi, Hokkaido, Japan during the 2011 Tohoku tsunami.

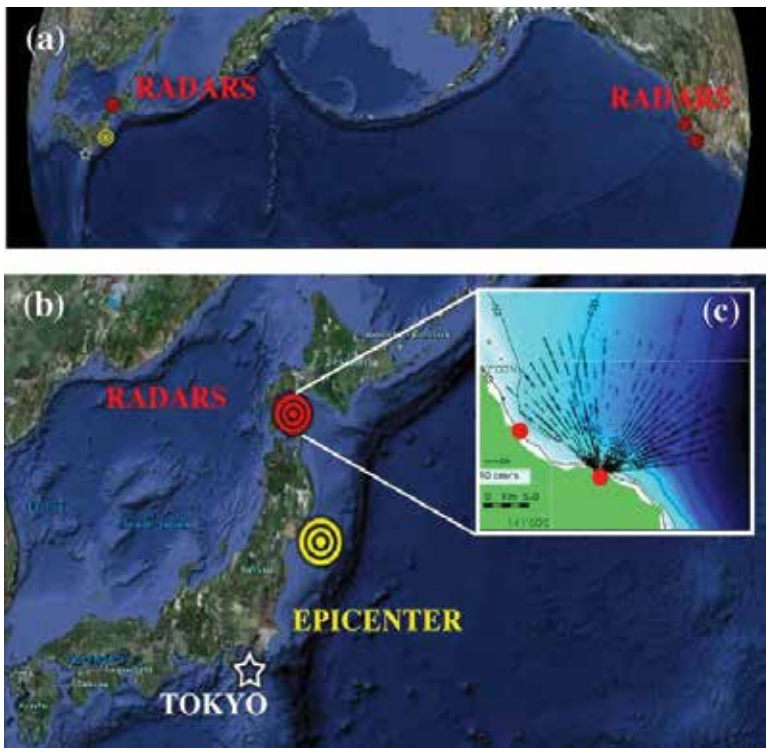

Figure 1. (a) The North Pacific Ocean showing the location of the radars that detected the tsunami. Abbreviated radar field names are as follows; corresponding geographic locations are given in Section 1. Japan: A087 and A088. USA: STV2, SEA1, YHS2, TRIN, GCVE, BML1, PREY, COMM, ESTR, and LUIS. (b) The location of the Japan earthquake and the radars in Hokkaido. (c) The bathymetry offshore from the radars and radial velocities measured by the Kinaoshi radar, March 11, 2011, 21:00 JST.

The radars had a transmit frequency of 42 MHz and a range increment of 0.5 km. The water depth over the entire radar coverage area is less than 200 m. The 42 MHz frequency band is used for high-resolution, short-range current observations and results in a radar range less than 15 km, due to significant attenuation of the surface wave passing across the sea at these higher HF frequencies.

3.1. Total velocity current maps

The direction and strength of the flow were measured at approximate 4-min intervals with a cell resolution of 0.5 km × 0.5 km. **Figure 2** shows total current-velocity maps, the first

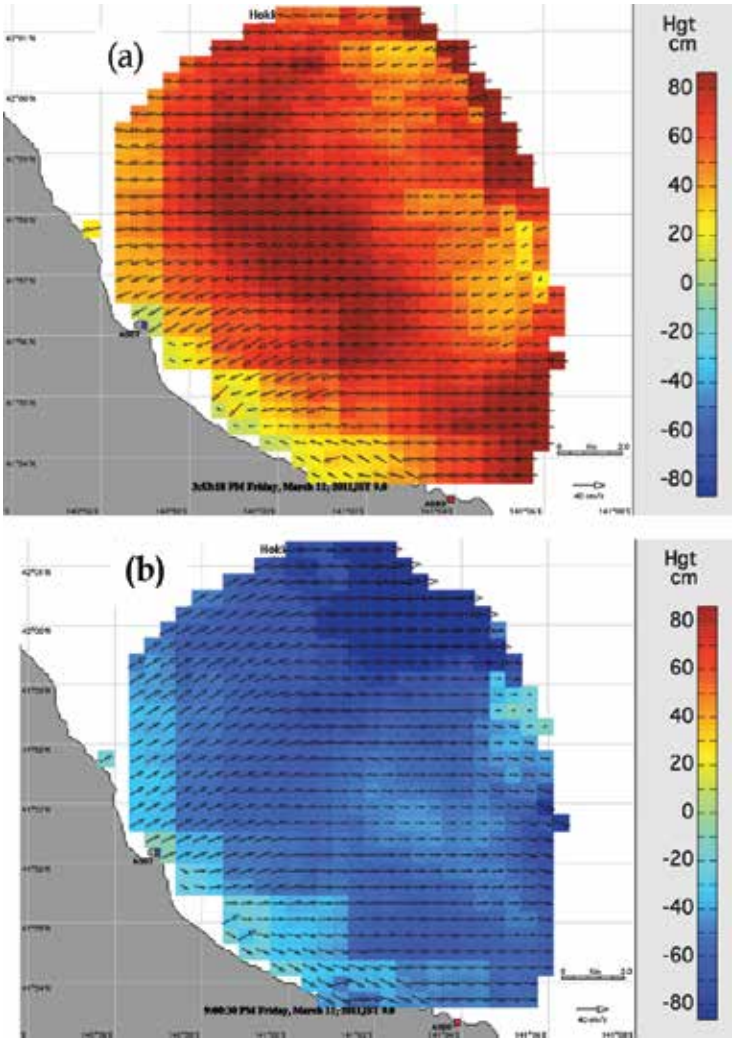

Figure 2. Tsunami current velocity vectors with the tsunami height shown in colors. Radar measurements from A087 (blue circle) and A088 (red circle) made on March 11, 2011 (a) the tsunami arrival at 15:53 JST and (b) outward flow occurring later at 21:00 JST.

http://dx.doi.org/10.5772/63960

demonstrating the arrival of the tsunami, indicated by strong inward flow, the second an example of outward flow. Eqs (6) and (7) relate the tsunami height to the current velocity; heights are displayed in colors superimposed on the velocity vectors shown by the arrows. As noted in Section 2.3.2, the accuracy of Green's Law estimates of height decreases close to shore.

A video showing the current velocity/height flow from March 11, 14:06 JST to March 12, 13:54 JST is shown in Video 1, available at http://bit.ly/29lOdXw

Time in JST is given in each frame of the movie. The video shows the tsunami arriving at 15:53 JST and then sweeping in and out of Uchiura Bay.

3.2. Radial velocity components

As would be expected, the tsunami signal is also visible in the radar returns from a single radar site [3]. To simplify the analysis of the data with the aim of developing objective detection criteria, we group the radial velocities into rectangular area bands 2-km wide approximately parallel to the depth contours. The radial velocities are resolved into components perpendicular and parallel to the area bands. These components are averaged over the band; the averages are termed "band velocities." A time series of the band velocities is then formed, which displays the characteristic oscillations produced by the tsunami.

Figure 3 gives an example of measured radial vectors with a 4-min time resolution and the 2-km wide bands used in the analysis.

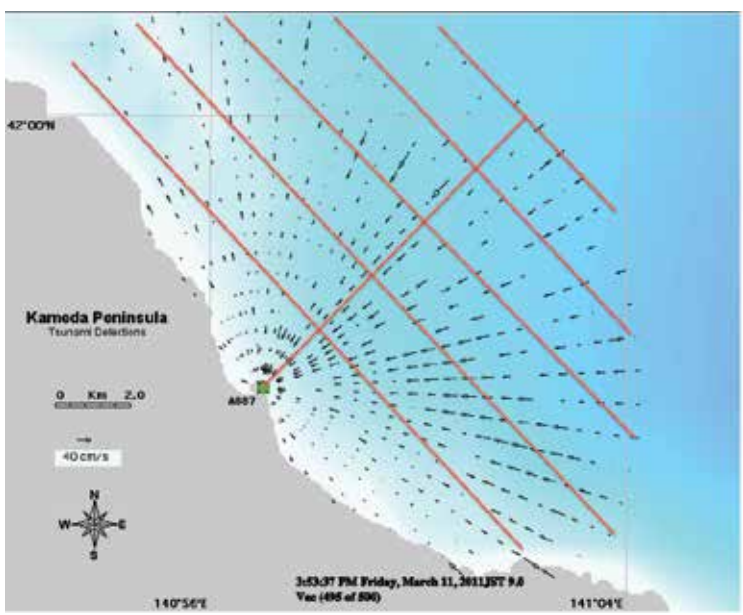

Figure 3. Radial current velocities from the Usujiri, Hokkaido radar (A087) and the area bands used in the analysis which are 2-km wide and approximately parallel to the depth contours.

Figure 4 shows band velocities observed at Kinaoshi, Hokkaido (A088), for three 2-km bands ranging from 6 to 12 km from the shore.

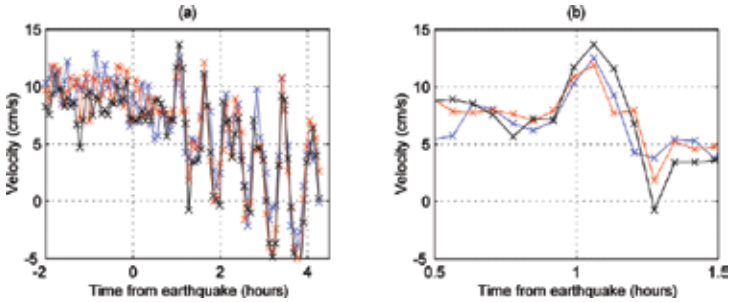

Figure 4. Band velocities from Radar A088. Distance from radar: 6–8 km (blue), 8–10 km (red), and 10–12 km (black). Time span: March 11, 2011 (a) surrounding the tsunami arrival, from 12:46 to 19:46 JST and (b) close to the tsunami arrival, from 14:16 to 15:16 JST.

The arrival of the tsunami is indicated by the commencement of distinctive oscillations in velocity with a period of about 40 min, which are strongly correlated over range.

Further examples of band velocities from radars on both sides of the Pacific close to the tsunami arrival time are shown in **Figure 5**.

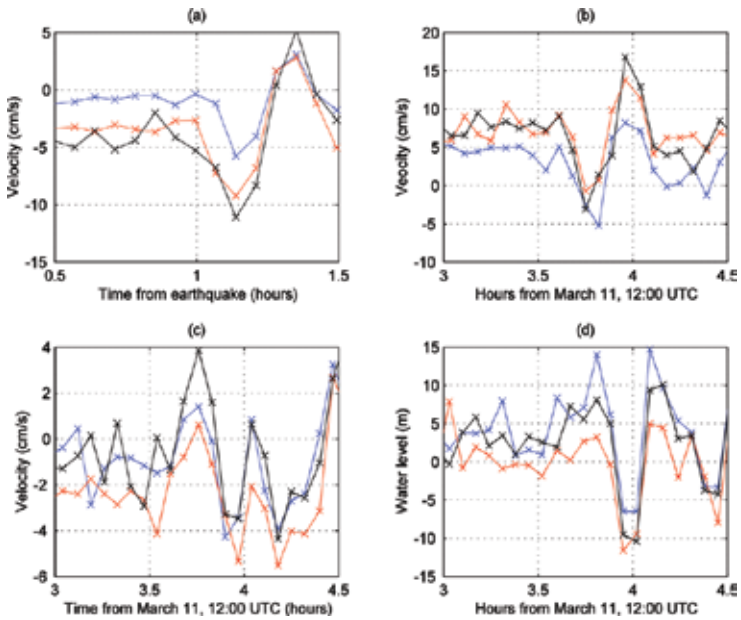

Figure 5. Time series of band velocities showing the typical appearance around the tsunami arrival time for three adjacent 2-km area bands. (a) A087 (Hokkaido, Japan), (b) YHS2 (Oregon, USA), (c) BML1 (California, USA), and (d) PREY (California, USA).

http://dx.doi.org/10.5772/63960

3.3. Detection of the tsunami signal in HF radar data

Two effects distinguish tsunami velocities from the background in **Figures 4** and **5**: (a) velocities in neighboring bands are strongly correlated after the arrival of the tsunami and (b) the velocity oscillations are clearly visible above the background. These effects appear to be characteristic of tsunami band velocities, as they occur in all the radar data from Japan and the US West Coast that we have analyzed. They form the basis of a simple pattern detection procedure. At a given time, a factor (which we call the q-factor) is defined which signals the tsunami arrival when it exceeds a preset threshold. The steps in the detection algorithm are as follows:

- **Step 1:** Within each band, check whether the velocity increases or decreases by an amount greater than a preset level over two consecutive time intervals. If it does, increase/decrease the q-factor level for that band.
- **Step 2:** Do the maximum/minimum velocities for consecutive bands coincide (within a preset value) for consecutive time intervals? If so, increase/decrease the q-factor level further for that band and time.
- **Step 3:** Finally, check whether the velocity increases/decreases over two consecutive time intervals for three adjacent area bands. If so, increase/decrease the q-factor level further for that band/time.

Details of the detection algorithm are given [6].

Positive q-factor values indicate the tsunami velocity at the wave peak is moving toward the radar, negative values indicate that it is moving away.

To set the operational threshold signaling a tsunami detection, an extended data set obtained under normal conditions is analyzed to produce q-factors. A threshold value is then selected. There is a trade-off in the threshold selection: if the q-factor limit is set too low, the peak will certainly indicate a detection, but there may be many false-alarm detections. If the threshold is set too high, there will be few false alarms, but then the tsunami arrival may not be detected.

The tsunami signal can be evident for some time after arrival; however, our detection method is optimized to apply to the first arrival.

3.4. Radar detection of the 2011 Japan tsunami

The Japan tsunami arrival was detected offline at radar sites around the northern Pacific Rim [3]. We here give examples of q-factor tsunami detections and compare arrival times at the radars with those measured by neighboring tide gauges.

3.4.1. Hokkaido, Japan

Figure 6 shows the locations of two radars on the Kameda Peninsula, the neighboring tide gauge, and the offshore bathymetry. The water depth is less than 200 m over the radar coverage area; we found that the tsunami signal is visible in the current velocities out to the radar range limits.

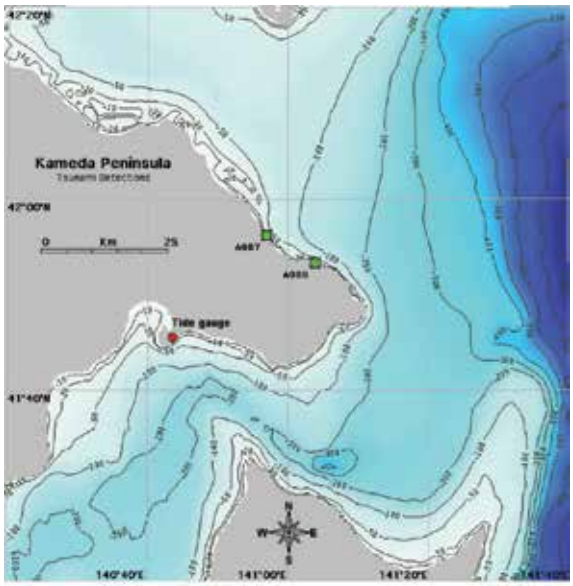

Figure 6. The location of the radars A087, A088, the tide gauge at Hakodate, and the offshore bathymetry.

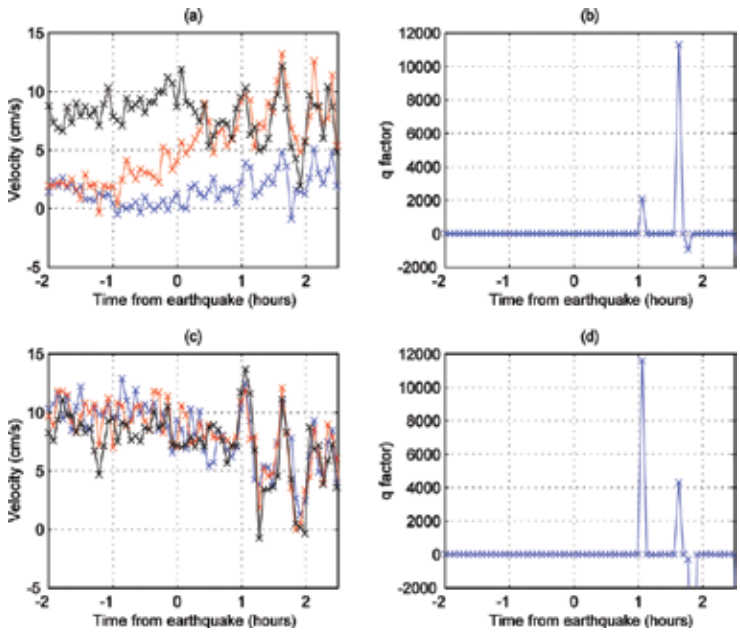

Figure 7. Perpendicular band velocities from A088 and derived *q*-factors. (a) Distance from radar: 0–2 km (blue), 2–4 km (red), and 4–6 km (black). (b) The *q*-factor for range 0–6 km. (c) Distance from radar: 6–8 km (blue), 8–10 km (red), and 10–12 km (black). (d) The *q*-factor for range 6–12 km.

Figure 7 shows A088 band velocities obtained over a 5-h period and the q-factors resulting from application of the analysis described in Section 3.3. About an hour after the earthquake, the tsunami arrived at A088, resulting in distinctive correlated oscillations in the perpendicular band velocities, which lead to a q-factor peak that indicates the tsunami arrival.

Close to shore, part of the tsunami flow is diverted by the steep bathymetry to move parallel to the coast, resulting in a reduced signal in the perpendicular component plotted in **Figure 7**. As discussed in Section 2, this effect can be shown by exact PDE modeling.

The analysis procedure was applied to A087 and A088 for all permutations of three band velocities that contained the tsunami signal, and the resulting q-factors were summed. The q-factor threshold was defined to be 500: the first q-factor to exceed this value was taken as defining the tsunami arrival time. The arrival time at the tide gauge was defined as first tsunami peak in the water-level reading. Radar and tide gauge arrival times are shown in **Table 1**.

Japan March 11, 2011 JST				
Radar (XMTR Freq)	***Arrival time (JST)***	***Ground instrument***	***Arrival time (JST)***	***Water-level change***
A088 (42 Mhz)	15:49	Hakodate tide gauge	16:32	2.0 m
A087 (42 Mhz)	15:54	Hakodate tide gauge	16:32	2.0 m

Table 1. Tsunami arrival times at the Hokkaido radars and the closest tide gauge.

Table 1 shows that the arrival times obtained from the radar q-factors reported are in the correct order: the tsunami arrives at Station A087 further from the earthquake location approximately 5 min after it reaches A088. Arrival times measured by the radars preceded those at the neighboring tide gauge by an average of 40 min, due both to the "quadrature relation" between velocity and height (discussed later in Section 4.1) and the tsunami propagation delay between the two observations.

3.4.2. West Coast of USA

Radar spectra measured by 10 radars located along the US West Coast were analyzed to give band velocities and q-factors. Arrival times were compared with those at local tide gauges. **Figure 8** shows radar and tide gauge locations and the offshore bathymetry. As the adjoining continental shelf is narrow off California and Oregon, the tsunami is often detectable only for close-in ranges.

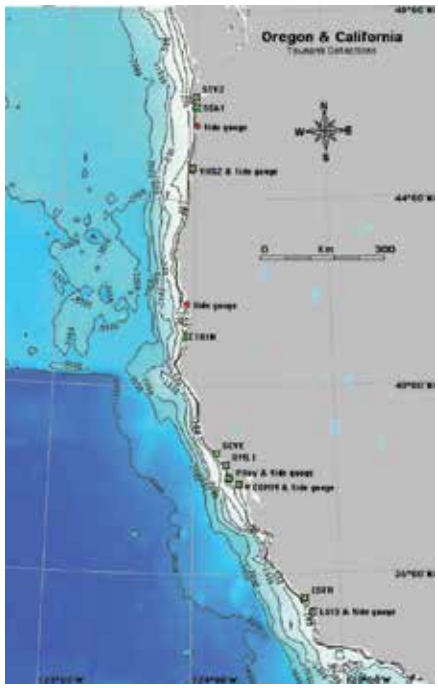

Figure 8. Locations of radars and tide gauges in California and Oregon. The offshore bathymetry indicates a narrow offshore continental shelf.

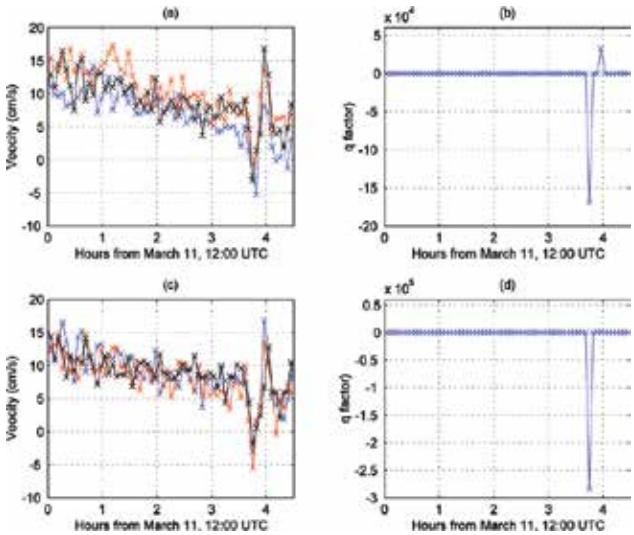

Figure 9. Perpendicular band velocities and derived q-factors from YHS2. (a) Distance from radar: 2–4 km (blue), 4–6 km (red), and 6–8 km (black). (b) The q-factor for range 2–8 km. (c) Distance from radar: 8–10 km (blue), 10–12 km (red), and 12–14 km (black). (d) The q-factor for range 8–14 km.

http://dx.doi.org/10.5772/63960

We illustrate the tsunami detections with two examples of measured band velocities and derived q-factors.

Our first example is the tsunami detection by the radar at YHS2, Oregon (transmit frequency 12 MHz).

Figure 9 shows the band velocities and corresponding q-factors.

The correlation is evident between the velocities in different bands starting at about 3:45 pm Coordinated Universal Time (UTC), resulting in a sharp decrease in the q-factor, which indicates the tsunami moving offshore, resulting in a decrease in water level. The neighboring South Beach tide gauge observed an initial water level increase due to the tsunami of just 0.3 m, which was inadequate to produce a radar detection. However, we note that in **Figure 9(a–c)** the band velocities show the typical correlation due to the tsunami just before the sharp decrease.

Our second example is the tsunami detection by the radar at ESTR in Southern California (transmit frequency 13 MHz). **Figure 10** shows the band velocities and q-factors for ESTR.

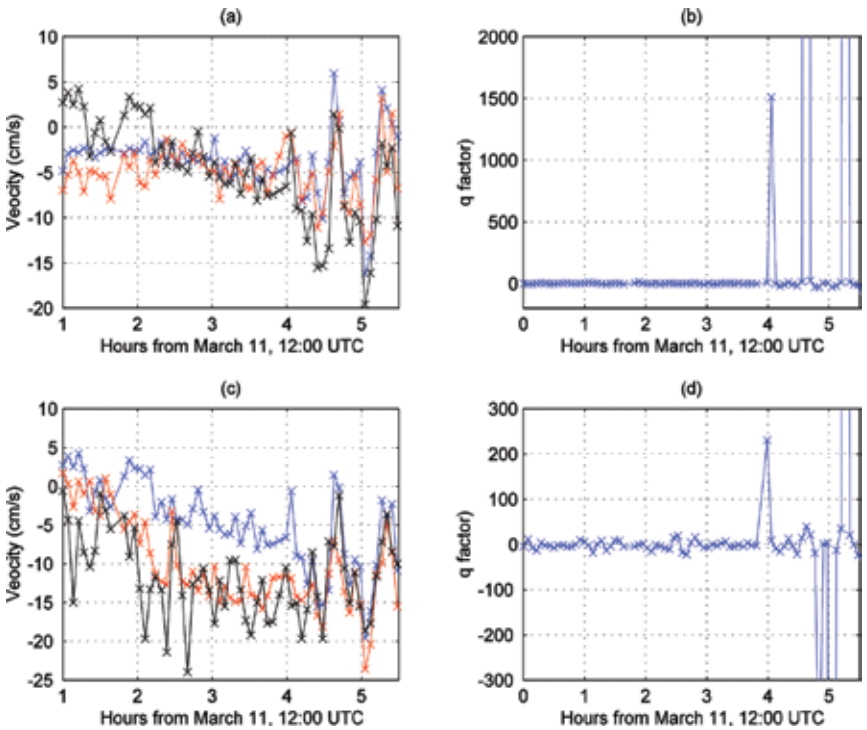

Figure 10. Perpendicular band velocities and derived q-factors from Radar ESTR. (a) Distance from radar: 2–4 km (blue), 4–6 km (red), and 6–8 km (black). (b) The q-factor for range 2–8 km. (c) Distance from radar: 8–10 km (blue), 10–12 km (red), and 12–14 km (black). (d) The q-factor for range 8–14 km.

The observed background current velocities are quite variable for this site: it is the correlations between velocities in different bands that allow the tsunami to be detected by the pattern-recognition algorithm described in Section 3.3.

The Japan tsunami took approximately 10 h to reach the US West Coast; it moved down the coast from north to south. Tsunami and tide gauge arrival times are compared in **Table 2**. Radar stations are listed in the order of the expected arrival of the tsunami.

US West Coast March 11, 2011 UTC				
Radar (XMTR Freq)	***Arrival time (UTC)***	***Tide gauge***	***Arrival time (UTC)***	***Water-level change***
STV2 (12 MHz)	15:32	Garibaldi	15:48	1.2 m
SEA1 (12 MHz)	15:47	Garibaldi	15:48	1.2 m
YHS2 (12 MHz)	15:45	South Beach	15:54	0.3 m
TRIN (5 MHz)	15:34	Crescent City	15:48	0.5 m
GCVE (14 MHz)	15:44	Pt. Reyes	16:00	0.5 m
BML1 (12 MHz)	15:46	Pt. Reyes	16:00	0.5 m
PREY (13 MHz)	15:49	Pt. Reyes	16:00	0.5 m
COMM (13 MHz)	15:56	Fort Point	16:30	0.4 m
ESTR (13 MHz)	16:04	Port San Luis	16:24	2.0 m
LUIS (13 MHz)	16:05	Port San Luis	16:24	2.0 m

Table 2. Comparison of tsunami arrival times from radars and neighboring tide/wave gauges.

Table 2 shows that listed arrival times obtained from the radar q-factors reported are normally in the correct order; thus, it arrives in Southern California after it gets to Northern California and Oregon. Arrival times measured by the radars preceded those at neighboring tide gauges by an average of 15 min, due to both the "quadrature relation" between velocity and height (discussed in Section 4.1) and the tsunami propagation delay between the two observations. We expect to be able to quantify the propagation delay using simulated tsunami velocity patterns derived from the analytical model, as discussed later in Section 5.1.

We note from **Table 2** that the tsunami was detected even though water-level changes at neighboring tide gauges were not large, varying between 0.3 and 2 m.

3.4.3. Chile

A WERA radar system operating at 22 MHz at a site near Concepcion, Chile, observed the Japan tsunami [4]. Current components pointing toward/away from the radar were measured within beams formed by the receiving antenna array. The orbital velocity of the shallow-water tsunami wave is therefore part of the total signal, which also includes other background contributions such as tides and geostrophic flow. **Figure 11** shows radial components of the

http://dx.doi.org/10.5772/63960

surface current velocity plotted as a function of range and time, and wave-level readings from a tide gauge located at Lebu, Chile, about 50 km from the radar.

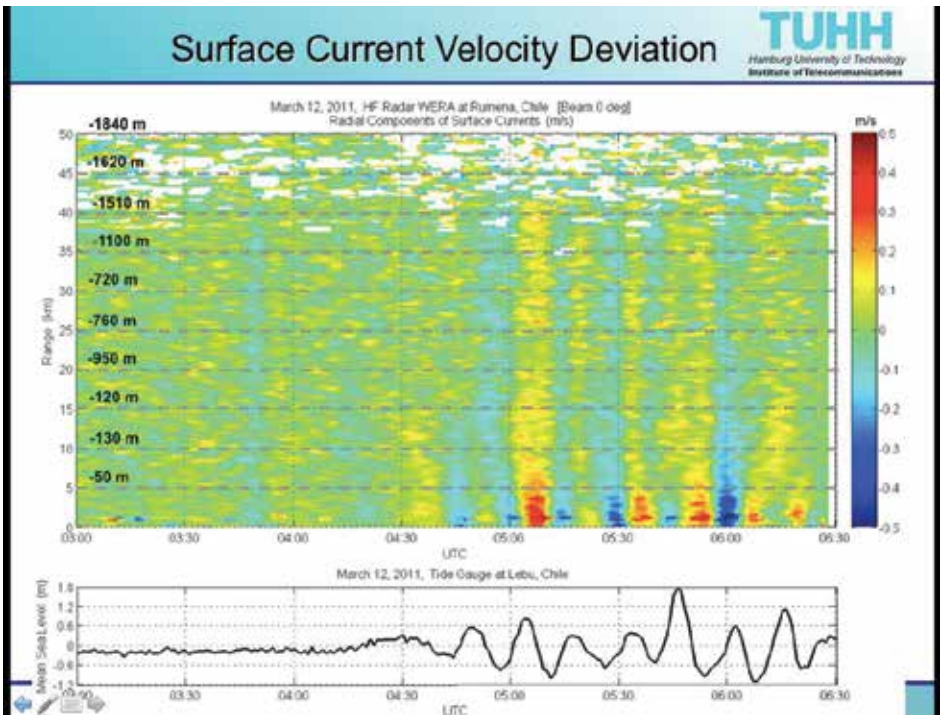

Figure 11. Reproduced with permission from Ref. [4]. Top: radial velocity in m/s of surface currents measured by the HF radar in Chile. Bottom: mean sea level measured by the tide gauge at Lebu, Chile, during the tsunami traveling near the Chilean coast.

Figure 11 shows clear periodic disturbances produced by the tsunami in both radar and tide gauge observations. Obvious correlations in tsunami signatures can be seen for both measurements.

Dashed lines in **Figure 11** give the depths within the main radar beam pointed offshore. The depth contours define a short continental shelf, followed by a steep slope. From a depth of about 50 m at 5 km, the depth drops to 1000 m at a distance of 34 km, that is, a steeply sloping region within a ~29-km span. From there, the depth decreases slowly with distance beyond the shelf/slope region.

The tsunami component of these currents is identified from their typical periods that lie between 20 and 45 min, arriving at about 05:07 UTC on March 12, approximately 22 h after the Japan earthquake. This arrival time was confirmed by NOAA's tsunami model and the tide gauge data.

These observations have unexpected features as follows: (a) the tsunami peaks/troughs are seen out to 40-km range at approximately the same time regardless of distance from the shore

and (b) beyond the shelf, where depths change slowly, from 760 m at 25 km to 1510 m at 40 km, the Green's Law approximation described in Section 2.3.2 should be valid. However, the observed velocity is nearly constant, which contradicts Eq. (7). These effects may be due to signal aliasing, as discussed later in Section 7.

4. Radar observations of the 2013 US East Coast meteotsunami

An unusual storm system moved eastward across the US on June 13, 2013, commonly called a "derecho," and appears to have launched a meteotsunami that impacted the US East Coast. The existence of the meteotsunami was confirmed by several of the 30 tide gauges along the East Coast up through New England and was seen as far away as Puerto Rico and Bermuda. The event, which occurred during daylight hours, attracted widespread attention after several media reports were released focusing on local impacts including people being swept off a breakwater at Barnegat Light, New Jersey, some damage to boat moorings, and minor inundation.

Meteotsunamis generally do not have sufficient heights/energies to cause catastrophic loss of life, as do severe seismic tsunamis, although damage to harbors and coastal structures is common. The June 13, 2013 event, however, attracted significant attention among many agencies and scientific groups, probably due to its proximity to heavily populated areas.

4.1. Origin of meteotsunamis and nature of the June 13, 2013 event

A meteotsunami is generated by an atmospheric pressure disturbance traveling across the sea. An atmospheric anomaly (a low- or high-pressure center) will produce a small peak or trough moving at the same speed on the sea surface beneath it. This results in a freely propagating surface wave that increases in amplitude when the speed of atmospheric anomaly v_{aa} matches the shallow-water wave phase velocity $v_{ph}(d)$. This is known as Proudman resonance, see [17]. The speed v_{aa} of the June 13, 2013 derecho was about 21.1 m/s [15]. Substituting this value for $v_{ph}(d)$ into Eq. (5), it follows that the onset of the independent wave occurs at a depth d equal to 45 m, which lies about 60 km off the New Jersey coast.

This meteotsunami was unusual because it was generated by a frontal pressure anomaly traveling offshore. Yet coastal sensors including HF radars indicate that the meteotsunami approached the coast. Numerical models [8] indicate that a strong reflection occurred at the shelf edge about 110–120 km offshore, where the depth decreases from 100 to 1200 m over a distance of 20 km. The reflection is greater when a wave interacts with a drop-off rather than a step-up with the same slope. Data from New Jersey radars confirm the existence of a wave reflected from the shelf edge back toward the coast. This wave was also detected by coastal tide gauges.

To explain these results, we consider the interaction of the tsunami with a hard boundary, assuming a single pulse of water approaching the coast, that is, a traveling wave. The forward velocity is maximum at the wave crest. As a boundary is approached, there is a hard reflection:

http://dx.doi.org/10.5772/63960

the velocity goes to zero and the height doubles. This is known as the Neumann boundary condition. After a period of time from the reflection, a single wave travels outwards, with the crest velocity and height maxima in phase again.

In reality, the situation is more complex. Instead of a single wave or soliton, a series of positive and negative tsunami peaks often resemble a sine wave for height and velocity. The hard-wall boundary condition causes the height peaks to lag the velocity peaks by as much as a quarter cycle, which is termed the "quadrature effect." After reflection, the height stays positive but the velocity amplitude becomes negative. The interaction of incoming and reflected waves constitutes a more complex partial standing-wave situation, which is well handled by numerical model solutions.

4.2. Radar detection of the 2013 US East Coast meteotsunami

We analyzed data sets from three SeaSonde HF radar systems located in New Jersey: BRNT, BRMR, and BELM. Radar transmit frequencies and range cell widths were approximately 13.5 MHz and 3 km, respectively. Radar results were compared with data from NOAA tide gauges at Atlantic City and Sandy Hook, New Jersey. **Figure 12** shows the locations of the radars and tide gauges, and the offshore bathymetry. The meteotsunami height at the neighboring DART buoy, located about 240 km to the east, was only 5 cm [15].

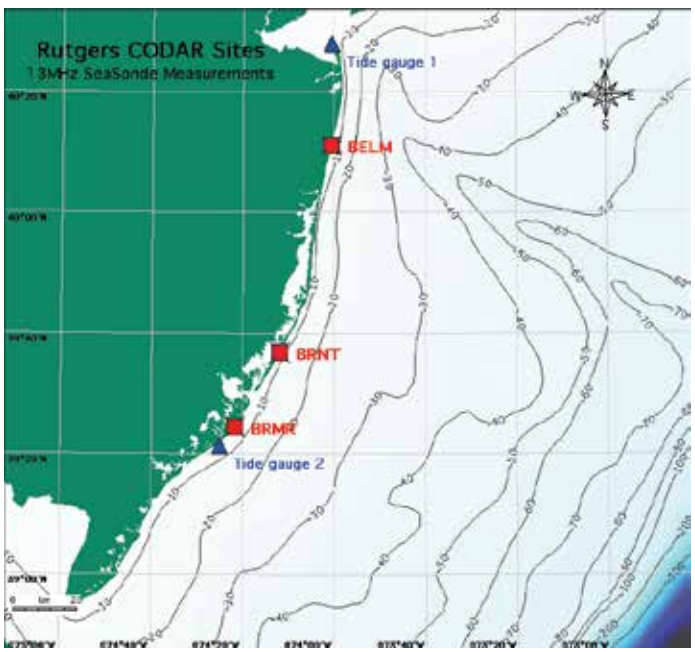

Figure 12. The radar stations at Brant Beach (BRNT), Brigantine (BRMR), and Belmar (BELM); the NOAA tide gauges at Sandy Hook (tide gauge 1) and Atlantic City (tide gauge 2) and the offshore bathymetry contours, with depths in meters.

Atlantic City tide gauge data obtained from the NOAA website [16] are shown in **Figure 13**.

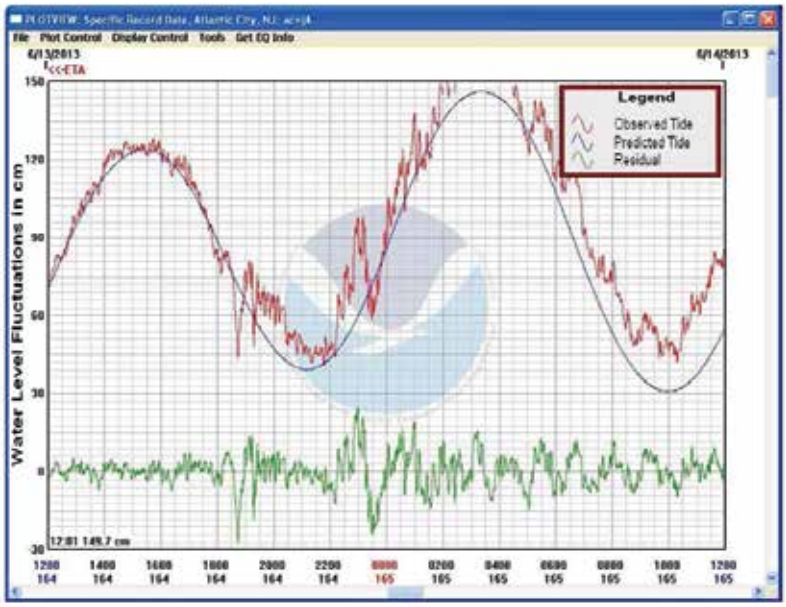

Figure 13. NOAA tide gauge observations June 13, 2013 at Atlantic City, NJ.

Readings show a maximum negative meteotsunami signal at approximately 18:42 UTC, indicated by the sharp water-level decrease. This is followed at approximately 22:00 UTC by a sharp increase in water level and subsequent oscillations.

As described in Section 3.3, the radar coverage area is divided into rectangular area bands 2-km wide and approximately parallel to the depth contours. Radial vectors within each area band were resolved parallel and perpendicular to the depth contour. These velocity components are then averaged over the bands.

Figure 14 shows time series of four perpendicular band velocities from BRNT and BRMR and the corresponding *q*-factors, obtained from the four bands [6].

The arrival of the meteotsunami is signaled by a marked decrease in the perpendicular band velocity component, indicating an outflow, followed by correlation between different area bands. The parallel component did not display the tsunami signature. The water level measured by closest tide gauge at Atlantic City decreases when the tsunami arrives, as shown in **Figure 13**, also indicating an outflow of water.

The tsunami signal at BELM was far less, which is consistent with tide gauge measurements at Sandy Hook, 30 km to the north, which barely registered the tsunami arrival.

About 4 h later, after 22:00 UTC, BRNT velocities first increase and then sharply decrease, as is also shown by the Atlantic City tide gauge (see **Figure 13**). This effect was not seen at BRMR or BELM.

http://dx.doi.org/10.5772/63960

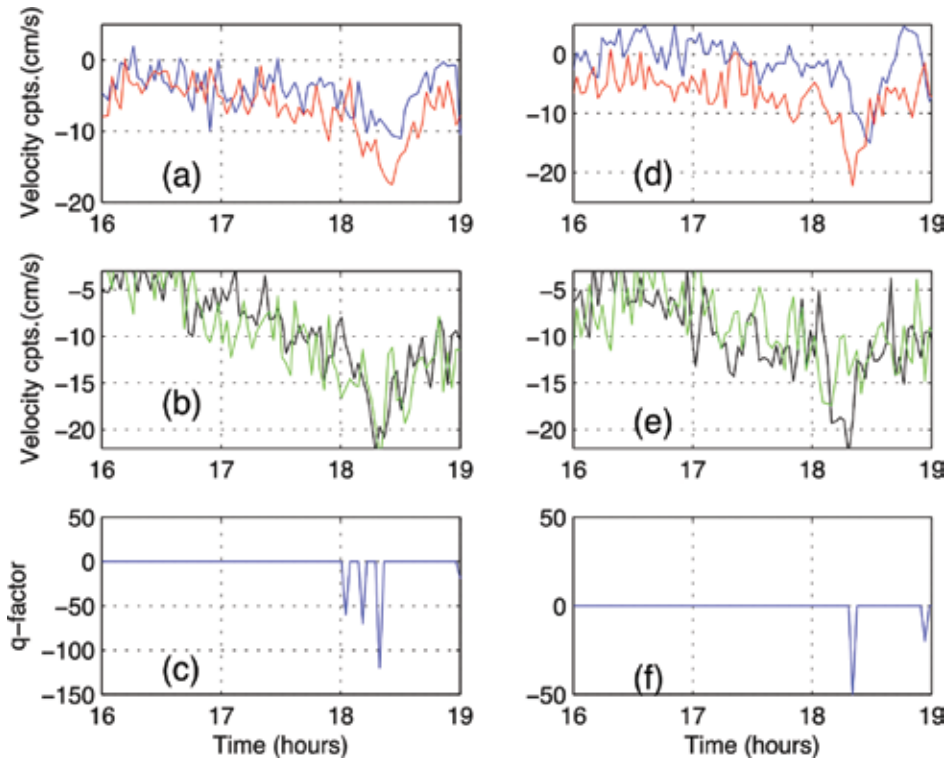

Figure 14. The meteotsunami arrival observed by radars BRNT and BRMR: band velocity components and the corresponding *q*-factors plotted against hours from 00:00 June 13, 2013. BRNT: (a) 6–8 km (blue), 8–10 km (red), (b) 10–12 km (black),12–14 km (green), (c) Corresponding *q*-factors. BRMR: (d) 2–4 km (blue), 6–8 km (red), (e) 14–16 km (black), 20–22 km (green), (f) Corresponding *q*-factors.

To demonstrate more clearly the meteotsunami velocity trough as it approached the coast, BRNT band velocities were further processed as follows: the band velocities were first detrended over time, removing effects with time scales longer than 1.5 h, such as those due to tides. The detrended band velocities were then low-pass filtered and, to further reduce noise, averaged over two adjacent bands.

Figure 15 shows the smoothed velocities plotted as a function of time vs. range from shore, the dashed line indicating the progression of the first tsunami trough. Tsunami hindcast modeling [15] confirms this time-distance progression of the meteotsunami as it moved toward shore.

Figures 14 and **15** show that the tsunami arrived first at the most distant ranges and progressively later moved toward the coast. To compare these results with theory, the tsunami arrival time at BRNT was calculated using Eq. (10), based on an initial detection at range 23 km. The bathymetry contours offshore from BRNT shown in **Figure 12** were approximated by parallel contours, giving depth as a function of distance. As discussed in Section 2, this approximation is valid, as the tsunami is not affected by perturbations in depth with spatial scales far less than

its wavelength. This analysis assumes no coastal boundary and results are expected to differ somewhat from radar-observed arrival times, as the orbital velocities are affected by shallow water.

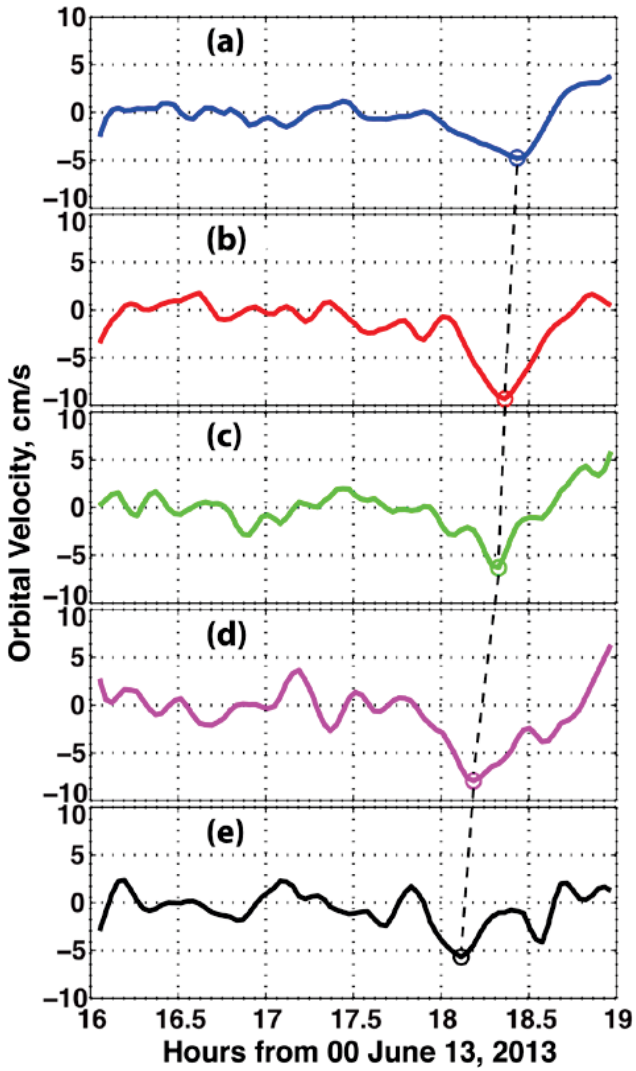

Figure 15. BRNT band orbital velocities plotted as a function of time, dstance from shore: (a) 6 km, (b) 10 km, (c) 14 km, (d) 18 km, and (e) 22 km. The progress of the first tsunami trough minimum is shown by the dashed line.

Figure 16(a) shows the different arrival times plotted vs. distance from shore. For the radars, arrival time was defined to correspond to the minimum tsunami velocity value; for the tide gauge, it was defined to correspond to the minimum water level. The solid curve shows the arrival times at BRNT calculated using Eq. (10), using the approximate depth vs. distance from shore plotted in **Figure 16(b)**.

http://dx.doi.org/10.5772/63960

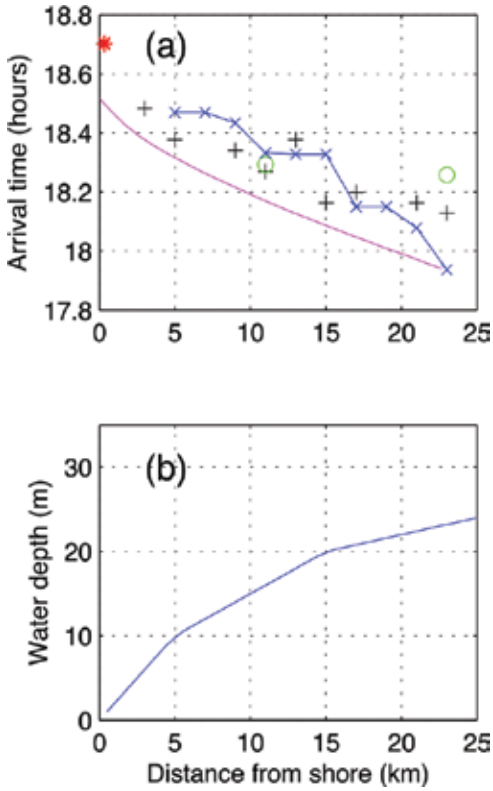

Figure 16. (a) The arrival time of the first tsunami trough observed by the radars plotted vs. distance from shore. Blue: BRNT, black: BRMR, green: BELM, red asterisk: arrival time at the Atlantic City tide gauge, and magenta: tsunami arrival time calculated from Eq. (10). Time is measured in hours from June 13, 2013, 00:00 UTC. (b) Depth plotted vs. distance from BRNT perpendicular to depth contours.

It can be seen from **Figure 16(a)** that the meteotsunami arrived 23 km from the coast at BRNT and BRMR at about the same time. It then traveled toward shore at approximately 30 km/h. The meteotsunami arrived about 14 min later 23 km offshore from BELM. The two BELM readings indicate that it then moved toward shore at a higher speed, probably due to deeper water near the Hudson Canyon. The tsunami arrived at the Atlantic City tide gauge 47 min after it was first observed by the BRNT radar.

The initial velocity observed by the radars was offshore, indicating a "trough" on the ocean surface. This was also observed by closest tide gauge at Atlantic City. However, as shown in **Figure 15**, the tsunami wave itself approached the coast due to a strong reflection occurring at the shelf edge 110–120 km from shore, see Section 4.1.

The meteotsunami was detected by the radars 23 km from the coast. It arrived at the shore 47 min later, as indicated by the tide gauge measurement of water level shown in **Figure 13**. The measured tsunami height was approximately 50 cm. These observations suggest that for similar tsunami height and bathymetry conditions, HF radar can provide a three-quarter hour warning alert before the wave strikes the shore.

5. Calculation of simulated tsunami velocities and heights

Tsunami simulation provides an understanding of many of the factors affecting the capability of coastal HF radars to provide tsunami observation and warning. Ultimately, this can lead to performance assessment for a radar at a given site based on local bathymetry. Orbital velocities are tracked vs. time and related to the tsunami wave intensity. Comparisons with the background current field allow the assessment of possible warning time and wave amplitude as the tsunami approaches the coast near the radar. In this section, we describe two methods for simulating tsunami velocities: the first based on solving the fundamental equations to give total velocity/height maps and the second based on application of Green's Law to give simulated band velocities.

5.1. Simulation based on solution of the fundamental equations of motion

To simulate tsunami height and velocity, Eqs (2) and (3) are solved numerically within the radar coverage area, typically out to ~50 km from the coast. The offshore bathymetry is included as the depth variable, $d(x,y)$, and the coastline becomes a boundary for the domain. First, the scalar Eq. (3) is solved for the tsunami wave height. Then, velocity is obtained by integrating the left side of Eq. (2) over time, after linearization as described in Section 2.1. This establishes the relations between the orbital velocity measured by the radar and the tsunami wave height, as well as provides the time of arrival at the coast from any point in the near-field region.

5.1.1. One-dimensional tsunami

We examine here how a simple one-dimensional wave approaching normally to the coast behaves when it encounters a steep continental slope starting from depth 1000 m at a distance of 70 km from shore and sloping upwards to depth 100 m, at a distance of 50 km from shore. How do both height and orbital velocity change as they traverse this shelf? How much is transmitted across the shelf and how much gets reflected? On the return of the ray reflected by the coast, is there a second reflection going back toward shore? Answers to these questions are provided by Video 2 that can be viewed at http://bit.ly/29nKuLh Elapsed time in minutes is given in each frame of the movie. Colors represent the wave height (blue) and the orbital velocities (red). The coast was taken to be a Neumann reflecting boundary, that is, velocity stops perpendicular to the coast, where its magnitude is zero. The bottom profile including the shelf is shown as the heavy black curve at the top in the video. We note several points indicated by the video:

- The normalized height wave and orbital velocity wave come in from the right, toward the coast at the left. For this exact solution, the orbital velocity grows much faster than height as the wave advances onto the shallower shelf. This also follows from the Green's Law approximation given by Eqs (6) and (7), which indicates that height depends on depth d as $d^{-1/4}$, while velocity varies as $d^{-3/4}$.

http://dx.doi.org/10.5772/63960

- After coastal reflection, the height remains positive, while the direction of the velocity for the outgoing wave reverses. This is also true of the initial reflection at the bottom of the shelf-edge slope, although this is below the visibility level in the movie. Thus, the reflected velocity changes sign while the height does not.
- The offshore retreating waves after coastal reflection encounter another strong reflection as they reach the top of the shelf edge 50 km offshore. In fact, these backward-reflected waves explain the meteotsunami that was observed in June 2013 from the New Jersey coast as discussed in Section 4. The original tsunami was launched by Proudman resonance [17] from the eastward-moving low-pressure center. When an atmospheric anomaly like a low-pressure center travels across the sea at the same speed as the shallow-water phase velocity (which depends on inverse square root of depth), a match or "resonance" is achieved. This causes the mound of water uplifted by the atmospheric low to break free and propagate as a tsunami soliton wave on its own. It was the returning reflected tsunami that impacted the coast and was reported by several radars and coastal tide gages. For more details, see [6] and Section 4.

It is from the output files of this one-dimensional simulation that we deduced the transmission coefficient cited in Section 2.4, which was compared with predictions from the Green's Law approximation.

5.1.2. Two-dimensional tsunamis

We now examine two more realistic scenarios: in the first, a plane wave tsunami approaches the Portuguese West Coast and in the second, a tsunami is generated by a point source in the Alboran Sea. Videos are provided, which show tsunami height and velocity normalized by their initial values, as the tsunami is refracted by the bathymetry and reflects from the coast. In these videos, the background color represents the tsunami wave height normalized by its initial value, with the magnitude indicated by the color bar. Velocity vectors overlain on top of the height background represent the orbital velocities normalized by the initial value, with the magnitudes indicated by the vector length. Elapsed time shown on each frame indicates the time taken for the tsunami to reach various points along the coast. These simulated values can be tested against radar observations of real tsunamis. In both cases, reflection of the wave from the coast is clearly visible and the tsunami velocity increases more rapidly than the height as depth decreases, indicating that observed velocities provide a sensitive alert flag for a tsunami approaching the coast. Future work on this simulation will study results related to actual heights and velocities, rather than normalized values; output values can then be tested against radar observations of real tsunamis.

5.1.2.1. Portugal

The 1755 Lisbon earthquake in combination with subsequent fires and a tsunami almost totally destroyed Lisbon and adjoining areas. Tsunamis as tall as 20 m swept the coast of North Africa, and struck Martinique and Barbados across the Atlantic [18].

Using the actual offshore bathymetry, we simulated a tsunami approaching the Portuguese coastline from the west, results are shown in Video 3, available at http://bit.ly/29l4vCx Bathymetry contours are shown in order to understand the tsunami refraction. The epicenter was located more than 200 km to the west of the map. When the source is so distant, the initial condition for solving the PDE can be taken to be a plane wave, corresponding to a ridge of water traveling eastward. This approximation is reasonable whenever the source is distant from the near-field region and is convenient to model for numerical solutions. The domain for the numerical solution consists of the coastline of interest and the open box edges over the ocean. The coastline was assumed to have a Neumann (reflective) boundary condition.

This region was also selected for study because there are three 13.5-MHz SeaSonde HF radars operating at nearby locations, which are shown by green squares in the video. Tsunami observation software is being installed at these sites. The three radars would not see the tsunami if its propagation followed the line of sight from the source because the coast of southern Portugal would shadow those paths. In fact, the model output shows how the tsunami wave refracts and approaches the sites from the south. Reflection of the wave from the coast is clearly visible.

5.1.2.2. Alboran Sea

Another region of recent interest is the Alboran Sea, which is enclosed on three sides by Gibraltar on the west, Spain on the north and Morocco on the south. There are seismically active regions near tiny Alboran Island that could raise a localized mound of water, which would spread out under the influence of gravity, initially radiating a near-circular tsunami wave.

A point source is another initial condition that is easy to handle in the PDE solution [9]. Resulting maps are shown in Video 4 that can be viewed at http://bit.ly/29gMdPA.

The tsunami point source is located near Alboran Island (the green square marker) in water that is 1000 m deep. The tsunami radiates in all directions, intensifying in height and velocity as it moves into shallow water, as indicated by the bathymetry contours. As before, background color represents normalized height and vector length represents normalized velocity.

One can see as the movie progresses how different coastal regions are affected, as the approaching tsunami intensity increases. Offshore reflections and along-shore tsunami vectors are clearly seen from the vectors. The island is small compared to the tsunami wavelength, causing little observable effect.

5.2. Band-velocity simulation based on Green's Law

This approximate procedure is based on the theory given in Section 2.3. To simulate velocities for a given test radar site over a period of time close to the arrival of a tsunami, band velocities from a real tsunami (termed reference velocities V_{Ref}) are superimposed on band velocities measured at the site (termed site velocities V_{Site}). Before adding to the site velocities, the reference velocities are adjusted for the site bathymetry using Eq. (7). They are then multiplied

http://dx.doi.org/10.5772/63960

by an arbitrary factor F that can be varied to adjust the height of the simulated tsunami approaching the test site. This process is encapsulated in Eq. (11) for a given band:

$$V_{Sim} = V_{Site} + F * V_{Ref} * \left(Depth_{Ref} \Big/ Depth_{Site} \right)^{3/4} \tag{11}$$

where V_{Sim} is the simulated velocity that for $F = 1$ would be observed if the reference tsunami approached the test site and $\text{Depth}_{\text{Site}}$ and $\text{Depth}_{\text{Ref}}$ are the average depths across the band for the test and reference sites. Increasing/decreasing the value of F will increase/decrease the size of the simulated velocity.

Simulated band velocities calculated using this approximate method are currently used to evaluate the suitability of radar sites for tsunami detection, as described in the next section.

6. Evaluation of radar sites for tsunami detection using simulated tsunami velocities

As some sites are less suitable than others for tsunami monitoring with coastal radar systems, we are developing a site-dependent method that uses simulated tsunami velocities to estimate the size of a tsunami required to trigger a detection as a function of distance from the shore. This leads to an estimate of the warning time available. The tsunami simulation methods currently available have been discussed in the previous section. Tsunami simulation based on PDE model solutions of equations of motion is under development at this time with early results discussed in Section 5.1. As it does not yet produce actual (non-normalized) heights and velocities, as an interim measure, we use the approximate simulated velocities based on Green's Law described in Section 5.2.

6.1. Evaluation method

The following steps are used to estimate the size of an approaching tsunami required for detection at the test site.

- **Step 1:** Measured tsunami band velocities obtained over a 5-h time period from the reference site V_{Ref} are stored in a database.
- **Step 2:** The test site is assumed to be operating in its normal mode acquiring radial velocities, which are converted to band velocities V_{Site} as described in Section 3.2 over a 5-h time period.
- **Step 3:** The reference set V_{Ref} is adjusted for depth, multiplied by a factor F, and added to V_{Site} using Eq. (11) to produce simulated velocities V_{Sim} over the 5-h time period.
- **Step 4:** The simulated velocities V_{Sim} are analyzed to produce q-factors, using the pattern-recognition algorithm described in Section 3.3.

- **Step 5:** Steps 3 and 4 are repeated for a range of values of the factor F. The minimum value of $F(F_{\text{detect}})$ is sought that will lead to an acceptable detection of the q-factor peak, with an acceptably low false-alarm rate.
- **Step 6:** The tsunami velocity (V_{detect}) and height (H_{detect}) necessary to produce an initial detection of the tsunami follow from Green's Law, Eqs (6) and (7):

$$\mathrm{V}detect = F_{detect} * \mathrm{V}_{ref}^{init} * \left(\frac{Depth_{Ref}}{Depth_{Site}} \right)^{3/4} \tag{12}$$

$$H_{detect} = \sqrt{\frac{Depth_{Site}}{g}} V_{detect} \tag{13}$$

where $V_{\text{ref}}^{\text{init}}$ is the magnitude of reference velocity oscillation leading to a detection of the tsunami arrival. Note that in these equations, V_{detect} and H_{detect} define the values where the band velocities are measured, not values very close to shore in the run-up zone, that can only be calculated using the highly nonlinear theory.

These steps are repeated using a sliding 5-h time window, running in the background of an operating radar system. The work described in this section is preliminary in nature and is being further developed in partnership with NOAA.

6.2. Application at two test sites

We demonstrate the procedure for a single 5-h time window using as reference band velocities measured by the Kinaoshi radar (A088) during the Tohoku (Japan) tsunami, see **Figure 4**. Test radar sites are located at Bodega Marine Laboratory (BML1) on the US West Coast and Brant Beach (BRNT) on the US East Coast. BML1 has a steep offshore bathymetry profile, that is a narrow continental shelf; it also has low background noise. In contrast, BRNT has a shallow offshore bathymetry profile, that is a wide continental shelf, but this site has higher background noise. Our analysis shows that for these two radar sites, the offshore bathymetry dominates the tsunami detection capability. We compare predictions from the simulation with detections of real tsunamis: at BML1 of the 2011 Tohoku event and at BRNT of the 2013 meteotsunami.

Figure 17 shows depth vs. distance offshore for the reference site and the two test sites.

Clearly, depths for BRNT are much less than those for BML1, which is advantageous for tsunami detection because it offers longer time from the first alert to the arrival at the coast. However, the signal-to-noise ratios for the BRNT antennas were observed to be about 20 dB less than those for BML1, indicating noisy spectra and reduced tsunami detection capability. This is an example of variations in local external noise that are sometimes seen among coastal HF radars.

http://dx.doi.org/10.5772/63960

As the Green's Law approximation applies only when the depth varies slowly compared to the tsunami wavelength, we consider distances from BML1 less than 19 km, which correspond to the edge of the continental shelf, see **Figure 17**. For BRNT, this limit does not apply, as here the continental shelf extends beyond the limits of the radar coverage.

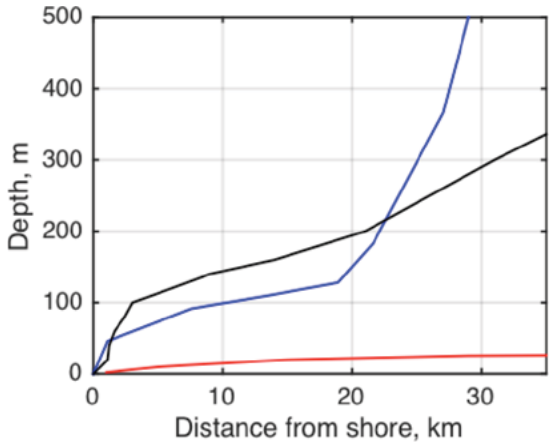

Figure 17. Depth vs. distance from shore for A088 (black), BML1 (blue), and BRNT (red).

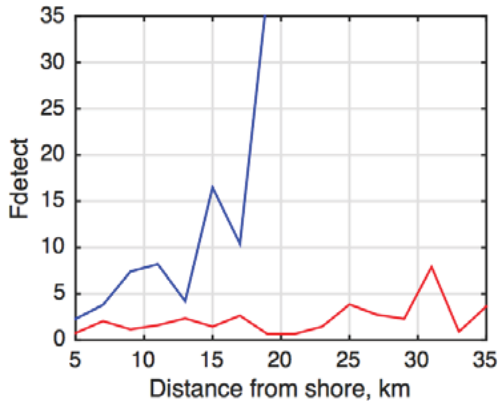

Figure 18. The multiplicative factor F_{detect} required for detection of the initial approach of the simulated tsunami vs. range from the radar. Blue: BML1 and red: BRNT.

With the empirical detection algorithm applied to noisy background velocities, a nonlinear pattern results as the multiplicative factor F is varied in Step 5 of the evaluation analysis described in Section 6.1. As F is increased from zero, the q-factor increases in stages as different components of the detection methods apply to the band velocities. When the q-factor exceeds the preset limit, this defines the value of $F(F_{detect})$ that signals a detection. Preset limits are set to produce minimal false alarms while allowing detection of observed tsunamis. In **Figure 18**,

F_{detect} is plotted vs. range from the radar: range is defined as the central value for the five 2-km bands, for example, for bands 1–5 (distance from shore 0–10 km), the central value is 5 km.

Step 6 of the analysis procedure is then applied to estimate for each range the tsunami velocity and height necessary for the detection of the initial tsunami approach. Parameters to insert into Eqs (12) and (13) were estimated as follows: **Figure 7** indicates that the amplitude of the initial A088 (the reference) tsunami velocity oscillation V_{A088}^{init} is about 9 cm/s averaged from 0 to 10 km from shore, where the mean depth is approximately 60 m. Substituting these values, the depths from the site and the values of F_{detect} shown in **Figure 18**, into Eqs (12) and (13) leads to estimates for the tsunami velocity V_{detect} and height H_{detect} required for a detection of the initial simulated tsunami approach. **Table 3** shows these values as functions of distance from shore.

	Velocity (cm/s)		Height (cm)	
Range (km)	**BML1**	**BRNT**	**BML1**	**BRNT**
5	7.9	11.7	21.6	11.7
7	11.5	27.4	34.2	30.3
9	20.8	13.7	65.1	16.4
11	22.0	17.2	71.0	22.0
13	10.8	23.2	25.9	31.4
15	40.6	13.3	129.0	18.9
17	24.5	23.5	86.2	34.2
19	84.1	5.6	306.0	8.3
21		5.4		8.2
23		11.8		18.2
25		30.6		47.9
27		21.3		33.9
29		17.4		28.2
31		58.5		96.0
33		6.5		10.9
35		25.9		43.7

Table 3. Estimated tsunami velocity and height required for detection vs. range from the radar for the two sample test sites based on simulations using reference tsunami velocities from A088.

From **Table 3**, the height of the simulated tsunami required to trigger a detection is generally larger for BML1 than for BRNT particularly at greater ranges where the water is deeper. This occurs in spite of the lower BRNT signal-to-noise ratio, indicating that the shallow offshore

http://dx.doi.org/10.5772/63960

bathymetry dominates the tsunami detection capability. We note that values shown in **Table 3** are noisy. Noise reduction will require the analysis of more extended data sets.

6.3. Comparison of test predictions with prior observations of real tsunamis

In this section, we compare predicted values of tsunami velocity required for a detection (shown in **Table 3**) with observations of real tsunamis at BML1 and BRNT.

6.3.1. BML1

About 9 h after the March 11, 2011 Japan earthquake, the Japan tsunami was detected at BML1; see **Figure 19**, which shows the measured band velocities and corresponding q-factors close to the tsunami arrival.

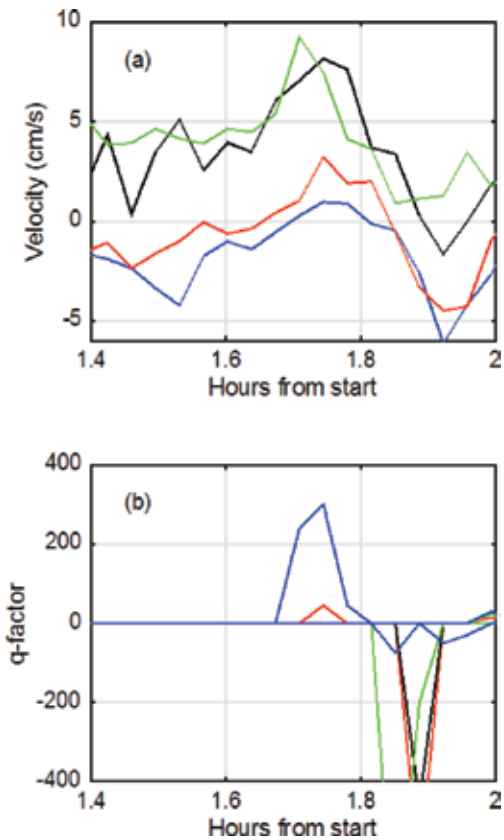

Figure 19. BML1 results; start time March 11, 2011, 14:00 UTC: (a) band velocities vs. time. Blue: 0–2 km, red: 2–4 km, black: 4–6 km, and green: 6–8 km; (b) q-factors vs. time obtained from analysis of velocities from five adjacent bands. Blue: 0–10 km, red: 2–12 km, black: 4–14 km, and green: 6–16 km.

Using a threshold of 250, the blue q-factor peak for bands 1–5 indicates a detection of the Japan tsunami arrival at 15:45. **Figure 19(a)** shows that the amplitude of the initial tsunami velocity

oscillation at BML1 was about 7 cm/s. There was no detection of the initial tsunami approach further from shore.

From **Table 3**, the simulation test predicts that the tsunami velocity required for an initial detection at BML1 at a 5-km range is ~8 cm/s, which is approximately consistent with the observed velocity (7 cm/s) resulting in the initial detection of the Japan tsunami. The test indicates that larger tsunami velocities are required further from shore for detection to be possible. It also gives credibility to our simulation methodology.

6.3.2. BRNT

From **Figure 14**, the magnitude of the initial meteotsunami velocity oscillation observed at BRNT 6–12 km from shore was ~10 cm/s. This value can be compared with the test results in **Table 3**: averaging from 5 to 11 km, the predictions indicate that the velocity required to produce a detection is ~17 cm/s. This conservative estimate may reflect a difference between the characteristics of a meteotsunami and an earthquake-caused event.

7. Factors affecting detectability

In this section, we summarize five factors that can affect the ability of a radar site to detect and provide warning of an approaching tsunami.

7.1. Water depth

Tsunami orbital velocities are small in deep ocean basins, with orbital velocity below the detectability threshold for HF radars. In the deep ocean, tsunami wave amplitude is always less than 1 m and wavelengths may be hundreds of kilometers. For example, fishermen 30 km offshore did not detect the huge Japanese tsunami of June 15, 1896. The tsunami height was only about 40 cm, but when the tsunami arrived at the shore, its height after run-up was 38.2 m [19].

As the tsunami moves onto the continental shelf, both velocity and height increase. Velocity, however, grows more rapidly with decreasing depth which gives advantage to the radar sensor. As the depth decreases, the orbital velocity can exceed a detection threshold. Based on our experience with small to moderate tsunamis in 21 HF radar detections, we use the 200-m isobath as a convenient demarcation for likely detectability.

The offshore bathymetry has a strong influence on HF radar tsunami detectability that is highly radar site dependent. It must be studied in simulations that guide the selection of detectability thresholds and other parameters for any tsunami warning methodology. This can be done using numerical models for near-field tsunami propagation based on the bathymetry offshore from the radar location, as described in Section 5.1.

http://dx.doi.org/10.5772/63960

7.2. Tsunami height

The orbital velocity and tsunami height of course increase with the severity of the tsunami, and this is a second factor determining detectability. We note that tsunami heights producing radar detections as measured by neighboring tide gauges were not large, varying between 0.05 and 2 m. Tsunamis with orbital velocity amplitudes of 5 cm/s have been detected [5]. Detection of larger tsunamis would of course be easier, for example, the tsunami waves that reached heights of 40.5 m in Miyako, Japan, following the 2011 Tohoku earthquake [20] would be very easy to detect.

The estimation of the tsunami height at the shore is of course of major interest and at present can only be estimated by tide gauge observations because of the breakdown of linear modeling very close to shore. More advanced modeling, as described in Section 5.1, should alleviate this problem.

7.3. Background currents

The orbital tsunami current must be detected among the ambient background flows that depend on a number of site-specific factors. Tsunami detectability may be degraded if there are large variations in the ambient current field over the tsunami period, which for the Japan tsunami and the US East Coast meteotsunami was approximately 40 min.

Existing networks of coastal HF radars have been installed primarily for reporting real-time currents. Such currents vary with location and time. Temporal variations may be either predictable (e.g. tides) or unpredictable (due to many causes, such as storms). Their patterns within the radar coverage where tsunami detection is desired can be quite complex. Some background flow variations may be mistaken for a tsunami and hence produce a false alarm in the absence of a good pattern-recognition algorithm.

7.4. External background interference/noise

Man-made radio interference may lead to radar signatures similar to those produced by a tsunami, leading to false alarms. In some cases, this interference can be mitigated; in others, it may not be possible. This problem can often be solved on a case-by-case basis, having collected a database of received signals. This is the biggest factor apart from the intensity of a tsunami that limits its detection and can give rise to false alarms if the threshold is too low. Even sporadic interference can cause the q-factor pattern-recognition algorithm to give rise to false alarms. Initial radio surveys for new radar sites are required to check for interference. Selection of a clean frequency band can improve the situation for all sites.

Methods are needed to detect interference, along with filtering where possible to remove it. If it cannot be removed, then passing along to a tsunami warning center a disclaimer with any q-factor alerts during high interference periods, or raising the threshold, is critical.

7.5. Signal aliasing

Strong echoes from close-in ranges can alias into distant range cells in systems that transmit while receiving. This "ringing" phenomenon produces spurious echoes in distant range cells that can be erroneously interpreted to be tsunami echoes. These far-out spurious echoes are easily distinguished from real tsunami echoes, as they appear at the same time as the real tsunami echoes from close-in ranges. If they were caused by a real tsunami, they would appear earlier at distant ranges. Also current amplitudes extracted from the spurious echoes are usually independent of depth. Fundamental, linear shallow-water wave physics [1, 6] shows that the current amplitudes always decrease with depth. Observations from Chile of the Japan tsunami [4], discussed in Section 3.4.3, appear to show indications of "ringing."

8. Dealing with false alarms

The first tsunami alert is indicated when the q-factor exceeds the preset limit. Due to the varying background current and noise/interference effects described in the last section, the detection might be a false alarm. The trade-off in the selection of the q-factor threshold is as follows: if the q-factor limit is set too low, the peak will certainly produce a q-factor alert, but many non-tsunami false-alarm detections may be generated, degrading performance and operational acceptability. If it is set too high, false alarms will be eliminated, but then the first actual tsunami peak may be missed. This is the classic "probability-of-detection vs. false-alarm rate" trade-off encountered by warning sensor systems. An acceptably low false-alarm rate for a given tsunami intensity and detection distance from shore are the parameters to be optimized at each site. Judging by the strength of the q-factor signals seen in the Japan tsunami, it would appear that a tsunami having a run-up height of 1 m should easily be detectable with very low false-alarm rates in uncontaminated radar spectra, using the detection methods described earlier. The value of the q-factor limit defining a tsunami detection is site specific and needs to be studied for the site under consideration. The most effective way to handle this for a given site is to study the background currents/extraneous effects and how the q-factor algorithm responds to them over a several month period.

We discuss two approaches for the reduction of false alarms:

8.1. Search for correlations between q-factor alerts from adjacent HF radars

A real tsunami would be seen at two coastal locations say 30 km apart, for example, within a definable time window (say 15 min). Tsunami waves refract as they move into the ever-shallower water of the continental shelf near the coast. This means they tend to arrive perpendicular to the shore. This forces similar arrival times at neighboring locations along a nearly straight coastline.

Hence, if a high q-factor peak at Radar M arrives at a given range within 15 min of a high q-factor peak at Radar N, the presence of both raises the probability that a real tsunami is being seen by orders of magnitude. Likewise, if a high q-factor at Radar M has no counterpart at

http://dx.doi.org/10.5772/63960

Radar N, this raises greatly the probability that the "alert" was in fact a false alarm. Thus, the solitary alert can be either eliminated as a false alarm or attached a flag to give it a much lower credibility.

8.2. Search for correlations between q-factor alerts and earthquake notifications

At present, several services distribute online notifications within 2 min of an earthquake that has occurred anywhere in the world, which give latitude, longitude, time, and magnitude of the earthquake, see, for example [21]. Not all subsea earthquakes generate tsunamis. The assumption here is that any subsea earthquake with magnitude higher than 5 can be considered to be the origin of a tsunami. The approximate expected arrival time can be calculated from Eq. (10) using the depth profile between the earthquake origin and the radar near field of interest. A threat window can be set up within ±0.5 h of the predicted arrival time, and any q-factor candidates within this window would be given increased priority.

9. Conclusions

The use of HF coastal radars to detect and warn of approaching tsunamis was proposed nearly 40 years ago [1]. Radars measure the tsunami wave's orbital velocity, unlike all other tsunami sensors that measure its height. However, it was not until the 2004 tragic Banda Aceh event that killed a quarter of a million people that attention was seriously focused on developing a local warning system. After the significant 2011 Tohoku, Japan tsunami, enough radars were in place worldwide to gather a radar-signal database that allowed the development of detection and warning methodology.

Several papers ensued demonstrating a detection algorithm and developments followed toward a methodology to capitalize on this near-field monitoring capability [2–3, 5–6]. The present work presents a summary of these prior works and also covers recent work on tsunami simulation and site evaluation that has not been reported elsewhere.

In the last 5 years, tsunami events were detected by 21 SeaSonde HF coastal radars. Times between detection and arrival at shore (as confirmed by tide gages) ranged between 1 and 43 min. This alert time for a tsunami of given intensity depends principally on the offshore bathymetry. A shallow shelf edge affords a much longer alert time than a steep drop-off. We have examined and compared approximate and exact methods for estimating the arrival. The latter include the solution of exact linear partial differential equations, especially suited to near-field HF observations; in the future, this will also allow the radar-measured orbital velocity to be related to the height of the approaching wave.

We have also described steps toward simulation of tsunami height and velocity. This allows the assessment of the warning possible at a given site location based on the offshore bathymetry, background currents, and noise. False-alarm rate and probability of detection are the metrics against which performance is evaluated. Methods of increasing the latter while

decreasing the former are examined. These include correlations with similar alerts from other nearby radars and with reports on seismic events that may constitute tsunamigenic sources.

After radars on the US East Coast detected a meteotsunami in 2013 that provided an alert that was missed by conventional methods, NOAA recognized the potential that the US Integrated Ocean Observing System (IOOS) could offer for tsunami warning. IOOS consists of 130 SeaSonde radars around the US coast. The NOAA Tsunami Warning Program office and IOOS entered into a partnership with Codar Ocean Sensors to optimize this capability based on steps outlined in this report and organized its transition to the two operational tsunami warning centers in Hawaii and Alaska.

It is clear that early local detection of incoming tsunamis by deployed radar systems is now within the capabilities of existing technology.

Acknowledgements

Many thanks to Mason Kwiat for his invaluable help with the videos.

Author details

Belinda Lipa[1*], Donald Barrick[2] and James Isaacson[3]

*Address all correspondence to: Belinda@codar.com

1 Codar Ocean Sensors, Portola Valley, CA, USA

2 Codar Ocean Sensors, Mountain View, CA, USA

3 Codar Ocean Sensors, Sunset Valley, TX, USA

References

[1] Barrick, D.E. A coastal radar system for tsunami warning. Remote Sens. Environ. 1979, 8, 353–358.

[2] Lipa, B., Barrick, D., Saitoh, S.-I., Ishikawa, Y., Awaji, T., Largier, J., Garfield, N. Japan tsunami current flows observed by HF radars on two continents. *Remote Sens*. 2011, *3*, 1663–1679.

[3] Lipa, B., Isaacson, J., Nyden, B., Barrick, D (2012a) Tsunami arrival detection with high frequency (HF) radar. *Remote Sens*. 4: 1448–1461.

[4] Dzvonskovskaya A. Ocean surface current measurement using HF radar during the 2011 Japan tsunami. In: Proceedings of the IEEE International IGARSS Conference, p. 7605–7608, Munich, Germany, 22-27 July 2012.

[5] Lipa B, Barrick D, Diposaptono S, Isaacson J, Jena BK, Nyden B, Rajesh K, Kumar TS (2012b) High Frequency (HF) Radar detection of the weak 2012 Indonesian tsunamis. Remote Sens., 4: 2944–2956.

[6] Lipa, B., H. Parikh, D. Barrick, H. Roarty, and S. Glenn. High Frequency Radar Observations of the June 2013 US East Coast Meteotsunami. Natural Hazards. 2013, doi: 101.1007/s11069-013-0992. Meteorological Tsunamis: The U.S. East Coast and Other Coastal Regions, Chapter 5. ISBN-13: 978-3319127118. [Internet]. 2013. Available from http://bit.ly/29dY8RI. [Accessed 2016-06-08]

[7] V. Titov and F. González, "Implementation and testing of the Method of Splitting Tsunami (MOST) model", NOAA Tech. Memo. ERL PMEL-112 (PB98-122773), NOAA/ Pacific Marine Environmental Laboratory, Seattle, WA, 11 pp, 1997]

[8] H. Mofjeld, V. Titov, F. Gonzalez, and J. Newman, "Analytic theory of tsunami wave scattering in the open ocean with application to the North Pacific", NOAA Tech. Memo. OAR PMEL-116, 38 pp., 2000.

[9] Partial Differential Equation Toolbox™ 1 User's Guide, MATLAB, The Mathworks Inc., Natick, MA 01760, 2012, ch3.

[10] Kinsler L, Fundamentals of Acoustics. 4th ed. Wiley India Pvt. Limited; 2009. 568p. ISBN-13: 978-0471847892

[11] Green G, On the motion of waves in a canal of variable depth G Green - Cam. Phil. Trans., VI: 1837. 457 p.

[12] Kinsman B, Wind Waves: Their Generation and Propagation on the Ocean Surface Dover Earth Science: 2012. 704 p. Dover Publications (July 17, 2012) ISBN-13: 978-0486646527

[13] Lipa, B.J. and D.E. Barrick (1983), Least-squares methods for the extraction of surface currents from CODAR crossed-loop data: Application at ARSLOE, *IEEE J. Oceanic Engr*., vol. OE-8, pp. 226-253.

[14] Lipa, B., B. Nyden, D. Ullman, and E. Terrill (2006), SeaSonde Radial Velocities: Derivation and Internal Consistency: *IEEE Journal of Oceanic Engineering*, vol. 31, pp. 850-861

[15] Hammond S. (2013) Teleconference on Meteotsunami, July 18. [Internet]. 2013. Available from: http://bit.ly/29hU6WZ [Accessed 2016-06-08] [http://bit.ly/29hTRLF [Accessed 2016-06-08]

[16] Tsunami of June 13, 2013 (Northwestern Atlantic Ocean) [Internet]. 2013. Available from: http://bit.ly/29eO9rJ [Accessed 2016-06-08]

[17] Monserrat, Sebastià; Vilibic, Ivica; Rabinovich, Alexander B., Meteotsunamis: Atmospherically induced destructive ocean waves in the tsunami frequency band, Natural Hazards and Earth System Sciences 6(6): 1035-1051 (2006).

[18] 1755 Lisbon earthquake. [Internet]. 2016. Available from: http://bit.ly/29hp6ZV [Accessed 2016-06-08]

[19] 1896 Sanriku earthquake. [Internet]. 2016. Available from: http://bit.ly/29vJshV [Accessed 2016-06-08]

[20] 2011 Tōhoku earthquake and tsunami. [Internet]. 2016. Available from: http://bit.ly/1JcVdQh [Accessed 2016-06-08]

[21] SMS Tsunami Warning. [Internet]. 2016. Available from: http://bit.ly/29jWSJU [Accessed 2016-06-08]

Case Studies

Chapter 6

Tsunamis in Sweden: Occurrence and Characteristics

Nils-Axel Mörner

Additional information is available at the end of the chapter

http://dx.doi.org/10.5772/63956

Abstract

In the last 13,000 years, there are 17 tsunami events recorded in Sweden. This chapter highlights the characteristics of two high-magnitude events from the deglacial period and three events from Late Holocene age.

Keywords: tsunami events, tsunamites, Sweden, paleoseismicity, varved clay, turbidites, lake record

1. Introduction

In Sweden, we have documented 62 high-magnitude paleoseismic events in postglacial time [1, 2]. Most of those occurred in subaqueous environment and 17 events set up tsunami waves [3]. All the 62 events are documented by multiple criteria and most of them are very precisely dated.

With recording by multiple criteria, I mean the recording of one and the same event in faults and fractures, in sedimentary deformations, in liquefaction characteristics and spatial distribution, in earth- and rockslides, in height and extension of tsunami waves, in distribution and age of turbidites, etc.

With very precise dating, I mean dating with a resolution as to a single year (sometimes even the season of a year) in the Swedish Varve Chronology [4].

Therefore, studies in those uplifted former shelf areas may help us to understand the mode of offshore deformation and the special characteristics of structures created [5, 6].

Sweden with its bordering Baltic Sea and Kattegat Sea were previously thought to be tsunami-free parts of the world. In 1995, we found the first evidence of a major tsunami wave that took place in the autumn of varve 10,430 BP [7]. It was soon followed by the documentation of

another big tsunami event in the varve-year 9663 BP [8, 9]. Today, we have a list of 17 events [1, 3, 6]. In this chapter, I will discuss five of them in terms of case studies from this part of the world.

2. Paleoseismics and paleotsunamis

Table 1. lists the 17 tsunami events recorded and documented in Sweden up to now [3]. The corresponding spectrum of inferred wave heights is provided in **Figure 1** [6]. In the present chapter, five of the events will be picked out and discussed as case studies from Sweden and its surrounding seas [1].

Age in BP	*Area affected*	*Earthquake magnitude*	*Observed tsunami record*
12,400	Kattegatt	At least 8	Very high & strong wave
11,600	Kattegatt	At least 7	High wave
11,250	Kattegatt	About 7	High wave
10,430	Mälardalen	Well above 8	Very high & strong wave
9663	Hälsingland	Well above 8	At least 15 m wave height
9428	Umeå area	At least 7	(height unknown)
9221	Umeå area	7–8	At least some meters
8600	Södermanland	6–7	Probably some 5–10 m
7800	Stockholm region	At least above 6	Maybe 13 m run-up
6100	Hälsingland	Well above 8	At least 10-15 m height
4000	Umeå area	6–7	Tsunamite
3–4000	Södermanland	Explosive gas venting	At least 11 m run-up
3200	Lake Marviken	Around 7	Local lake tsunami
2900	Hudiksvall area	Explosive gas venting	At least 12 m wave height
2900	Forsmark area	Same as above	At least 6 m wave height
1600	Kattegatt	Unknown	Some meters run-up
776	South Kattegatt	Around 7	Destructive, tsunamites

Table 1. Tsunami events recorded in Sweden in association with paleoseismic events [1, 2].

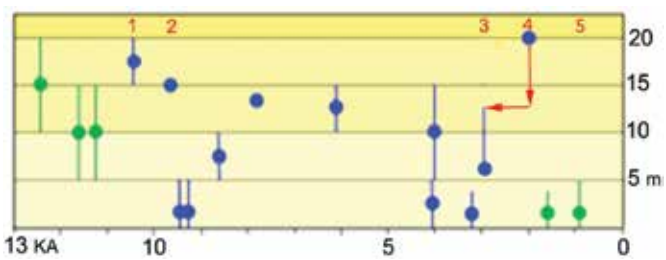

Figure 1. Recorded tsunami heights in the Baltic (blue) and Kattegat (green) coasts of Sweden [6]. Red figures (1–5) refer to the five events here discussed with event 4 being revised in time and wave height.

http://dx.doi.org/10.5772/63956

2.1. The 10,430 BP event

When ice receded over the Baltic basin, it dammed an ice lake in its front. The outlet was via the Great Belt area. The ice lake is known as The Baltic Ice Lake. Due to the successive land uplift with increasing amplitude to the north, the vertical damming above the corresponding Atlantic sea level successively increased to a final damming of 29 m. Due to ice recession, the ice lake grew in horizontal extension too. When the ice margin, shortly after the end of the Younger Dryas stadial, left the northern slope of Mt. Billingen in southern Sweden, the ice lake dropped to the level of the sea. This event occurred 10,740 varves BP [7]. Pack ice and meltwater discharge blocked open excess to the sea, however [8].

At the varve-year 10,430 BP (i.e., about 300 years after the drainage), the entire Baltic basin suddenly turned marine and the Yoldia Sea stage (*sensu strictu*) commenced [8]. The forces generating this change were a high-magnitude earthquake occurring in the autumn of varve 10,430 BP and a high-amplitude tsunami wave washing the Närke Straight free of blocking ice [1, 3, 4, 8, 9]. The wave height must have been in the order of 15–20 m, and several lake basins were invaded by a high wave, recorded as tsunamites of graded bedding and including planktonic marine microfossils [1].

In 1995, we got excellent, extensive and multiple sections and trenches in connection with the construction of a new motor highway and a railway some 70 km west of Stockholm [10–12]. There were remarkable liquefaction structures, ground-shaking structures and deformed annual varves (**Figure 2**).

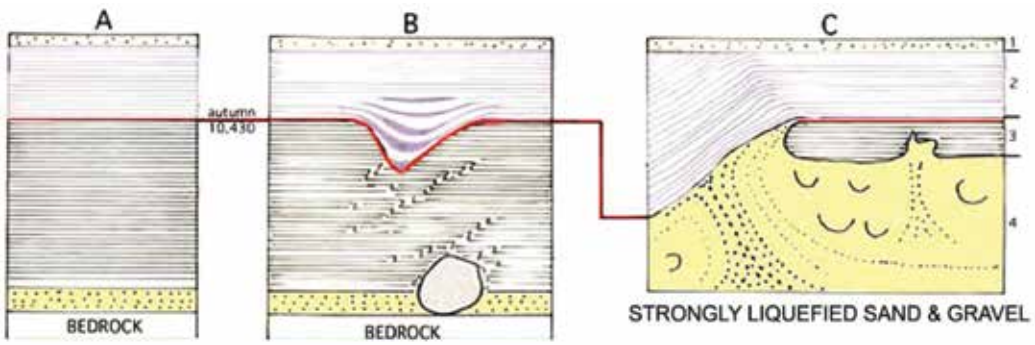

Figure 2. Three sections in the Turinge area exhibiting: (1) regressional sand and gravel, (2) varved clay deposited in marine-brackish environment, (3) varved clay deposited under fresh water conditions and (4) glacifluvial sand and gravel, strongly liquefied and with a subvertical venting pipe [1]. Section A shows a concordant change from freshwater to marine conditions in varve 10,430 BP. Section B shows an erosional contact in the autumn of varve 10,430 BP. Section C shows heavy liquefaction with a venting pipe mushrooming in varve 10,430 BP. This is indicative of a major earthquake event in the autumn of varve 10,430 BP, and a major tsunami event that washed the Närke Straight free of blocking pack ice and icebergs and opened the straight for ingression of marine water, turning the Baltic into the Yoldia Sea stage [1, 3, 4, 8]. The dating to the autumn of varve 10,430 BP is obtained at three sited 85 km apart [4, 9].

The earthquake in the autumn of varve 10,430 BP was exceptionally large with an estimated magnitude well above M 8 [1, 2, 4, 9]. It is recorded by multiple criteria (**Figure 3**).

Figure 3. The 10,430 BP paleoseismic event is documented by multiple criteria [1, 2, 4, 9].

The tsunami event linked to this earthquake must have been both strong and high because it flushed the Närke Straight totally open allowing marine water into the Baltic in the varve-year 10,430 BP. At the same time, several lake basins were invaded [1]. The total height of the tsunami wave is estimated at 15–20 m (**Figures 1** and **3**). The event is likely to have set up a sequence of six waves, judging from multiple graded bedding cycles as illustrated in **Figure 4** in view of [4, 9].

http://dx.doi.org/10.5772/63956

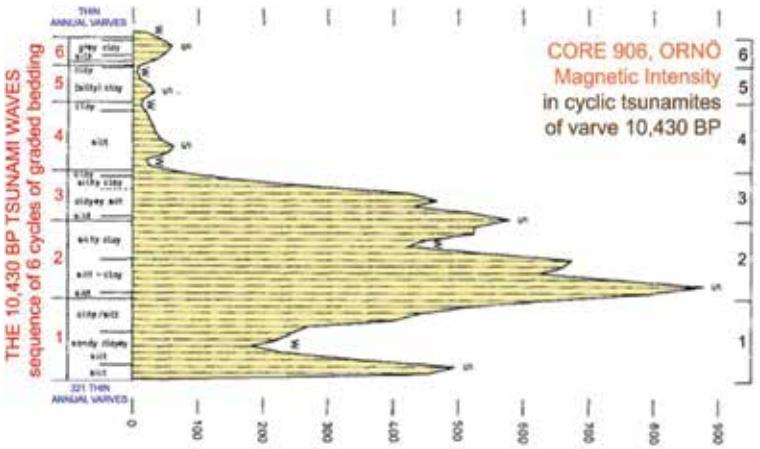

Figure 4. A segment of an 11 m core taken on the island of Ornö, some 30 km south of Stockholm [13]. After 321 years of deposition of normal annual varved clay, the sequence is broken by a sequence of six thick beds of graded bedding (1–6), interpreted to represent a sequence of six major tsunami waves of the 10,430 BP major earthquake and tsunami event [1–4]. Paleomagnetic intensity shows a high peak representing "the Gålö Geomagnetic Intensity Peak," known to have occurred in varve 10,430 BP [14]. The intensity curve records six cycles of stronger (s) and weaker (w) magnetization [15]. The six beds of cyclic sedimentary (and magnetization) deposition represent a bed load, deposited at a water depth of about 130 m, as a hydride between tsunamites and turbidites [3, 4].

Varve 10,430 BP is recorded in numerous cores and sections in southern Sweden. It is characterized by a simultaneous change from freshwater to marine environmental conditions, but also as a thick sandy-gravelly varve including rounded clay "pebbles" from the erosion of older clay beds, i.e., a layer transported under strong forces over the old seabed in the form of a turbidite. This turbidite varve has been recorded over an area of 200 × 320 km (**Figure 3**). In a few sites, it is seen as a sequence of cyclic deposits (**Figure 4**) representing a tsunamite deposited by a sequence of tsunami waves. This called for a new model where the tsunami wave forces and the seabed turbidite transport could be understood in terms of an integrated mode of transport, erosion and deposition [3, 4]. **Figure 5** presents this integrated model (first presented in [3]).

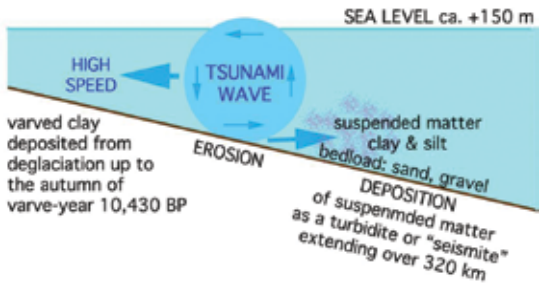

Figure 5. Integrated model [3, 4] for the tsunamite/seismite deposition in varve 10,430 BP. The tsunami wave has a large diameter and soon starts to trim the surface of the seabed setting up clay and silt in suspension and bed load of sand and gravel transported as a turbidite. At the time of the earthquake and tsunami event, sea level was about 150 m high than today in the Stockholm region. From [3].

Varve 10,430 BP was originally interpreted in terms of a "drainage varve" [16], an old idea now substituted by the recording of the huge earthquake in varve 10,430 BP and its extensive tsunami event [1, 3, 4]. The spatial distribution is given in **Figures 6** and **7**.

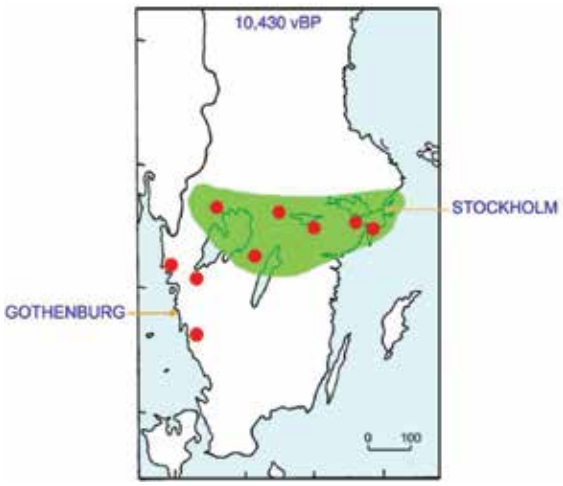

Figure 6. Red dots represent sites of recorded tsunamites. Green field represents the spatial distribution of firmly varve-dated tsunamites, seismites and liquefaction features with sites outside this field referring to sites dated by other means.

Figure 7. Paleogeography of the land–sea–ice distribution at the time of the big earthquake in varve-year 10,430 BP (modified from [3]). Red dot marks location of epicentre. Red double arrows refer to the Närke Straight opened by the tsunami wave so that marine water could enter the Baltic and turn it into the Yoldia Sea stage. Red cross marks the location of two sites recording an earthquake event with liquefaction and a tsunami event occurring 67 varves after deglaciation [17].

http://dx.doi.org/10.5772/63956

2.2. The 9663 BP event

In the Hudiksvall area of central Sweden, there occurred a very large earthquake in the varve-year 9663 BP [1, 3, 4, 9, 12, 18, 19]. The paleogeography of this event is very well known (**Figure 9**). Sea level was in the order of +224–230 m, and only minor islands stack out of the sea in front of the ice margin. It is recorded by multiple criteria [1, 4, 9] as illustrated in **Figure 8**. It seems to represent one of the best documented paleoseismic events in the world [1, 2]. The intensity was estimated at XII and the magnitude as >8 [2, 9]. Bedrock fracturing is recorded in some 100 sites over an area of 50 × 50 km. Liquefaction is recorded at 12 separate sites covering an area of 80 × 40 km. At two sites, it is recorded in five separate phases thought to represent the main event and a sequence of aftershocks. The liquefaction event is directly tied to varve 9663 BP. The water depth at the epicentre is likely to have been in the order of 250 m (allowing for a tsunami wave with the same diameter). A tsunami wave is recorded at 14 different sites, including nine lakes where a total of 44 cores were taken. It is dated both by varves (at 9663 varve-years BP) and by radiocarbon (at about 9150 C14-years BP). The tsunami wave must have a height of at least 15 m [1, 3, 4, 9]. A turbidite in varve 9663 BP extends for 310 km along the coast [1, 19].

Figure 8. The 9663 BP paleoseismic event must have had a magnitude of $M > 8$. It is documented by multiple criteria [1, 3, 4, 9, 18].

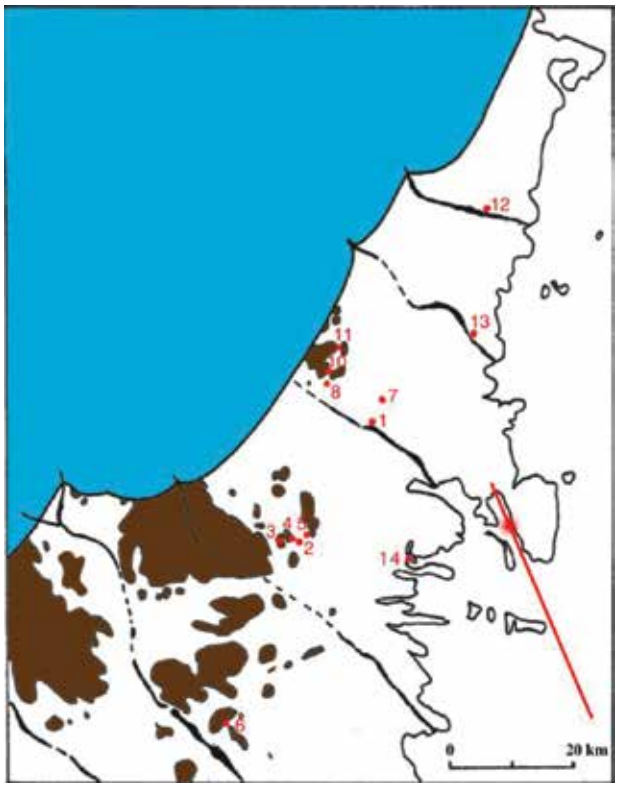

Figure 9. Paleogeography of the Hudiksvall area at the high-magnitude earthquake in the varve-year 9663 BP (or ~9150 C14-years BP). Explanations: blue: extension of the ice cap; brown: land areas; black winding strings: eskers; red line with dot: fault line and location of epicentre; red dots with numbers 1–14: sites where tsunamites of the 9663 BP event have been documented (from [1]).

Figure 9 provides the paleogeography of the area in the varve-year 9663 BP and the location of the 14 sites where records of the tsunami event have been recorded in the near-field region [1]. The area is traversed by six separate drainage basins marked by the corresponding esker systems from the subglacial drainage. The turbidite of varve 9663 BP traverses the entire area and expands 310 km to the south.

The tsunami was probably composed of two to three waves judging from the cycles recorded (**Figure 10**). Site 2 (Lake Svartsjön) is the key site of 14 closely spaced cores, five C14-dates and diatom analysis [1, 3]. The site was deglaciated 25 years before the tsunami event. The highest coastline (HK in **Figure 10**) was closely determined at +31.3 m. At the time of the tsunami event, the Baltic level had fallen to +223.5 m, i.e., a drop of about 7.8 m in 25 years, providing a rate of relative uplift of about 312 mm/year. The five C14-dates all overlap at 9155-9135 C14-years BP. A C14-age of 9150 BP would correspond to an absolute age of 10,350 cal. years BP. The deviation between the absolute age and the varve age of 9663 BP records an error in the varve chronology of about 700 years [20].

http://dx.doi.org/10.5772/63956

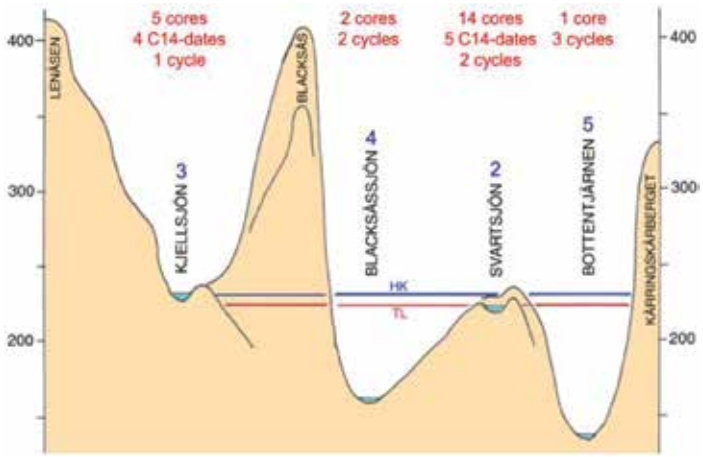

Figure 10. A 5.5 km SW–NE profile of the topographic setting of sites 2–5 (from [1]).

Figure 11 provides a good and representative record of the stratigraphy and sequence of events in Lake Svartsjön (Site 2). After the deposition of 25 varves, a tsunami wave invades the lake basin by overflowing the sill to the east (about +228 m) and depositing a thick tsunamite spread over the entire lake basin. This calls for a minimum height of the tsunami wave of 6 m (cf. 15 m at Site 3).

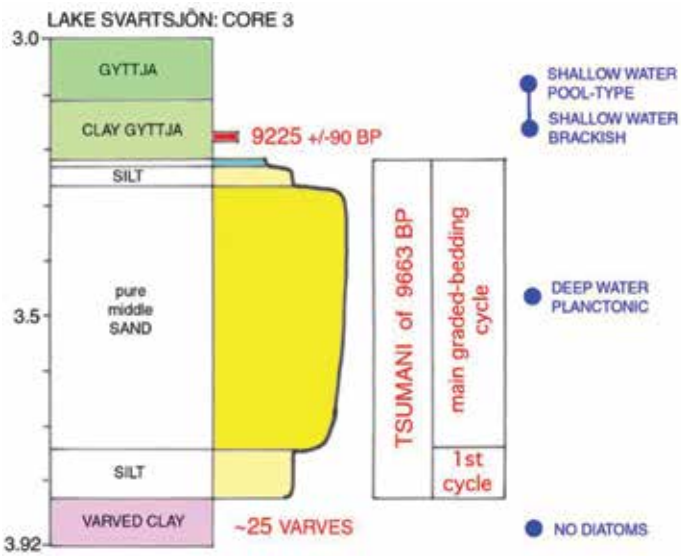

Figure 11. Stratigraphy, dates, tsunami characteristics and diatom analyses of Core 3 in Site 2 [1, 3]. The tsunamites spans 60 cm and is composed of a fragmentary first cycle and a full main cycle of graded bedding fining upward (sand-silt-clay). The diatom content of the tsunamite represents a planktonic deep-water flora of the open Baltic Lake Ancylus stage [3].

The tsunamite has a thickness 50–60 cm and is composed of two (occasionally 3) depositional cycles of graded bedding. The diatom flora of the tsunamite represents planktonic deep-water species from the open Baltic environment of the Ancylus Lake stage. This is a useful characteristic of sandy beds deposited by tsunami waves from the sea (contrary to shallow-water beach erosion).

The Lake Källsjön records are important [1]. This lake was never a part of the Baltic. The sill in-between had an original level of about +236 m [3] (**Figure 12**). Five cores were obtained in the lake, all including a typical tsunamite of graded bedding, indicating a forceful overflow of the sill and ingression into the lake of the 9663 BP tsunami wave. The wave must be at least 12.5 m high and overflow the sill for 700 m. Therefore, we can set the tsunami height at 13 m or rather about 15 m. The full evidence of a major tsunami event comes from the content of diatoms in the tsunamite beds, viz., a typical planktonic diatom flora of the Baltic Lake Ancylus stage [1, 3]. Furthermore, in today's lake, a small fish, smelt, is living, which is considered to be a relict from the Lake Ancylus stage of the Baltic, washed into the lake by the 9663 BP tsunami wave.

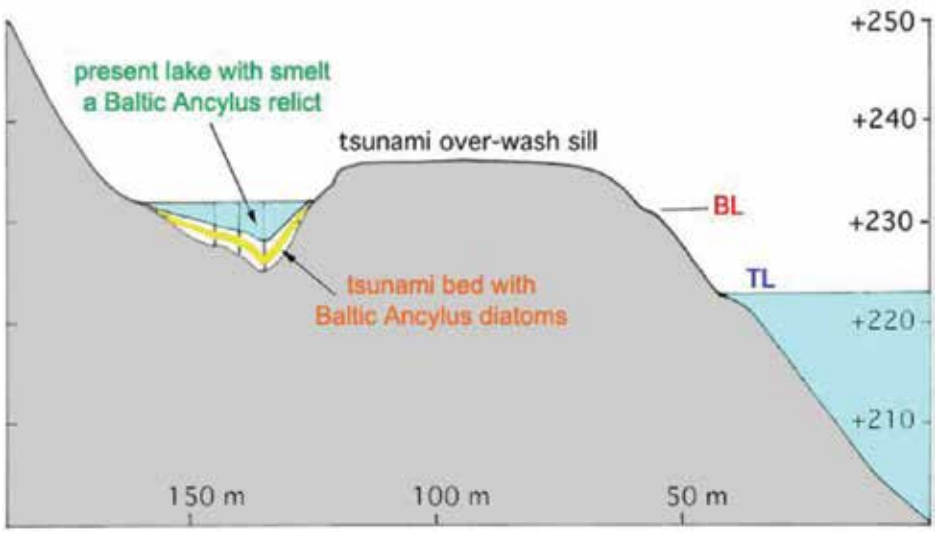

Figure 12. Site 3, Lake Kjällsjön, was never a part of the Baltic because it was located above the highest Baltic limit (BL) and separated from it by a sill [1, 3]. At the 9663 BP event, the sill was overwashed and the lake was invaded by a wave from the Baltic. The tsunami height must have been at least 13 m, probably about 15 m high. From [3].

A final example of the 9663 BP tsunami comes from the harbour of Iggesund (site 14 in **Figure 9**), where we had five pits and a major trench cut [1, 4]. The area was free-melted in 9747 BP. Then, followed the deposition on 84 annual varves. In varve-year 9663 BP, the area was affected by a strong earthquake. The glacifluvial sand and silt was heavily liquefied, and the liquefied material vented to the surface where it spread laterally by mushrooming. Some lateral spreading also occurred along the surfaces of varve beddings. In pits 4 and 5, the intra-clay sand layer had the character of a tsunami bed. In pit 4, we brushed off the sand covering

http://dx.doi.org/10.5772/63956

the clay surface beneath. The surface exposed was traversed by furrows and wave patterns (**Figure 13b**) indicating that the tsunamites must have been deposited by a flow from the NE, which implied from the sea towards the coast. At that stage, we had not yet located the epicentre of the paleoseismic event. Later it was determined that the epicentre of the 9663 BP event must have been located 12 km to the NE (as marked in **Figure 9**). Consequently, our sedimentary records in the pits at Iggesund (**Figure 13**) are in full agreement with this location of the epicentre.

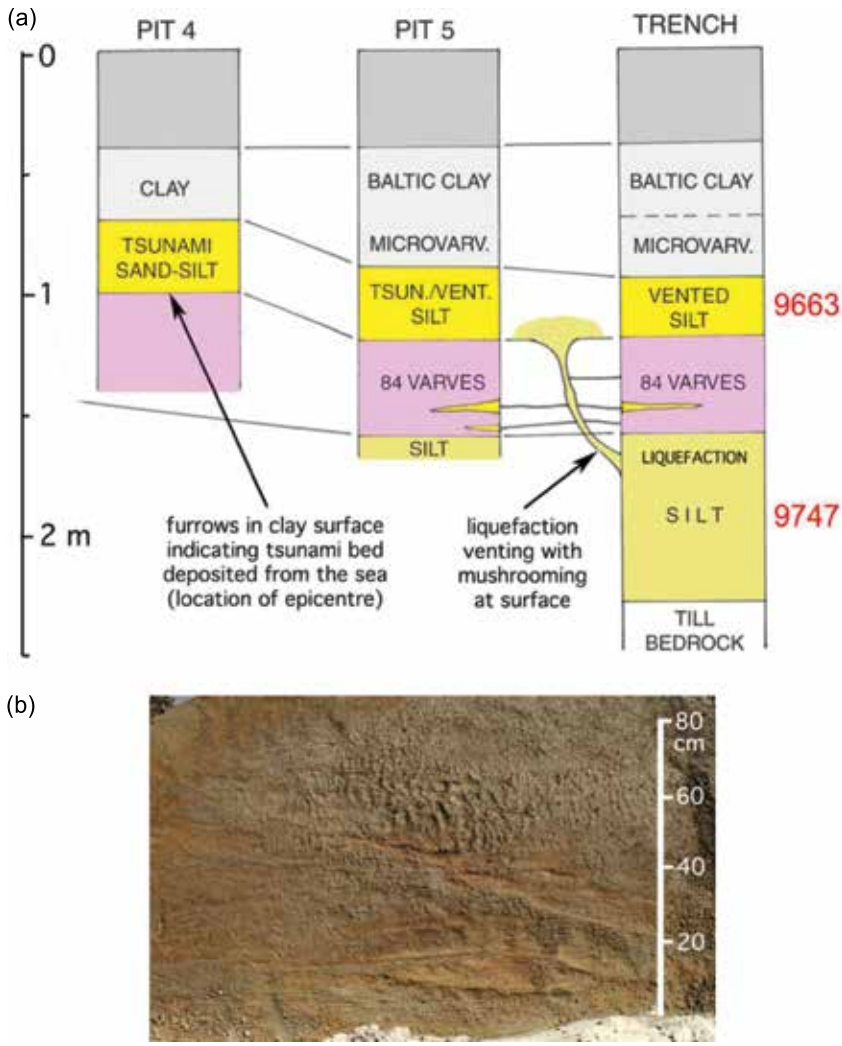

Figure 13. Stratigraphic records at site 14, Iggesund harbour [1, 4] recording liquefaction, venting and surface mushrooming of liquefied material, and the deposition of a tsunamite. The clay surface beneath the tsunamite in pit 4 is irregular (furrows and waves) in a manner indicative of a deposition from the NE (from right to left), i.e. from the sea outside.

Figure 14 provides the spatial distribution of the 9663 BP tsunami event in Sweden. The extension of this tsunami even will surely expand considerably with time to sites in Finland, Sweden and the Baltic coast to the SE, where there are numerous sites of proposed transgression deposits of the Ancylus Lake dated at the same age as the tsunami. Most probably, several of these sites must be reinterpreted in terms of tsunamites [1].

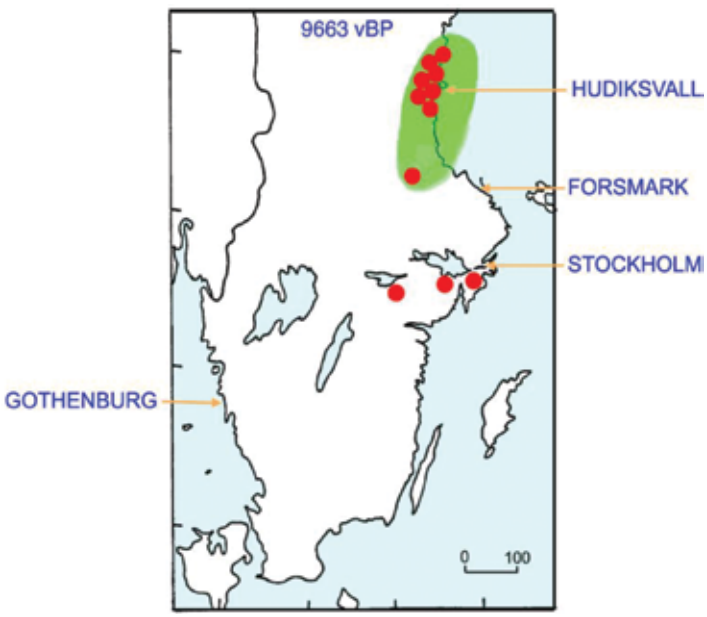

Figure 14. Red dots represent sites of recorded tsunamites. Green field represents the spatial distribution of firmly varve-dated tsunamites (also seismites and liquefaction features) with sites outside this field referring to sites dated by other means.

2.3. The Late Holocene events

The 17 tsunami events recorded in Sweden over the last 13,000 years (**Figure 1**, **Table 1**) are fairly regularly distributed over time. In the past 4000 years, there were as many as seven events observed [3, 21, 22], three of those are discussed below.

This includes a revision of the previously assigned age of the Hudiksvall event; now re-dated at 2900 BP, instead of 2000 BP. This makes the two events synchronous though recorded 160 km apart.

2.4. The 2900 BP event recorded at two sites 160 km apart

Site 1 refers to a well recorded at Skålbo, north of Hudiksvall [1, 3, 22, 23]. Here, violent methane-venting tectonics set up a tsunami wave recorded in five bogs at +8, +14, +18, +23 and +38 m [1, 3, 9, 22]. Lake Dellen, 25 km to the west and today at +37 m has a submerged peat dated at about 2000 BP [3]. This age was used to determine the age of the event. At 2000 BP,

http://dx.doi.org/10.5772/63956

sea level was at +18 m, implying a wave height of 20 m [1]. Consequently, the run-up must have been at least 20 m in order to invade the +38 m bog.

Later, I come to question the age determination, however. First, the Lake Dellen pounding may have nothing to do with the tsunami event. Second, we find no records of the 2900 BP event in the Hudiksvall lakes and no records of the 2000 BP event in the Forsmark lakes. Third, subsequent C14-dates of the lake deposits provide ages older than 2000 BP.

Now, it seems quite clear that the Hudiksvall event should be synchronized [23] with the Forsmark tsunami event closely dated at 2900 BP.

At 2900 BP, sea level in the Hudiksvall area would have been at +26 m [23]. This implies a tsunami height of at least 12 m (to deposit a tsunamite in the +38 m bog). The tsunami wave had a trimming effect of the seabed (i.e., erosion) down to at least +8 or 18 m below sea level at that time.

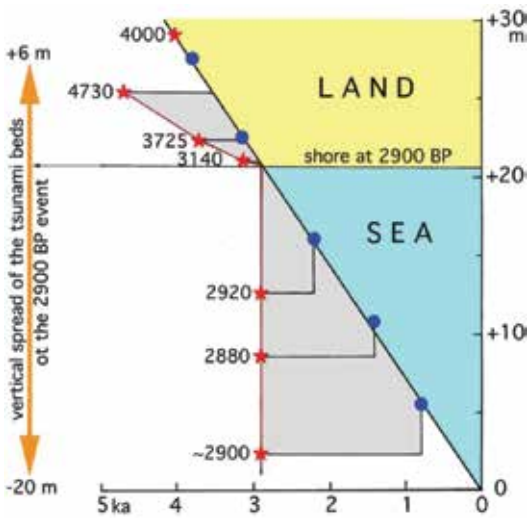

Figure 15. The 2900 C14-years BP tsunami event in northern Uppland with respect to the rate of land uplift and shore displacement over the last 4000 years (the oblique line of ~7 m uplift per millennia passing through dated anchor points marked by blue dots). At 2900 C14-years BP, the shore was at +20.7 m with land above (yellow) and sea (blue) below as marked on the right side of the diagram. The stars mark tsunami beds recorded and dated in offshore sediments (all falling sharply at the 2900 BP level), in coastal deposits and in lakes and bogs on land where the tsunami beds have eroded down into the older sediments. The graph provides evidence of a tsunami event that deposited typical tsunami beds over a vertical range from −20 to +6 m.

The Forsmark event (**Figure 15**) refers to a tsunami event very closely C14-dated at 2900 BP, which was recorded in seven lakebeds in northern Uppland, 160 km to the south of the Hudiksvall records [3, 9, 22]. The lakes investigated and dated form a staircase in elevation, viz., +5.5, +10.8, +16.0, +16.0, +22.2, +22.5 and +24.7 m. At the time of the tsunami event, sea level was at +20.7 m, implying that four lakes were located below and three above sea level at 2900 BP (**Figure 15**). In all the lakebeds, we found nice tsunamites of sandy layers in graded

bedding. A lakebed at +27.4 m [24] shows no sign of a tsunami ingression. Therefore, the upper limit of the tsunami event is set at about 26.5 m, indicating a tsunami height in the order of 6 m (and a submarine trimming depth of about 20 m).

Several lakes and bogs in the region had been investigated before [24–26], but none of those studies recorded the occurrence of tsunamites despite the fact that they are quite clearly present in the lakes at +5.5, +10.8, +16.0 and +22.5 m [26], all later cored and dated by the author, as shown in **Figure 15**.

Synchronizing the events recorded at Skålbo and Forsmark (**Figure 16**) implies a fall in tsunami height of 6 m over a distance of 160 km, which seems quite reasonable.

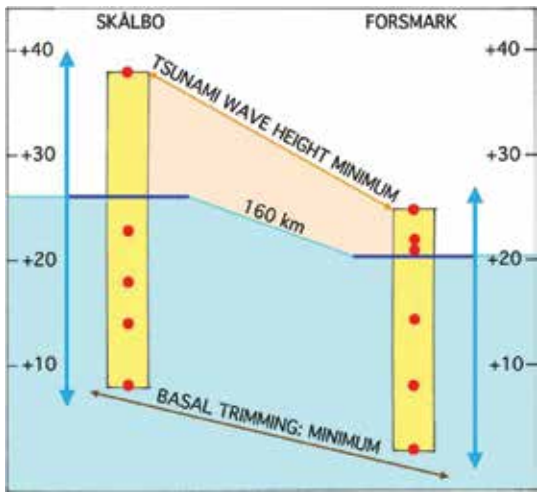

Figure 16. Synchronization of the tsunami events recorded at Skålbo (Hudiksvall) and at Forsmark (northern Uppland) at 2900 BP [23]; elevation of dated cores (red dots), sea level at 2900 BP (dark blue lines). The tsunami wave height of at least 12 m in Skålbo decreases to at least 6 m in Forsmark, i.e., a decrease of 6 m in 160 km. The basal trimming seems to go down at least 18 m below sea level.

2.5. The AD 1174 event

In SW Sweden, there are evidence of a young paleoseismic event with local faulting of the Viking shoreline. This implies a faulting post-dating the formation of this shoreline, known as PTM-10, and dated at 1000-950 BP [1, 22, 27]. A fault offset of 1.1 m is recorded [1, 22].

It seems highly likely that this earthquake also set up a tsunami wave, which buried two Viking ships in the ancient harbour of Galtabäck [27]. A C14-date of the ship gave 1172 ±73 cal. years AD [28], which is quite close to a major historical earthquake event in 1174 as recorded in chronicles [29]. The covering and burying of the two ships in silt are indicative of a very rapid (instantaneous) process that took the ship owners by surprise, fully in line with the process of a tsunami event.

http://dx.doi.org/10.5772/63956

Therefore, it was proposed [27] that, indeed, the earthquake set up a tsunami and that the event refers to the earthquake in 1174 mentioned in the chronicles [29], which corresponds to 776 cal. years BP.

Having established this, it is possible to re-evaluate a turbidite record from the Gullmar Fjord [30] 230 km to the NW in terms of a tsunamite (**Figure 17**).

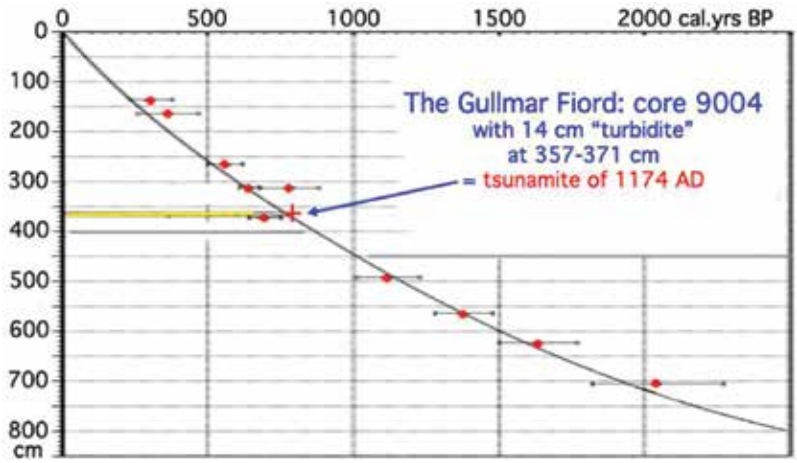

Figure 17. The time/depth relations of core 9004 [30] and the position of the "turbidite" here revised in terms of a tsunamite of the 1174 AD earthquake event.

An inferred age of the "turbidite" in the Gullmar Fjord core of 1174 AD fits perfectly well with the time/depth curve of [30]. I therefore, quite confidently, re-evaluate this layer as a tsunamite of the 1174 paleoseismic event [27].

3. Discussion

With a total of 17 separate tsunami events documented in Sweden after the Last Ice Age [1–4, 21], Sweden is a country of exceptionally high number of tsunami events. This is due to the fact that it represents an uplifted shelf environment [5] with sedimentary sequences—not least the varved clay—exposed on land where tsunami events can be documented in details and where their age can be determined with high precision [4].

It is most surprising that tsunamis have not yet been reported by other geologists in Sweden, Finland and Denmark, especially after the first report was brought out in 1995 [10] and 1996 [11]. The evidence is there in the field, just to observe, interpret and document.

In Norway, there are excellent records of the tsunami from the gigantic Storegga submarine slide [31, 32].

4. Conclusions

Tsunami events with the deposition of tsunamites are well recorded in Sweden [1, 2, 3, 4]. Up to today, 17 events have been documented and described (**Table 1** and **Figure 1**). The triggering factor was high-magnitude paleoseismic events ranging from ~13,000 BP to ~800 BP. In two cases, however, the triggering factor was a violent methane-venting episode [1–3, 23]. **Figure 1** summarizes the estimated tsunami heights: 6 of 1–5 m, 5 of 6–10 m, 5 of 11–15 m and 1 of 16–20 m.

The absence of recognition of tsunami events in Sweden by other scientists seems to be routed both in personal ignorance and in pressure from the nuclear power industry, which has chosen to neglect evidence of high seismic activity that might invalidate their claim of a safe deposition of the high-level nuclear waste in the bedrock. A safety analysis ignoring observational fact [33] can, of course, never be trustworthy as shown in a devastating manner by screening available field evidence in a long-term safety perspective [2].

A generally high paleoseismic activity during the deglacial phase of Sweden, a number of Late Holocene events reaching magnitudes of $M\sim 7$ and a sequence of 17 tsunami events are facts that must be assimilated in the history of Quaternary geology of Sweden [34] like in the long-term safety of a nuclear waste storage in the bedrock [2, 35].

Acknowledgements

This chapter is an update and revision of the author's paper in the previous tsunami book, *The Tsunami Threat —Research and Technology*, N.-A. Mörner, ed., InTech, 2011, of InTech. The author declares no conflict of interest.

Author details

Nils-Axel Mörner

Address all correspondence to: morner@pog.nu

Paleogeophysics and Geodynamics, Stockholm, Sweden

References

[1] Mörner, N.-A. *Paleoseismicity of Sweden—A Novel Paradigm*. A Contribution to INQUA from Its Sub-Commission on Paleoseismology at the 16th International INQUA Congress in Reno, Nevada, P&G print; 2003, 320 pp.

[2] Mörner, N.-A. Patterns in Seismology and Palaeoseismology, and Their Application in Long-Term Hazard Assessments —The Swedish Case in View of Nuclear Waste Management. Pattern Recognition in Physics, 2013; 1: 75–89. doi:10.5194/prp-1-75-2013

[3] Mörner, N.-A., Dawson, S. Traces of tsunami events in off- and on-shore environments. Case studies in the Maldives, Scotland and Sweden. In: N.-A. Mörner, editor, The Tsunami Threat—Research and Technology. InTech, 2011, Chapter 18, pp. 371–388.

[4] Mörner, N.-A. Drainage varves, seismites and tsunamites in the Swedish Varve Chronology. GFF, 2013; 135: 308–315.

[5] Mörner, N.-A. Paleoseismics in an uplifted, former shelf, area. In: Abstracts of IGCP-526 Meeting in Rabat 2009.

[6] Mörner, N.-A. Tsunamis and tsunamites: origin and characteristics. In: Proceedings of the 4th International INQUA Meeting on Paleoseismology, Active Tectonics and Archeoseismology (PATA), 9–14 October 2013, Aachen, Germany, 2013, 165–168.

[7] Brunnberg, L. Clay-varve chronology and deglaciation during the Younger Dryas and Preboreal in the easternmost part of the Middle Swedish ice marginal zone. Ph.D. thesis. Quaternary Geology, Stockholm University.

[8] Mörner, N.-A. The Baltic Ice Lake —Yoldia Sea transition. Quaternary International, 1995; 27: 95–98

[9] Mörner, N.-A. Paleoseismology: The application of multiple parameters in four case studies in Sweden. Quaternary International, 2011; 242: 65–75.

[10] Mörner, N.-A. Geologisk sensation. Jättejordbävning skakade Märardalen för 10.476 år sedan. Forskning och Framsteg, 1996; 5: 30–33.

[11] Mörner, N.-A. Liquefaction and varve disturbance as evidence of paleoseismic events and tsunami: the autumn 10,430 BP event in Sweden. Quaternary Science Review, 1996; 15: 939–948.

[12] Mörner, N.-A. Paleo-tsunamis in Sweden. Physics and Chemistry of the Earth, 1999; 24: 443–448.

[13] Mörner, N.-A. Paleoseismicity and geodynamics in Sweden. Tectonophysics, 1985; 117: 139–153.

[14] Mörner, N.-A. Additional information obtained after the 1973 report. Boreas, 1976; 5: 261–271. In: Mörner, N.-A., editor, The Pleistocene/Holocene boundary: a proposed boundary-stratotype in Gothenburg, Sweden. Boreas, 1976; 5: 193–275.

[15] Mörner, N.-A. and Sun, G. Paleoearthquake deformations recorded by magnetic variables. Earth and Planetary Science Letters, 2008; 267: 495–502.

[16] De Geer, G. Geochronologia Suecia Principles. Kungliga Svenska Vetenskapsakademiens Handlingar, 1940; 18 (6): 1–360.

[17] Mörner, N.-A. Seismotektoniska grottor i Finland. Grottan, 2010; 4: 6–14.

[18] Mörner, N.-A., Tröften, P. E., Sjöberg, R., Grant, D., Dawson, S., Bronge, C., Kvamsdal, O., Sidén, A. Deglacial paleoseismicity in Sweden: the 9663 BP Iggesund event. Quaternary Science Reviews, 2000; 19: 1461–1468.

[19] Mörner, N.-A. Paleoseismicity and Uplift of Sweden, Guidebook, Excursion 11 at 33rd IGC, Oslo 2008, 107 pp. www.33IGC.org.

[20] Mörner, N.-A. Varve Chronology. In: N.-A. Mörner, editor, Geochronology: Methods and Case Studies. InTech, 2011, Chapter 3, pp. 73–87.

[21] Mörner, N.-A. Tsunami events within the Baltic. In: Proceedings of the workshop "Relative sea level changes—from subsiding to uplifting coasts," Gedansk, 2005, Polish Geological Institute Special Papers, 2008; 23: 71–76.

[22] Mörner, N.-A. Late Holocene earthquake geology in Sweden. Geological Society in London, Spec. Publ., 2009; 316: 179–188.

[23] Mörner, N.-A. Methane ice in crystalline bedrock and explosive methane venting tectonics. Manuscript, 2016, under review.

[24] Bergström, H., Late Holocene distribution of lake sediment and peat in NE Uppland, Sweden. SKB, 2001; R-01–R12: 1–50.

[25] Robertsson, A.-M., Persson, C. Biostratigraphical studies of three mires in northern Uppland, Sweden. Sveriges Geologiska Undersökningar, 1989; C821: 1–18.

[26] Hedenström, A., Risberg, J. Shore displacement in northern Uppland during the last 6500 years. SKB in [24, 26, 33] stands for Swedish Nuclear Safety Ltd, 2003; TR-03-17: 1–48.

[27] Mörner, N.-A. An M>6 earthquake ~750 BC in SE Sweden. Open Journal of Earthquake Research, 2014; 3: 66–81.

[28] Mörner, N.-A. The Late Quaternary History of the Kattegatt Sea and the Swedish West Coast: Deglaciation, Shorelevel Displacement, Chronology, Isostasy and Eustasy. Sveriges Geologiska Undersökning, 1969; C-640: 1–487.

[29] Svedmark, E. Jordskalf i Sverige 1904-1906. P.A. Nordstedt & Söner, 1908, Stockholm, 124 pp.

[30] Harland, R., Polovodova Asteman, I., Norberg, K. A two-millennium dinoflagellate cyst record from Gullmar Fjord, a Swedish Skagerack sill fjord. Palaeogeography, Palaeoclimatology, Palaeoecology, 2013; 392: 247–260.

[31] Bondevik, S., Svensen, J.I., Mangerud, J. Tsunami sedimentary facies deposited by the Storegga tsunami in shallow marine basins and coastal lakes, western Norway. Sedimentology, 1997; 44: 1115–1131.

http://dx.doi.org/10.5772/63956

[32] Vasskog, K., Waldmann, N., Bondevik, S., Nesje, A., Charpron, E., Ariztegui, D. Evidence for Storegga tsunami run-up at the head of Nordfjorden, western Norway. Journal Quaternary Science, 2013; 28: 391–402.

[33] Hedin, A. (project leader), Preliminary safety evaluation for the Forsmark area. SKB, 2005; TR-05-16: 1–105.

[34] Mörner, N.-A. Paleoseismics and general Quaternary geology of Sweden. New aspects in the light of the novel concept of a high deglacial seismicity. In [1], Chapter 14, 313–318.

[35] Mörner, N.-A., Nuclear power and radioactive contamination. Journal of Environmental Protection, 2014; 5: 175–180.

Chapter 7

Challenges and Opportunities for Reducing Losses to Fast-Arriving Tsunamis in Remote Villages Along the Coast of Pakistan

Ghazala Naeem, Abdullah Usman and
Jamila Nawaz

Additional information is available at the end of the chapter

http://dx.doi.org/10.5772/64897

Abstract

Fishing villages in coastal Pakistan would need to respond quickly to escape a tsunami from nearby parts of the Makran Subduction Zone. A previous Makran tsunami, in 1945, took hundreds of lives in this coastal area. The majority of those fatalities took place along tidal creeks of the Indus Delta, where the parent earthquake was scarcely felt. Today, many of the Delta villages must be reached by boat, and telecommunication is difficult. These circumstances add to the challenge of their receiving timely warning of an incoming tsunami—whether it is the immediate natural warning from a felt earthquake or a subsequent official warning from government agencies. A study supported by Oxfam GB underscores this challenge. Ten remote coastal villages, each visited by the study team, were found to have limited links to official warning systems through landlines, mobile phones, and the Internet. Two cities, by contrast, have International Maritime Satellite Organization sirens that can be set off by satellite. In addition to technological solutions, partial remedies currently available include improved tsunami awareness, training about natural warnings, and land use informed by hazard assessments.

Keywords: coastal hazards, tsunami early warning, Pakistan, dissemination mechanism

1. Introduction

Recent events of cyclone (Gonu 2007 and Phet 2010) and tsunamis of Indonesia in 2004 and Japan in 2011 were the wakeup call for the scientific community and for developers, planners, and decision makers to prepare for a worst case scenario. Moreover, as a result of unplanned urban growth, negligence of construction standards, localized concentration of population and infrastructure, and the lack of awareness at the public and the institutional levels, coastal cities of developing countries are more vulnerable to the adverse effects of seismic hazards including tsunamis. Despite the tsunami's complex nature, its potential to create massive damage is compelling. Along coastal belt of Pakistan, many small fishing villages still lacking in basic communication infrastructure are extremely vulnerable to coastal hazards when personal notification is the only way of evacuation warnings. Most of these villages do not have landlines, electricity, roads, and mobile phone networks (**Figure 1**). Local conditions do not facilitate for any safe evacuation site nearby; details are discussed in Section 3.3.

Figure 1. View of Sonth Village, UC Basool, Tehsil Ormara, District Gwadar, Balochistan Province.

Historical evidence for tsunami along the shores of the Arabian Sea (Northern Indian Ocean) is rare and in cases contradicting. Out of several historical events the 1945 Makran earthquake is the only instrumentally recorded one that generated a tsunami. Therefore, the 1945 event serves as the basis for modeling approaches in early tsunami warning system which is currently being set up in Pakistan [1] (**Figure 2**).

National Tsunami and Cyclone Warning Center established at Pakistan Meteorological Department (PMD) [2] is being set up to watch, investigate, and warn about tsunami and cyclone threats to Pakistan coastline. The PMD established tsunami warning standard

http://dx.doi.org/10.5772/64897

operating procedures (SoPs) in 2010 [3] and has categorized tsunamis in different types based on the size and location of the parent earthquake.

A regional or local tsunami such as the one created in Arabian Sea in 1945 [3] might be more destructive for Pakistan's coastal belt than the one located farther in the Indian Ocean. Therefore, a dissemination of warning for local tsunami should be issued to the communities within 7–10 min of its origin, and usually, a possible threat of tsunami is proposed for an earthquake of magnitude 7.5 and above. A tsunami in the Indian Ocean might take as long as 10–13 h to reach and affect Pakistan's coastal areas. Henceforth, a warning for tsunami (as a possible threat) in this case is issued only if the earthquake magnitude lies within the ranges of 7.0 and above.

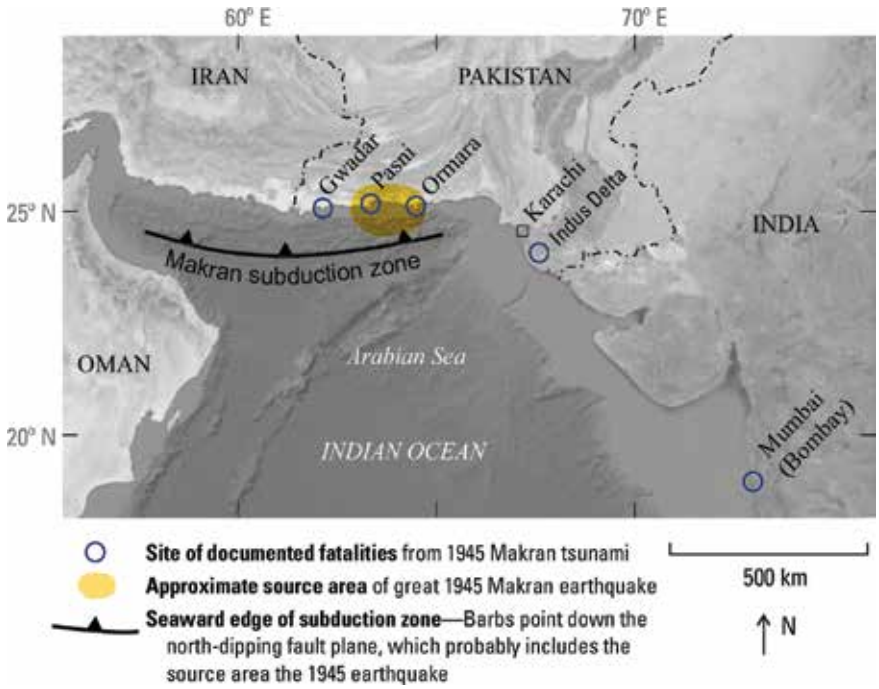

Figure 2. Makran and Indus Delta Creek region affected by 1945 Tsunami also covers communities studied.

This chapter analyzes the gaps in coastal hazard early warning system (EWS), specifically pertaining to dissemination of information along the coastal belt of Pakistan. Although EWS comprises of two components: (a) detection of threat and (b) subsequent relay of information, the chapter only focuses on the later.

This study sheds light on the challenges related to dissemination of early warnings of coastal hazards in Pakistan. It provides a comprehensive overview of the current arrangement for broadcasting a warning and limitations of the system (with references to sampled villages). The chapter also provides recommendations for division of responsibility and improvement of the system.

2. Methods

The study methods included desk review of the available documents and data on the subject, collection and analysis of primary and secondary sources data, and direct field observations as well as interviews with community's representatives and concerned personnel. All such information was finally summarized and put for analysis to identify issues and gaps, and to develop recommendations on effective early warning to coastal communities of Pakistan.

2.1. Primary data collection

Primary data collection is generally based on field survey comprising three main parts: (a) household interviews, (b) key informant interviews, and (c) focus group discussions.

The research team, led by the principal investigator, visited ten villages in Thatta, Sujawal, and Badin districts in Sindh and in the Gwadar district of Balochistan. The team was assisted by representatives of the communities for interpretation and to translate the questions and answers for both parties (**Figure 3**).

Figure 3. Discussion carried out with women at Sonth Village living at the bank of Basool River where it falls into sea.

2.1.1. Household interviews

A detailed questionnaires were designed for household interviews that focused primarily on the basic infrastructure related to early warning communication systems present in the communities, their efficacy in delivering information and warning the potential affectees in times of disaster (cyclones or tsunamis), and constraints or limitations observed in the operation of these early warning communication systems.

http://dx.doi.org/10.5772/64897

2.1.2. Key Informant interviews

For this part, the research team interviewed senior officials from various organizations namely WWF-Pakistan, Rural Community Development Council (RCDC) Gwadar, Trust for Conservation of Coastal Resources (TCCR) Sindh, Pakistan Meteorological Department, Pakistan Navy and the Government of Sindh. Their observations, suggestions, and recommendations pertaining to the gaps present in the currently employed early warning systems and consequently the required improvement have been incorporated in the chapter.

2.1.3. Focus group discussions

The questions concerning early warning system were mostly inquired from the middle- and old-aged men (mostly fishermen by occupation) and women of different households. A special emphasis was placed on the availability of various communication systems in the community and used at the household level. An additional content of the investigation involved recording oral histories of the 1945 tsunami. For this purpose, the researchers especially asked senior members of the household to recount what they had observed or heard from their elders witnessed the 1945 tsunami (**Figure 4**).

Figure 4. Focus Group Discussion at Tayyab Jatt village including interviewing eyewitness of 1945 Tsunami.

2.1.4. Compilation and analysis

The data set collected from site visits, key informant interviews, and focus group discussions was compiled in the form of report and was analyzed to draw conclusion on the present situation and provide recommendations for further steps needed to work on the elimination of gaps and limitations of the currently used early warning communication systems.

2.2. Secondary data collection

2.2.1. Desk review

A thorough desk-based review was conducted in order to carry out the project effectively. This comprises a literature review of reports drafted in the past that focuses on the same problem analysis, for example, Standard Operating Procedures of Tsunami Warning by National Seismic Monitoring and Tsunami Early Warning Centre Pakistan Meteorological Department 2010, Tsunami Risk Reduction for the Coastal Areas of Pakistan by National Disaster Management Authority, reports of UNDP's pioneer project on "Strengthening TEWS in Pakistan," UNESCO-IOC [5], Indian Ocean Tsunami Information Center (IOTIC) project website "1945 Makran Tsunami" and policy documents of government organizations to understand mission and objective of various stakeholders.

Data relating to the geography, topography, and demography of the target areas were collected from the Deputy Commissioner offices, WWF-Pakistan, Google imagery, and Survey of Pakistan's maps.

3. Current scenario

3.1. Institutional arrangement

The 2004 Indian Ocean tsunami and 2005 Kashmir earthquake prompted the Pakistani authorities to establish disaster management institutional arrangement and strengthening existing early warning system that could relay warning to those most at risk. Foregoing in view, in March 2010, the National Seismic Monitoring and Tsunami Early Warning Centre (NSM & TEWC) at Pakistan Meteorological Department (PMD) published Standard Operating Procedures (SOPs) for tsunami warning [4]. It identified PMD, disaster management authorities, and emergency responders as the key informants within the early warning communication chain that initiates from National Seismic Monitoring and Tsunami Early Warning Center (NSM & TEWS) at PMD and ends at the potential victims. This chapter assesses the institutional arrangements of each of the aforementioned authorities, especially in terms of capacity and limitations in two categories: Early Warning Dissemination Agencies and Emergency Responders.

3.1.1. Early warning dissemination agencies

3.1.1.1. Pakistan meteorological department

NSM & TEWC at PMD are adequately equipped to issue warnings depending upon National and Global Seismographic network's data on real-time basis to monitor seismic activity in order to locate potential tsunamigenic earthquakes. They are also connected with global centers such as Pacific Tsunami Warning Center (PTWC), Indian Ocean Tsunami Warning Centers (IOTWS), and Japan Meteorological Agency (JMA). PMD is also working on information sharing with

http://dx.doi.org/10.5772/64897

newly established tsunami early warning system at Oman for Arabian Sea. Once a warning is received, after initial assessment, PMD communicates a message to the district disaster management authorities.

PMD also has SOPs in place regarding the format of bulletin based on the category of threat, that is, time of issuance, level of threat, name of issuing agency, earthquake parameters (location, magnitude, and depth). These SoPs are the only time-based specific sequence of actions to be taken in case of potential tsunami threat among all stakeholders in Pakistan.

3.1.1.2. Information flow

PMD is acting as the key focal agency role. In case of tsunami all initial information flow will take place through PMD following timeline (**Figure 5**).

The information received to PMD about the possibility of a natural disaster such as tsunami, through national or international sources, is first conveyed to response agencies and national/provincial/district stakeholders within minutes, as per departmental SoPs.

a. NDMA

b. PDMAs (Balochistan and Sindh)

c. District Coordination Officers (DCOs) Karachi, Gwadar, Lasbela, Thatta, Sajawal, and Badin

d. Pakistan Army and Navy

e. an Coast Guards

f. Marine Security Agency

g. Karachi Port Trust

h. Gwadar Port Authority

PMD's usual modes of communication and dissemination of early warning information are:

a. Automated GPRS-based SMS

b. Mobile phone-based SMS (backup)

c. Automated Fax-2 Channel

d. Manual Fax-1 Channel

e. Satellite Phone (limited recipients)

f. Website updating www.pakmet.com.pk/ and email

In addition to the above-mentioned resources, PMD recently acquired mass notification system installed at Gwadar and Pasni cities connected via satellite.

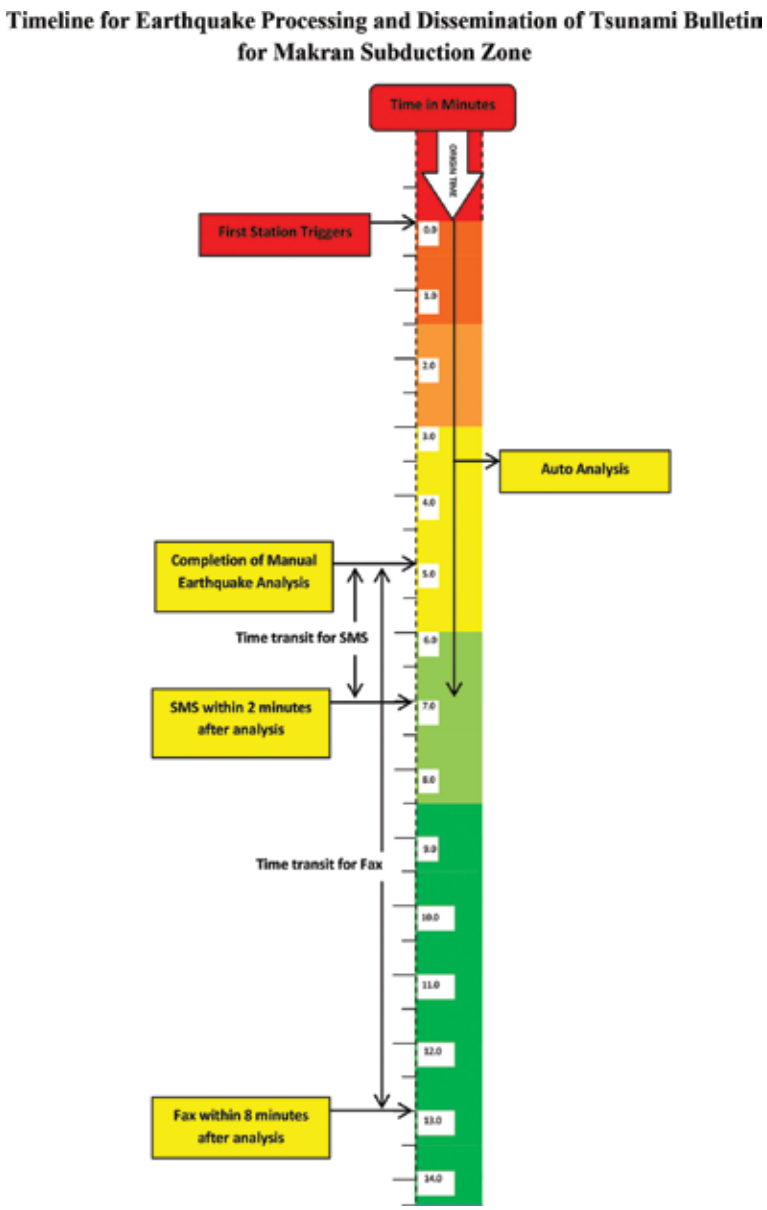

Figure 5. Tsunami warning SoPs, Source; Report developed by NS&TEWC, PMD, 2010.

Through this arrangement, the system installed in a community can be directly activated from PMD Karachi office, using a satellite link. Technically, the warning information received to PMD (about a possible tsunami) will be sent to INMARSAT ground station through TCP/IP link. The information received to INMARSAT ground station then is sent to INMARSAT satellite pointing to area that activates the mass notification systems at Pasni and Gwadar. The system basic building blocks have been shown in **Figure 6**.

http://dx.doi.org/10.5772/64897

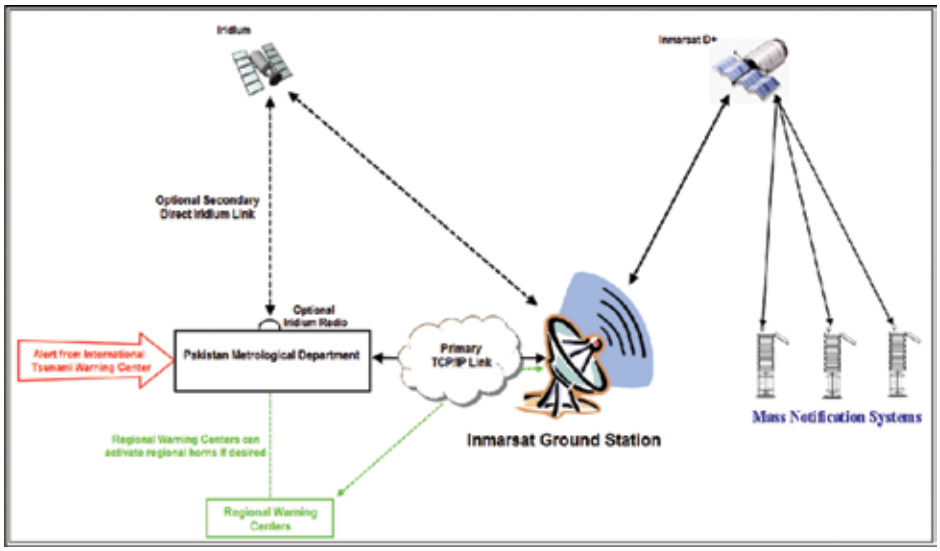

Figure 6. INMARSAT Siren system activated through satellite connection from PMD Tsunami Center Karachi.

3.1.1.3. District disaster management authorities (DDMAs) of the coastal districts

Once DDMAs established (notified) at District Commissioner Office receive an alert from PMD, a warning is issued to the vulnerable communities on the basis of vulnerability assessments. Mode of communication includes high-intensity sirens at mosques and special sirens towers (very limited in numbers). If a power failure occurs, the siren is sounded by police, ambulances, and fire brigade vehicles. The DDMAs maintain communication with these agencies via wireless channels, telephone, fax, GSM in the districts depending upon the availability of the mode of communication. All DCO offices in Sindh also have the facility of video conference, but it again is dependent on the quality of the internet connection. In case of declared emergency the concerned DDMA/DCO office establishes "Emergency Room" on 24-h operational basis to receive and pass on the required information locally and among provincial- and federal-level stakeholders. Local electronic media can also be approached by these authorities for releasing public messages.

However, DDMAs lack appropriate means of reaching to the last mile in case of difficult access coastal area for example boats, helicopters, etc., considering less than half an hour time available before tsunami can attack after a local earthquake hits the area.

3.1.1.4. National and provincial disaster management authorities (NDMA, PDMAs)

NDMA and PDMAs also have SOPs to further disseminate information to a limited number of recipients including media. The NDMA and PDMAs are responsible for communicating the alerts to national and provincial response organizations via press release, emails, phone, faxes, and GSM networks (available list of contacts) and through involving electronic media.

However, it must be noted that because media is more interested in "big news" than in disseminating an early warning, which results in panic. The media, therefore, lacks understanding and training on handling such information in a more appropriate manner.

3.2. Emergency responders

3.2.1. District government

The district government acts as an emergency responder despite having limited resources to mobilize like vehicles, phones, and faxes that are used to relay information. For remote areas that lack phone and fax services, representatives are sent via vehicles and boats to convey the early warning. District government declares the situation as an "emergency" for provincial and federal help if the response is beyond the available resources in the districts. However, assessment of the situation and declaration of emergency takes time; at least 24 h. This can be acceptable in case of a cyclone warning (if received 2 or 3 days earlier); however, for local tsunami, the lead time can be less than 30 min for some coastal areas, which is not manageable by any of the six coastal district administrations.

3.2.2. Police and security agencies (army, navy, coast guards, marine security agency)

Although equipped for immediate relief and emergency response, the armed forces and security agencies do not have an SOP for the dissemination of early warning. However, they do have the means (satellite phones, HF/VHF, etc.) to ensure effective communication to those most at risk. There are some areas in the creek where the access is limited with boats and no direct HF/VHF system setup is available in such settlement. Again the cyclone warning and required evacuation can be managed; however, for local tsunami, it seems difficult to inform the people timely and manage evacuation unless there is a direct mass notification system installed at each such vulnerable community.

There is need to map presence of all these agencies near remote agencies and to develop SOPs that define roles and responsibilities among agencies based on their existing resources.

3.2.3. Nongovernment organizations

NGOs with local presence such as Plan International Pakistan, HANDS Pakistan, International Red Cross (IRC), and many others, collaborate with international NGO coordination groups such as United Nations Office for the Coordination of Humanitarian Affair and government during disasters until the first phase of recovery. Previous disaster risk management (DRM) and contingency plans (developed for few districts) from 2008 to 2013 show allocation of functions for different line-departments and areas of coordination with NGOs and INGOs [6].

Local NGOs have developed a great network and deep roots in coastal areas of Sindh and Balochistan. These NGOs have all the required local knowledge and access to remote areas; however, such organizations are based on donors funding that usually comes in post disaster situation. Potential of these local organizations can be utilized through mapping and devising SoPs for early warning dissemination to the coastal communities at risk.

http://dx.doi.org/10.5772/64897

3.3. Pilot coastal communities (field survey)

Tsunamis of nearby origin, which account for most tsunami fatalities worldwide pose the greatest tsunami hazard on Arabian Sea shores. The nearby source is the Makran subduction zone (MSZ), an active boundary between converging tectonic plates that descends northward beneath Iran and Pakistan. Earth scientists have recently proposed that the zone can produce an earthquake of magnitude 9. This worst case scales up the 1945 Makran earthquake, which was followed by a tsunami that took hundreds of lives [7]. Coastal Pakistan is also subject to tropical cyclones, as seen recently with cyclones Gonu and Phet.

Today coastal communities of Pakistan are much more vulnerable (to tsunami, cyclone and sea level rise) than they were in 1945 because of high population density, rapid urbanization, lack of land use planning and loss of natural safeguards such as mangroves and sand dunes. In urban areas where the multilayer communication networks exist, it is assumed that emergency information can be delivered quickly, though how to manage evacuation from low-lying parts of Karachi has yet to be determined. Pakistan's coastal villages are vulnerable to marine hazards not just because of meager communications, but also because of poverty and

Figure 7. Boundaries of District Thatta, red outlined.

low literacy rates resulting communities' inappropriate level of understanding and responding warnings.

Ten such villages were selected for study of the capacity to receive tsunami warnings. Eight are located in Sindh Province—in Thatta, Sujawal, and Badin districts, mostly located in the Indus Delta—and the other two are in Gwadar District of Balochistan Province. All 10 were visited for field observation of the current situation with regard to the delivery of official tsunami warnings.

3.3.1. District Thatta

Thatta is an ancient city of the Indus delta situated about 100 km from Karachi connected via the national highway. The district Thatta is bounded on the north by district Jamshoro, on the east Tando Muhammad Khan and Badin districts, on the south (Rann of Kutch) and Arabian Sea and on the west by Karachi district. The total area of the district is 17,355 sq. km, whereas the population of the district is around 1.20 million (**Figure 7**).

Communities from the following villages were visited as part of the field survey.

a. Somar Dablo village (Phirt Creek)

b. Siddique Dablo village (Tippun Creek)

c. Dilli Sholani village (Khobar Creek)

d. Tayyab Jutt village (Bhori Creek)

Figure 8. Research team approaching Bhori Creek, two small adjacent islands can be accessed by boats only.

http://dx.doi.org/10.5772/64897

Almost all surveyed villages have no electricity from national grid and rely on solar panels provided by local NGOs to recharge their cell phones and watch TV occasionally. No land lines phones are available and GSM networks are weak, partial, and occasionally available at certain locations in the surrounding. None of the villages are connected by roads and the only access is through boats that are also used to bring drinking water in canes/tanks and daily groceries for the households from nearby city, that is, Keti Bandar (**Figure 8**).

These villages lack basic facilities in education and health; the nearest health facilities available are miles away; at Sakra, Gharo, and Keti Bandar cities. The literacy rate is near zero.

Fishing is the main occupation in this area and women make handicrafts for additional income. Residents of this area lack a local source of clean drinking water and have few sanitation facilities. Freshwater in tankers is purchased at a rate varying from PKR 1000/- to 5000/- (US $ 10–50) per tanker in different villages except Tayyab Jutt village (Bhori Creek) where wells are dug up for water.

Figure 9. Broken solar panels require maintenance and repairs; the only source of power to recharge torch and mobile phone batteries.

As a result of inadequate sanitation and health facilities, most residents are exposed to diarrhea, fever, and flu. The daily sustenance of residents is on fish and vegetables that are purchased from Keti Bandar town due to unavailability of local grocery shops in the village.

For communication, most households rely on radio signals and cellular phones. However, these villagers are not very fond of listening to the news broadcast by radio. They prefer watching television using solar panels/generator and even this mode is not used for watching televised news on popular channels. Televisions in these households are used as a mode of entertainment to watch movies using solar batteries and generators as power source (**Figure 9**).

DRR training for emergencies has been provided by WWF-Pakistan to communities of Dilli Sholani village (Khobar Creek). Villagers were glad to receive the training and appreciated the initiatives taken by the local NGOs but mentioned the inconsistency and follow-up of such activities.

Further information of the surveyed villages is given in **Tables 1** and **2**.

		District Thatta, Keti Bunder				District Sajawal		District Badin		District Gwadar, Ormara,	
Factor/Parameter	Communities	Phirt Creek	Tippun Creek	Khobar Creek	Bhori Creek	Rohro Creek	Haji Yousuf Goth	Peer Sheikh Prio	Goth Ramzan Sheikh	Sonth Village	Sirki Village
Location	Distance from Tehsil Headquarters (km)	5	5	10	7.5	25	25	25	50	>100	>100
	Distance from District Headquarters (km)	50	60	100	76	70	61	25	50	300	300
	Distance from Coastal Highway (km)	*N/A	*N/A	*N/A	*N/A	*N/A	*N/A	*N/A	*N/A	35	30
	Distance from Coastline (m)	40	20	23	63	22	25	15	500	20	300
Elevation (m) with respect to Sea leave		1.8	3.0	8.8	3.0	1.8	6	2.7	8	10	2.4
No. of near available Coast Guard Posts (CGP)		1 (Keti Bunder)	1 (Keti Bunder)	1 (Keti Bunder)	1(Kharo Chan)	1 (Kharo Chan)	1 (Kharo Chan)	1 (Darya Khan Bridge)	1 (Darya Khan Bridge)	1 (Coastal Highway)	1 (Coastal Highway)
Direction of Location of Coast Guard Post from Community		E	E	NE	E	W	SW	N/A	N/A	N	N
Community Distance from Coast Guard Post (km)		5	5	7.5	10	13.5	9.25	N/A	N/A	40	40
Line of Sight from Coast Guard Post		No	No	No	No	No	No	No	No	Unclear (sandy)	Unclear (sandy)
Terrain Issue from Coast Guard Post		Creek	Creek	Creek	Creek	Located far	Located far	Located far	Creek	Sandy	Sandy
In Case of Tsunami possible Evacuation Route	Exists	Only via boat	Only via boat	Only via boat	Only via boat	Road and Via boat	Road and Via boat	Road	Road and Via boat	Road and Via boat	Road and Via boat
	Towards	**CGP	CGP	CGP	CGP	inland	inland	inland	inland	Inland	inland

The pilot communities' structure-related information/data nontrivial to surroundings can be summarized in Table 1.

* Coastal Highway in Sindh Region is not yet completed

** Coast Guard Pakistan Post

Table 1. Communities' structure-related data nontrivial to surroundings.

http://dx.doi.org/10.5772/64897

			District Thatta, Keti Bunder				District Sujawal		District Badin		District Gwadar, Ormara	
Factor/Parameter	Communities		Phirt Creek	Tippun Creek	Khobar Creek	Bhori Creek	Rohro Creek	Haji Yousuf Goth	Peer Sheikh Prio	Goth Ramzan Sheikh	Sonth Village	Sirki Village
Location	Latitude (E)		67°24′29.1″	67°23′85.2″	67°26′19.7″	67°28′71.6″	67°41′80.4″	67°39′13.2″	42°87′06.5″	N/A	25°18′57.899″	25°23′08.999″
	Longitude (N)		24°08′75.2″	24°07′25.0″	24°02′85.6″	24°03′55.8″	24°03′69.2″	24°07′44.4″	26°91′34.7″	N/A	64°13′46.5″	64°06′12.851″
Projected Population			250	300-325	400	2100-2800	50	600	400	8000	600-700	600
Major Population Concentration			Clusters	Clusters	Clusters	Clusters	Clusters	Clusters	Clusters	Clusters	Clusters	Clusters
No. of Households			35	40	50	300-400	350	180	60	800	60-70	60-70
Literacy Rate %			0	0	0 (2 persons are literate)	0	N/A	1% (5 persons are literate)	N/A	N/A	1% (3 persons)	3% (20 persons)
Max. Occupying Area (sq.km)			0.5	1	0.25	0.3	3	2	0.3	3	0.08	002
Community Settlement Pattern			Circular	Irregular	Irregular	Irregular	Irregular	Irregular	Irregular	Irregular	V-Shaped	Irregular
Available Telecom Networks	Wired	Landline Telephone	No	No	No	No	No	No	No	No	*V-Phone	No
		Internet	No	No	No	No	No	No	No	No	No	No
	Wireless	GSM	Zong, Warid, Ufone (*)	Jazz, Telenor Zong, Warid, Ufone (*)	Zong, Warid, Ufone, Jazz (*)	Zong, Warid, Ufone, Jazz (*)	Warid, Jazz	Jazz, Warid	Zong, Ufone, Telenor (*)	Zong, Ufone, Jazz, Telenor (*)	Zong (*)	Zong (*)
		Coast Guard HF, VHF	Yes	Yes	Yes	Yes	Yes	Yes	No	No	No	No
		Wireless Internet	Yes	Yes	Yes	Yes	Yes	Yes	No	(*)3G Phone	(*)3G Phone	No
		Satellite Phones	Not Available	Not Available	Not Available	Not Available	Not Available	Not Available	Not Available	Not Available	Not Available	Not Available
		Others	No	No	No	No	No	No	No	No	No	No
Electricity			No national grid but	Only solar Panels	No, only torches	No, only torches	Only solar panels	Only solar panels	Only solar panels	Only solar panels	Only solar panels	Only solar panels
			solar panels									
Radio Network			No	Yes	Yes	Yes	Yes (occasional)	Yes	Yes	Yes	Yes	Yes
Line of Sight throughout the Village			Clear up to mangroves	Clear	Clear up to mangroves	Clear	Almost clear with vegetation and streams	Almost clear with vegetation and streams	Clear above vegetation	Clear above vegetation	Clear	Sandy
Terrain			All flat, divided by water	All flat	All flat	All flat, divided by water	All flat	All flat	Almost flat	Almost flat	Almost flat	Sandy
Background Noise Level			Natural	Natural	Natural	Natural	Natural	Natural	Natural	Natural	Natural	Natural

The pilot communities' individual information be summarized in Table 2.

* partially and occasionally available

Table 2. Communities' structure-related data trivial to surroundings.

3.3.2. District Sujawal

Previously, Sujawal was an old Taluka (Tehsil) of Thatta district, Sindh, Pakistan. In 2013, the Government of Sindh granted Sujawal, the status of a district. It is located at about 20 km west of Thatta on the road from Badin to Karachi. Sujawal is an agricultural area with a few industries. Its residents are diverse in ethnicity and religion.

The following two communities were selected from Sujawal district: (a) Haji Yousuf Goth and (b) Rohro Creek, Misri Jatt Village.

In the surveyed villages, there are no TV sets, radio sets, and 2–3 mobile phone sets per household are available. Early warning signals are usually broadcasted and received on radio sets (two of which were provided by WWF-Pakistan and two by National Rural Support Programme).

Figure 10. Women collecting partly sweat water from the creek for drinking and household purposes at Rohro Creek near Kharochhan city

The primary occupation in the region is fishing. Residents in Yousuf Goth rely on a big pond for drinking water that is filled from the Indus River during the period of June–July and for next 4–5 months whereas in Rohro creek 8 hand pumps have been installed by WWF-Pakistan in 2014 making access to clean water easy for the villagers (**Figure 10**).

Rohro creek has a relatively high literacy rate of 30% of the population, while in Yousuf Goth five persons can read and write among 180 households. Training by WWF-Pakistan led a few families in Rohro Creek to reduce their risk of flooding by elevating their homes.

Detailed information of the surveyed villages is tabulated in **Tables 1** and **2**.

3.3.3. District Badin

Badin district is a part of Lower Indus plain formed by the alluvial deposits of the Indus River. General elevation of the district is about 50 m above sea level that is lowest for the communities lying along the coastline. The southern part of the district is close to the delta of the river Indus

http://dx.doi.org/10.5772/64897

and the land surface is, therefore, relatively low as compared to the northern half. The eastern part of the district is connected with the sand dunes of Tharparkar district. The degree of slope in Badin is negligible; the district is bounded on the north by Hyderabad district, on the east by Mirpur Khas and Tharparkar districts, on the south by Rann of Kutch, which also forms the international boundary with India, and on the west, it is bounded by Thatta and Hyderabad districts (**Figure 11**).

Figure 11. Boundaries of Coastal District Badin outlined in red.

The following two communities were selected from district Badin: (a) Peer Sheikh Krio and (b) Goth Ramzan Sheikh.

Peer Sheikh Krio Bario village is located about 0.5 km from the coast. It is 2 hours travel away main city and the road leading to the city is only half way paved. The village is deprived of any health facility. Twenty of 400 residents are literate and one graduated from University of

Jamshoro. Fishing remains a predominant profession in the village. A large pond that fills up during rainy season is used for drinking water (**Figure 12**).

Figure 12. Access road to Pir Sheikh Kario Bandari Goth, UC Bhugra Memon, Badin.

For early warning signaling, the coast guard post is located on the Darya Khan Bridge couple of miles away. Television sets are available in two of the households and are used to watch Sindhi news on local channels like KTN. Electricity is not available through national grid and solar panels provided by various NGOs are used to recharge cellular phone and torch batteries.

Basic facilities in the Goth Ramzan Sheikh and in nearby area are lacking including education, access to clean drinking water, and communication. There is a government school building in the village that caters to 150 students with a staff of 4. Since the school is relatively new, only school-going children in the area are being educated. The residents get water from canals in the area, which is also used for drinking purposes.

There is not an early warning system in the area. However, there is potential for one. The residents use a TV on a generator and have adequate access to cellular services. Additionally, they use mobile phone to remain updated with current affairs.

3.3.4. District Gwadar

The district Gwadar, with its 600 km long coast line and un-irrigated tracts of Kulanch and Dasht valleys, is located immediately adjacent to the shipping lanes to and from the Persian

http://dx.doi.org/10.5772/64897

Gulf. The 15,216 sq.kms district area is surrounded by Kech and Awaran districts on north and northeast, Awaran and Lasbela districts on east, the Arabian Sea on south and on the west by Iranian territory Sistan.

Figure 13. Access to Sonth Village near Basool River, Tehsil Ormara, District Gwadar.

The following two communities were selected from Tehsil Ormara in district Gwadar: (a) Sirki village and (b) Sonth village. Both villages are far from the coastal highway and can be accessed by four-wheel drive in two hours. Both villages, because they adjoin the shore, can also be reached by seagoing boats. Electricity is not available through national grid, nor are there telephone connections by wire. The GSM network is also very limited and partially available at certain locations (**Figure 13**).

The area has rudimentary communication services. The residents sometimes get access to Zong as a cellular service and also use radio to listen to news. There are no other means of communication available to facilitate an early warning system. Fishing remains a primary source of income in this village. People rely on a water well that is located far from the village for clean drinking water.

Sonth villages have an abundant supply of water from the river. They also often dig wells in the ground, up to 4–6 feet to access freshwater, whereas in Sirki village, for drinking water, villagers usually purchase a 30 liters tank of water at a price of PKR 50 (US$ 0.5) (**Figure 14**).

Figure 14. View of Sirki Village UC Basool, Tehsil Ormar, District Gwadar.

There is no electricity available in the village, but most households depend on solar panels for lighting and for charging mobile phones' batteries. Zong is the only mobile network whose signals are occasionally available in the region. There are radio sets present in almost every household and people listen to news broadcasted on BBC Urdu and FM Gwadar.

4. Data analysis

With reference to the Section "Pilot Coastal Communities" following information was collected relevant to data on nontrivial, that is, significant and dependent of surroundings of communities studied and data on trivial, that is, insignificant and independent to surroundings. The information is presented in **Tables 1** and **2**.

5. Considerations for effective warning system

The ultimate goal of an effective, warning system is to have the most effective coverage for the most affordable price or cost. Therefore, it is very critical to properly evaluate the structure and local needs of an area before designing and implementing an effective warning system.

http://dx.doi.org/10.5772/64897

The communities' structural information/data can be scrutinized under following parameters to formulate the basic blocks of possible coastal hazards warning notification system.

5.1. Location and coverage

The information about the location of a community and audiences is very crucial in identifying the type(s) of method and hence the system(s) to be used—for both dissemination and notification of a warning to an area.

The information about population concentration directly links with the location of audience; indoor or outdoor. The type of construction gives an idea about effective penetration of an alert to a particular area. A careful analysis of both parameters can give a better selection of an information dissemination system in terms of effectiveness of an alert.

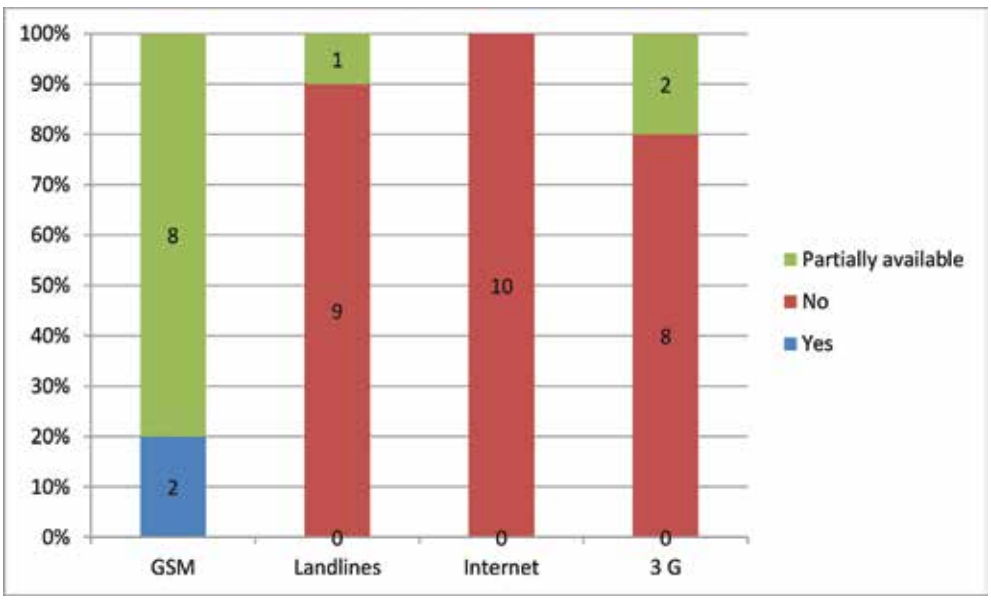

Figure 15. Telecommunication networks availability.

The graph provides an analysis of availability of types of phone coverage in the area. It can be noted that although coverage is partial mostly (80%), but GSM phones were available in all 10 villages as compared to 10 and 20% and respective availability of landline (V phone Pakistan Telecom Wireless phone) and 3 G services in the surveyed villages (**Figure 15**: Telecommunication Networks Availability). But these mobile networks are partially accessible in most of the villages like weak or no signals in the middle of the island and inhabited area. Villagers have to reach out at certain locations for a certain commercial GSM network. Satellite phones

can be used in all 10 surveyed villages; however, none of the community member is presently using this communication mode because of its very high cost.

5.2. Loudness

The information about total occupying area is also related to determine the loudness of an alert, and hence, the number of effective mass notification units required to a particular area. The loudness of sound from all types of siren is subject to diminishing ten decibels at every doubling of distance between the siren and point of measurement.

Since the occupying area information shows that area of each pilot community lies within 0.1–3 sq.km range, single mass notification unit (for each community) with sound intensity of 120–130 dbs can give enough loud sound to cover the whole area for example similar to INMARSAT System currently installed in Gwadar and Pasni cities.

5.3. Area terrain in context with good line of sight

In case of natural hazards like tsunami, loss of lives can be reduced by using an effective timely manner information dissemination and notification method, with least human involvement. This objective can only be achieved if the maximum of hardware used in information dissemination and notification purposes are activated and operated remotely. Generally, radio wireless links located within good line of sight to such systems are used for such purposes. HF/VHF networks presently in use of security agencies are available near most of the villages, that is, six out of ten communities. Few systems where such radio links are not available for information dissemination purposes are activated through satellite links.

5.4. Power source

Almost all mass notification systems rely on electricity; however, mostly, they do not depend on the main power system. Generally, solar panels are used, which have high prices and significantly raise the overall cost of warning notifications system.

As information about pilot communities shows that all villages lack this facility; hence, solar panels (unavailable in Khobar and Bhori Creek only) can be used to these communities as power source.

Regular electricity network is unavailable in ether of the 10 villages, but they use solar energy (very small panels) and battery operated torches.

5.5. Information dissemination from PCG network

Cyclone and tsunami warnings issued by PMD are conveyed to PCG headquarters located at Karachi, which further goes downstream through PCG's internal networks (**Figure 16**).

http://dx.doi.org/10.5772/64897

Figure 16. Information flow of coastal hazards early warning from PMD to PCG posts and community.

The cost and reliability of information dissemination from coast guard posts to community is generally affected by following three factors:

1. Distance between post and community
2. Reliability of ways/means of information dissemination
3. Terrain Issues

5.5.1. Personal notification system using PCG posts' human and technical resources

Personal notification uses emergency personnel or trained volunteers to go door-to-door or to groups of people to deliver a personal warning message. As per the field survey:

1. 7 out of 10 communities lie at least 5 km away from nearest PCG post,
2. no other information dissemination means exists in these communities, and
3. evacuation routes are away from communities.

The best use of this system in present situation is its use as enhancement purposes—in combination with any other individual addressable notification system. The merits and demerits of this system are detailed below:

Advantages	Disadvantages
High degree of credibility.	Very time-consuming and slow.
Provides all necessary information and instructions.	Requires recruiting and training large numbers of personnel.
Very strategic notification.	May require a large amount of logistics support (cars, boats, accurate maps and route information, etc.).
Can reach at a specific location.	Unable to reach a very wide area quickly.
Cost-effective if using trained volunteers.	Expensive if using paid personnel.

5.5.2. Communities where information dissemination is not possible through PCG posts

The communities' data analysis shows that Sirki Village and Sonth Village lie at a faraway distance from the nearest post, with severe terrain and line of sight issues. Hence, information cannot be directly disseminated to these villages through PCGs posts without addition of few repeater stations. Since repeater stations have a considerable cost, it is not feasible to use this method as a solution. In context with present situation, there exist two possible systems in this regard.

5.5.2.1. Mass notification systems linked with satellite activation

Because of its good coverage to the area, mass notification system linked with satellite activation such as NMARSAT system at Gwadar and Pasni instantaneously passes information. The system has (a) high degree of credibility, (b) very effective in terms of time line of an emergency, (c) have average component cost compared to other wireless mass notification systems, (d) running operational coast to satellite link.

5.5.2.2. Addressable notification systems—satellite phones

This type of solution includes satellite phones such as Thuraya. The main disadvantages of such system in present scenario are as follows: (a) continuous operational coast, (b) ownership issues, and (c) satellite phones are generally intended for outdoor usage.

Each of above-mentioned systems has advantages and limitations in its applications to a particular community. If a system has better response and is more reliable at one side (like Wireless operated Mass Notification Systems), then its high cost limits its application.

http://dx.doi.org/10.5772/64897

6. Conclusion

Tsunami generated from a near source has proven its fatality equally for developing and developed nations through 2004 Indian Ocean and March 2011 events in Indonesia and Japan, respectively. The real challenge of relaying the early warning to the vulnerable communities has been the most crucial element, being race against time, allowing mostly less than half an hour reaction period. Every single minute has its significance to be utilized optimistically and well planned.

In case of tsunami generated from Makran Subduction Zone, the PMD, one and the only organization in Pakistan, authorized to issue warnings, uses reliable data obtained from national and global seismographic network to monitor seismic activity that might become the cause of a tsunami. For relaying the warnings, multiple channels of communication are used by PMD including automated GPRS based SMS, mobile phone based SMS, automated fax, manual fax, satellite telephone communication, website updating or email. However, the ground situation at receiving end is quite unable to access such vital information timely through any of the available means of communication which is evident through case studies of 10 coastal communities presented in Sections 3.3 and 4 previously.

The communities studied lies at far distances from respective Tehsil and district headquarters that are the last administrative units of the government to receive any communication with regard to coastal hazard early warnings. **Table 1** shows minimum distance of 5 km to a maximum of 300 km making it extremely difficult for minimum and impossible for average and maximum distant communities to send an "official messenger" for personal notification especially for near filed tsunami threat.

Pakistan Coast Guard posts are established at comparatively closer for example; on average at 16 km apart, in comparison to 35.25 and 822 km average distance of Tehsil and district Headquarters. These posts are also equipped with the fastest means of communication like HF/VHF networks, but presently the communication is restricted to security use only. For bringing this network to disaster, emergency use such as EW, some principal agreements, protocol and SoPs among concerned organizations are to be established.

For other means of communication like phone, TV, and fax and GSM networks, referring to **Table 2**, electricity and landlines are not available in any of the villages studied. However, limited and partial GSM (Global System of Mobile communication) networks are available at some particular locations, which are not yet strong enough to be a reliable mean of EW dissemination. Radio broadcast is mostly available; however, there are two issues yet to be tackled, usually batteries are used as energy source, which are hardly locally available, second is the line of communication between PMD and radio channels is to be streamlined and established.

Population of the communities studied varies from 50 individuals to 8000 concentrated into on average, less than 2 km of area. Four out of ten settlements (located in the creeks) are only accessible through boats; three have population of less than 1000 individuals, whereas only one has maximum population of 2800. In recent past, the only mode of communication used

to convey cyclone early warning to those communities was personal notification, that is, sending local emergency responders; mostly Armed Forces and Security Agency officials on boats and vehicles to inform and support for evacuation to the vulnerable communities. It took hours and in some cases days in comparison to extremely quick actions and reactions required for a local tsunami that might happen like 1945 event.

Therefore, PMD's SoPs alone are not enough to get prepare for a potential threat of local tsunami impacts in Pakistan. The urgent need of developing a well-coordinated time-based SoPs for all stakeholders involved in tsunami warning and evacuation chain is extremely important along with enhancing capacities for technological solutions to quickly rely information to the last mile. This would not be the last but the first step toward mitigation and preparedness as there are still many administrative issues to deal with and to tackle the situation, for example, effective land use managements, expanding data base and information related to the prevailing hazards and vulnerabilities regarding communities and areas under threat of future tsunami. Optimum utilization of available high tech communication networks with armed forces and security agencies, that is, to bring those in the chain of early warning dissemination can reduce burden on limited resources of the nation. Above all, the need of preparing communities to observe natural warning and train them for self-evacuation and emergency response is the most urgent and important line of action at the moment.

7. Recommendations

The following recommendations can help strengthen the early warning dissemination system for coastal hazards in Pakistan.

7.1. Technological solutions

- Considering quick response, better reliability and long life the most preferred system in Phirt Creek, Tippun Creek, Khobar Creek, Bhori Creek, Misri Jatt Village, Haji Yousuf Goth, and Goth Ramzan Sheikh is a wireless operated mass notification system.
- In case of budgetary constraints, the second preferred solutions to these communities is the use of Radio as warning dissemination and notification system in combination with Personal notification system parallel to this system through capacity building measures taken in target communities.
- For villages in Sirki and Sonth, the best preferred solution is satellite-activated mass notification system. As a second option satellite phones are recommended as mass notification system.

7.2. Land use management

It has been observed that communities tend to settle on remote islands along the coastal belt and due to lack of development in these areas, limited sources of communication exist, which makes communities more vulnerable to coastal hazards. It is recommended that authorities

http://dx.doi.org/10.5772/64897

establish a land use management system that facilitates knowledge on land use along the coastal belt and prevents settlements in remote locations that cannot be easily accessed, especially in times of distress.

It is also important to note that development usually takes place around a central point and infrastructure is installed along that progression. Hence, public and private authorities cannot invest in infrastructure everywhere. This impedes the remotes settlements' access to utilities. However, the government can't be blamed because they facilitate development along a central point and should not be held responsible for providing infrastructure to the most isolated communities.

7.3. Self-response training of communities

Although the communities are aware of coastal hazards, they do not know how to address such a situation if it arises. It is pertinent that the communities are trained on the following:

1. Detection of early warning via natural signs such as abnormal behavior of animals;
2. Basic emergency response, especially how and where to evacuate;
3. Interpretation of bulletins issued by PMD and DDMAs;
4. Different categories of threat and how they should respond to it.

7.4. Communication of early warning in local languages

In addition to the existing format, PMD should ensure that the bulletin formats are available and disseminated in local languages, particularly Sindh and Balochi.

7.5. Training of media

Currently, the media has been observed to sensationalize news instead of reporting it. They should be trained on how to communicate early warning so that panic can be avoided. It would also be in the interest of PMD and NDMA to have designated representatives to coordinate with media in case such a situation arises.

7.6. Research

There is a need for research to investigate the vulnerable areas and analyze the extent of damage based on extrapolation of historically available data. For example, it would be important to highlight the potential increase in Karachi's vulnerability to a tsunami similar to that of 1945, based on the increase in population and infrastructure.

7.7. Delineation of responsibilities

There is need to map the presence of all these agencies and to develop SOPs that define roles and responsibilities among agencies (including security establishments) based on their existing resources for effective dissemination of information.

Acknowledgements

The author would like to thank the Pakistan affiliate of Oxfam GB for funding the research and for assisting officials and residents in identifying vulnerabilities of the coastal communities. The logistics support by the WWF Pakistan field offices was also vital for the execution of the field activities. Guidance and interpretational services were contributed by Ms. Zubaida Birwani from TCCR, Mr. Abdullah Usman from Rural Community Development Council (RCDC) Gwadar, WWF Pakistan staff at Gharo (Mr. Yameen Samo, Mr. Ali Samo and Mr. Ali Hassan) and WWF Karachi Office Mr. Moazzam Khan.

Author details

Ghazala Naeem[1*], Abdullah Usman[2] and Jamila Nawaz[3]

*Address all correspondence to: ghazala_ghq@hotmail.com

1 Resilience Group, Islamabad, Pakistan

2 Rural Community Development Council, Gwadar, Pakistan

3 DRR & Climate Change, Oxfam GB, Pakistan

References

[1] Hoffmann G, Rupprechter M, Balushi N Al, Grützner C, Reicherter K. The impact of the 1945 Makran tsunami along the coastlines of the Arabian Sea (Northern Indian Ocean) – a review: Zeitschrift für Geomorphologie, Supplementary Issues, Volume 57, Number 4, December 2013, pp. 257-277(21).

[2] National Seismic & Tsunami Early Warning Center – Pakistan. Available from: http://www.pmd.gov.pk/seismic/seismicnew/index.html (Accessed 05/02/2016).

[3] Tsunami Warning Standard Operating Procedure, Report developed by National Seismic & Tsunami Early Warning Center – Pakistan, Number 4-54, 2010.

[4] 1945 Makran Tsunami—IOTIC—IOC for Makran 1945. Available from: http://iotic.ioc-unesco.org/1945makrantsunami/ (Accessed 05/02/2016).

[5] Proceedings of UNESCO-IOC Strengthening Tsunami Warning and Emergency Responses: Training workshop on The Development of Standard Operating Procedures, 23-27 November 2009, Karachi, Pakistan.

http://dx.doi.org/10.5772/64897

[6] Islamic Relief-Pakistan Research Study: Research Study on Disaster Vulnerability and Capacity Assessment-Number 27-59, March 2015.

[7] Kakar DM, Naeem G, Usman A, Hasan H, Lohdi HA, Srinivasalu S, Andrade V, Rajendran CP, Nabderi Beni A, Hamzeh MA, Hoffmann G, AL Balushi N, Gale N, Kodijat AM, Fritz HM, Atwater BF. Elders Recall an Earlier Tsunami on Indian Ocean Shores. Eos, Transactions American Geophysical Union, Volume 95, Issue 51, Version of Record online: 23 Dec 2014.

Edited by Mohammad Mokhtari

This book is a collection of contribution from experts involved in tsunami study for the purpose of covering its different aspects from generation to warning system to be applied in tsunami risk reduction. The presented chapters have been peer reviewed and accepted for publication. The content of the book consists of information on tsunami propagation from the open sea to the coast and coastal tsunami warning using deployed HF radar systems in different parts of North America and Japan. In this book, tsunami propagation, preliminary methods for evaluating the suitability of radar sites for tsunami detection using simulated tsunami velocities and factors affecting tsunami detectability are discussed and methods for reducing the false alarms are described. It further covers multi-scale meteorological systems resulted in meteo-tsunami and tsunami generation due to a landslide or a submarine volcanic eruption, where few case studies have been presented. The occurrence and characteristics of tsunami in Sweden, using paleo-tsunami events from different parts of the Scandinavia and finally challenges and opportunities for reducing losses to fast-arriving tsunamis in remote villages along Pakistan coast, with few examples are also discussed.

ISBN 978-953-51-5455-6

IntechOpen